

# Motion Generation and Control: Selected Topics With Applications

## 7.1 OVERVIEW

Humanoid robots are expected to perform a broad variety of tasks, similar to humans. Basically, two large groups of periodic and aperiodic motion tasks can be distinguished. The most prominent example of a periodic motion task is walking on a regular (flat) ground. This is an indispensable task for a humanoid robot. Other examples of periodic motion tasks are ascending/descending a staircase and running. Historically, the initial focus in the humanoid robotics research field was on gait generation and walking control [114]. This was a very challenging task for more than 25 years, until the announcement of the P2 humanoid prototype by Honda Motor Co. in 1996 [39]. The recent state of the art in periodic gait generation and control is based on the capture point (CP) concept (see Section 5.5). An implementation that stabilizes the unstable component of motion during walking has been described in [105]. In this chapter, the implementation described in [22] is explained and applied to gait generation and walking control on sand [60].

The class of “aperiodic” [9] or “nongaited” [35] motion tasks includes such tasks as fetching/manipulating objects within cluttered environments, performing a job with a hand-held tool, sitting/lying down and standing up, negotiating highly irregular terrain (e.g. a free-climbing robot [12]), crawling through narrow spaces, and climbing a ladder. These types of tasks require a somewhat different approach than those used in periodic motion generation tasks. In the pioneering work [70], motion generation for aperiodic tasks was based on the given initial and target postures. The process is accomplished in two phases. First, a statically stable collision-free path is computed via a modified version of the Rapidly exploring Random Trees (RRTs) algorithm [72]. Second, the computed path is smoothed and transformed into a dynamically stable whole-body trajectory with the help of the AutoBalancer [55]. This approach can be characterized as time consuming and prone to robustness issues, though. Heuristics have to be employed during the search, and hence there is no guarantee that an existing solution will be found.

The roots of motion generation for humanoid robots are found in the closely related field of physics-based human character animation methods. These methods became widely adopted recently. Already at an early stage, though, it was clarified [119] that to obtain a “realistic” and smooth motion of the animated character for reaching a prespecified goal, two problems have to be addressed. First, the initial state has to be determined carefully to ensure the

appropriateness of the generated motion trajectory. Second, since the character is underactuated, its successful propulsion requires a force (reaction wrench) input trajectory. The force trajectory cannot be generated in an independent fashion from the motion trajectory; they are intertwined since the impressed/reaction wrenches depend upon the acceleration of the CoM and the angular accelerations of the body segments (cf. Section 5.8.1). As a consequence, it became apparent that simulation methods based on initial-value problems are not appropriate; the above objectives require the solution of a constrained two-point boundary problem. Furthermore, it has been also argued that the movement “realism” can be further improved by introducing joint torque minimization into the algorithm. This implies that, in addition to the motion/force task constraints, physical constraints also need to be specified. The former determine the task completely; they freely propagate forward/backward in time. The latter are used to limit the “muscle” forces (i.e. the actuated joint torque) and to determine an appropriate contact (i.e. passive-joint) behavior. An optimal, physically feasible solution trajectory can then be found with the help of an appropriate constraint optimization method, e.g. one of those described in Chapter 5. It is important to note that the character of the solution is global, but time consuming and, hence, only suitable for off-line calculations. To summarize, for motion generation and control of complex tasks as those mentioned above, the robot should be equipped with the following two general capabilities: (1) multicontact planning [12,24] and (2) whole-body motion generation consistent with the constraints [70,35,33].

There are a few ways of improving the efficacy of the process of motion generation for aperiodic motion tasks. First, discrete sets of contact states can be added to the motion plan [12]. The contact states are determined from a coarse model/map of the environment constructed in advance. The process is referred to as contact planning [24]. For each given contact state, a set of statically stable postures is obtained.<sup>1</sup> This process is referred to as the posture generation [15]. Posture generation is accomplished with the help of a constraint-based inverse kinematics and statics solver [10,11]. Recall that, as discussed in Chapter 3, for a given set of contacts there is in general an infinite number of statically stable postures [12–14]. There are also an infinite number of motion/force trajectories that connect the generated keyframes in accordance with the kinematic/dynamic relationships and the various constraints. A dynamically feasible trajectory can be generated via interpolation [70,33]. This approach is referred to as the “contact-before-motion” approach [35]. It is important to note that because of the variety of tasks and environments envisioned, the contact planning process is nontrivial. For example, it is not sufficient to plan one contact state at a time since the current contact state determines all future states [12]. A number of methods have been developed so far for contact planning purposes. Interested readers are referred to [35,12,23,11,24,15,109]. It should be noted that, although the contact state-based posture/trajectory generation approach is faster than the algorithms based on RRTs, it is still quite time demanding due to the involvement of iterative optimization procedures. It is also important to note that the method is not straightforward since there is no guarantee that the preplanned contact states will facilitate the generation of smooth, “naturally looking” constraint-consistent movements. Additional contact states/keyframes may have to be inserted to support the process of motion generation, as already noted.

<sup>1</sup> Such postures are sometimes called “keyframes” [33], a term borrowed from the field of animation.

Another way of increasing the time efficiency in motion generation is by making use of the reduced dynamics representations in terms of end-link and CRB coordinates. Note that the posture-based motion generation process implies that the optimization runs over the joint space, involving all of the DoFs. The number of variables can be drastically decreased by resorting to one of the reduced forms of the equation of motion (cf. Section 4.13). In this case, the preplanned contact states are connected via trajectories determined from the CRB dynamic relations. As a result, one obtains constraint-consistent CRB and end-link motion/force trajectories that can be resolved for the joint torques via the inverse dynamics [69]. Another possibility for improvement is to divide the trajectory generation process into two phases. First, a parametrized path is generated that connects the contact states. Then, a constraint-consistent trajectory is obtained by determining the appropriate timing along the path [33]. This approach also has the advantage of facilitating time-optimal motion generation [97,98].

The time efficiency of motion generation can also be increased by making use of motion synergies or primitives [30,34]. These are motion patterns in joint-space that are controlled with fewer variables than the number of DoFs. An approach to synergy-based motion generation based on an inverse kinematics solution with task prioritization is introduced in Section 7.5. Synergy-based motion generation for reactive balance control with planar models is discussed in Section 7.6. Reactive synergies obtained with a whole-body model are addressed in Section 7.7. The final section in this chapter deals with motion generation for impacts.

## 7.2 ICP-BASED GAIT GENERATION AND WALKING CONTROL

### 7.2.1 CP-Based Walking Control

This section introduces a gait generation and walking control approach based on the CP concept [22]. The following expressions for the extrapolated CoM (xCoM) and the CP dynamics represented in 2D space will be employed (cf. also (5.55) and (5.56)):

$$\mathbf{r}_{ex}(t) = \mathbf{r}_g(t) + \frac{\dot{\mathbf{r}}_g(t)}{\omega}, \quad (7.1)$$

$$\dot{\mathbf{r}}_{ex} = \omega (\mathbf{r}_{ex} - \mathbf{r}_p). \quad (7.2)$$

Here  $\mathbf{r}_{ex}$ ,  $\mathbf{r}_g$ , and  $\mathbf{r}_p$  are 2D vectors denoting the xCoM, the gCoM, and the CoP, respectively (see Section 5.3). Eqs. (7.1) and (7.2) are rewritten in the frequency domain as follows:

$$\mathbf{r}_g(s) = \frac{1}{1 + \frac{1}{\omega}s} \mathbf{r}_{ex}(s), \quad (7.3)$$

$$\mathbf{r}_{ex}(s) = \frac{1}{1 - \frac{1}{\omega}s} \mathbf{r}_p(s). \quad (7.4)$$

Eq. (7.3) represents the first-order open-loop CoM dynamics taking the CP as the input, while (7.4) represents the first-order open-loop CP dynamics taking the CoP as the input.

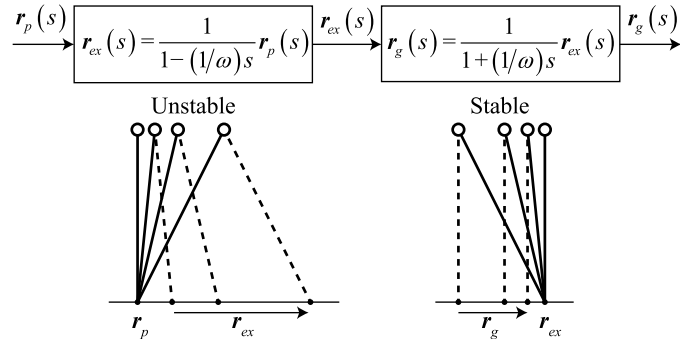


FIGURE 7.1 Coupled dynamics of the CP and the CoM.

The system (7.3) is stable because the real part of the characteristic root,  $s = -\omega$ , is negative. On the contrary, the system (7.4) is unstable because the real part of the characteristic root,  $s = \omega$ , is positive. Fig. 7.1 illustrates the coupled dynamics of the CP and CoM. In order to stabilize the CP dynamics, the following CP controller was proposed in [22] (cf. also (5.57)):

$$\mathbf{r}_p^{ref} = \frac{1}{1 - e^{\omega dT}} \mathbf{r}_{ex}^{des} - \frac{e^{\omega dT}}{1 - e^{\omega dT}} \mathbf{r}_{ex}. \quad (7.5)$$

Substituting  $\mathbf{r}_p^{ref}$  from (7.5) into  $\mathbf{r}_p$  in (7.2), the following system is obtained:

$$\dot{\mathbf{r}}_{ex} = \frac{\omega}{1 - e^{\omega dT}} (\mathbf{r}_{ex} - \mathbf{r}_{ex}^{des}). \quad (7.6)$$

The frequency-domain representation can be written as

$$\mathbf{r}_{ex}(s) = \frac{1}{1 - \frac{1 - e^{\omega dT}}{\omega} s} \mathbf{r}_{ex}^{des}(s). \quad (7.7)$$

Note that  $dT$  is always positive; hence  $e^{\omega dT}$  is greater than 1, and consequently the real part of the characteristic root,  $s = \omega / (1 - e^{\omega dT})$ , is negative. Therefore, the CP controller (7.5) stabilizes the system. The block diagram of the stabilized CP and CoM dynamic system is illustrated in Fig. 7.2.

### 7.2.2 CP-Based Gait Generation

Let  $T_{step}$  be the specified duration of the step. The gait generation sequence is based on relative time, i.e.  $0 \leq t \leq T_{step}$ . The sequence comprises the following phases:

**(a) Planning of foot prints:** The foot prints are designed with the step length  $L_x$ , step width  $L_y$ , and step direction  $L_\theta$  (see Fig. 7.3). The step width  $L_y$  is generally set to the natural

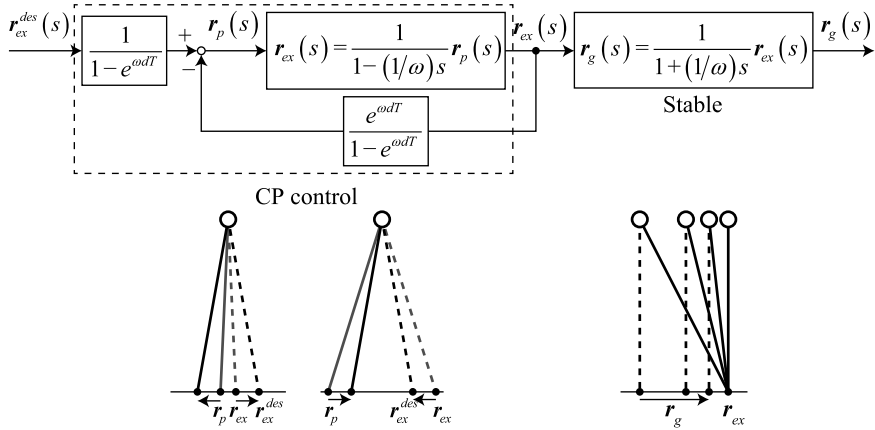


FIGURE 7.2 CP stabilization control.

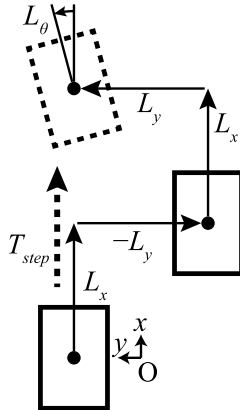


FIGURE 7.3 Step parameters.

length between the left and right legs. The step length  $L_x$  and step direction  $L_\theta$  are heuristically designed depending on the dimensions of the humanoid robot and the desired pathway.

**(b) Planning of the CPs at the end of each step (eos):** The desired CP at the end of the  $i$ th step  $r_{ex,eos}^i$  is located at the ground projections of the corresponding ankle positions (see Fig. 7.4A). The CP at the beginning of the  $i$ th step  $r_{ex0}^i$  is determined based on the initial position and velocity vectors of the gCoM. The reference CoP at the  $i$ th step  $r_{p0}^{ref,i}$  is calculated based on  $r_{ex,eos}^i$  and  $r_{ex0}^i$ . However, there is no guarantee that the calculated reference CoP,  $r_{p0}^{ref,i}$ , will lie within the BoS. When the calculated reference CoP lies outside the BoS, it is modified, as explained in Phase (d). Depending on the parameter setting for the desired walking pattern, it might happen that  $r_{p0}^{ref,i}$  frequently lies outside the BoS. This problem can be alleviated by

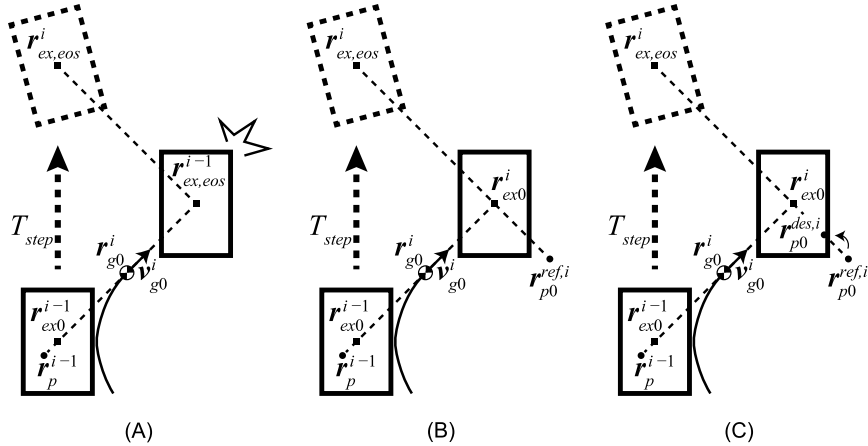


FIGURE 7.4 Design components for walking pattern generation based on the CP: (A) Planning of footprints and CPs at the end of each step (eos). (B) Calculation of the reference CoP  $r_p^{ref}$  using (7.5). (C) When  $r_p^{ref,i}$  is located outside the BoS, it is shifted within the BoS.

modifying  $r_{ex,eos}^i$  with a heuristically designed constant offset that is added to the preplanned ankle position, such that the resulting CoP  $r_{p0}^{ref,i}$  always lies within the BoS for the desired walking pattern. In this way, the frequent modification of the reference CoPs  $r_{p0}^{ref,i}$  can be avoided.

**(c) Calculation of the reference CoP:** Let  $r_{g0}^i$  and  $v_{g0}^i$  be the 2D initial position and velocity vectors of the gCoM, respectively, in the  $i$ th step (see Fig. 7.4A). Note that  $r_{g0}^i$  and  $v_{g0}^i$  are equal to the terminal position and velocity of the gCoM in the  $(i-1)$ th step. Substituting  $r_{g0}^i$  and  $v_{g0}^i$  into (7.1), the initial CP at the  $i$ th step  $r_{ex0}^i$  is calculated as follows:

$$\mathbf{r}_{ex0}^i = \mathbf{r}_{g0}^i + \frac{\mathbf{v}_{g0}^i}{\omega}. \quad (7.8)$$

The reference CoP at the  $i$ th step  $r_{p0}^{ref,i}$  is calculated by substituting  $\mathbf{r}_{ex}^{des} = \mathbf{r}_{ex,eos}^i$ ,  $\mathbf{r}_{ex} = \mathbf{r}_{ex0}^i$ , and  $dT = T_{step}$  into (7.5). Thus

$$\mathbf{r}_{p0}^{ref,i} = \frac{1}{1 - e^{\omega T_{step}}} \mathbf{r}_{ex,eos}^i - \frac{e^{\omega T_{step}}}{1 - e^{\omega T_{step}}} \mathbf{r}_{ex0}^i. \quad (7.9)$$

**(d) Calculation of the desired CoP for step initialization:** When the reference CoP  $r_{p0}^{ref,i}$  (calculated from (7.9)) lies within the BoS, the desired CoP for step initialization is determined as  $\mathbf{r}_{p0}^{des,i} = \mathbf{r}_{p0}^{ref,i}$ . However,  $\mathbf{r}_{p0}^{ref,i}$  may not always lie within the BoS (see Fig. 7.4B). In this case,  $\mathbf{r}_{p0}^{ref,i}$  is shifted to the nearest point on the footprint boundary along the line  $\mathbf{r}_{ex,eos}^i - \mathbf{r}_{ex0}^i$ .

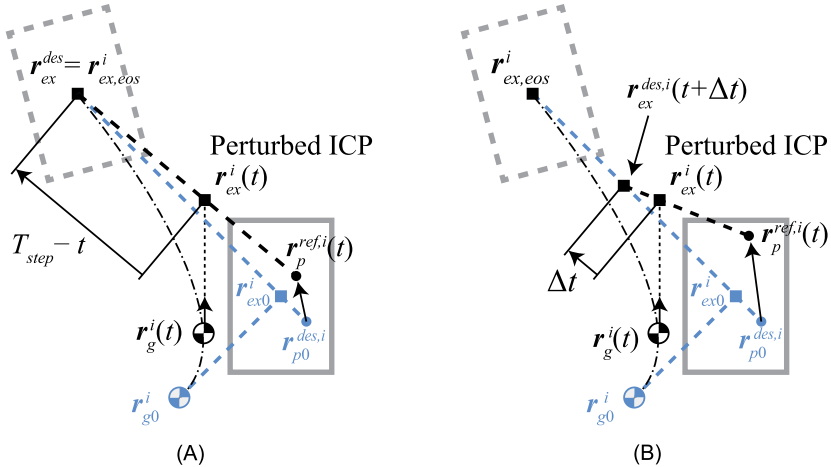


**FIGURE 7.5** Concept of two CP controllers. (A) The CP end-of-step (CPS) controller. (B) The CP Tracking (CPT) controller.

(see Fig. 7.4C). If the line does not intersect the  $i$ th footprint, the line is slightly tilted to do so. The desired CoP  $r_{p0}^{des,i}$  is then determined from the intersection point.

### 7.2.3 ICP Controller

The desired COP  $\mathbf{r}_p^{des,i}$  at the  $i$ th step is obtained from the Phases (a)–(d) presented in Section 7.2.2. The desired CP trajectory is obtained by solving (7.2) with  $\mathbf{r}_{ex} = \mathbf{r}_{ex0}^i$  and  $\mathbf{r}_p = \mathbf{r}_{p0}^{des,i}$  as

$$\mathbf{r}_{ex}^{des, i}(t) = e^{\omega t} \left( \mathbf{r}_{ex0}^i - \mathbf{r}_{p0}^{des, i} \right) + \mathbf{r}_{p0}^{des, i}, \quad (7.10)$$

which is a 2D extension of (5.50);  $\mathbf{r}_{ex}^{des,i}(t)$  ( $0 \leq t \leq T_{step}$ ) is referred to as the *instantaneous* CP (ICP) trajectory [67]. The ICP trajectory heads toward  $\mathbf{r}_{ex,eos}^i$ . However, in reality the ICP trajectory is perturbed by modeling errors and/or disturbances, or for other reasons. In the CP control method proposed in [22], two different approaches were verified: the CP end-of-step (CPS) control and the CP Tracking (CPT) control. The concepts of the CPS and CPT controllers are illustrated in Fig. 7.5.

**CP end-of-step (CPS) controller:** Let  $T_{step}$  be the specified duration of a step. As illustrated in Fig. 7.5A, the ICP trajectory is controlled so that  $\mathbf{r}_{ex}^i(t)$  reaches  $\mathbf{r}_{ex,eos}^i$  at  $t = T_{step}$ . Therefore, (7.5) has to be modified as follows:

$$\mathbf{r}_p^{ref,i}(t) = \frac{1}{1 - e^{\omega(T_{step}-t)}} \mathbf{r}_{ex,eos}^i - \frac{e^{\omega(T_{step}-t)}}{1 - e^{\omega(T_{step}-t)}} \mathbf{r}_{ex}^i(t) \quad (0 < t \leq T_{step}). \quad (7.11)$$

Note that the CPS controller does not depend on future step positions but only on the final CP at the  $i$ th step  $r_{ex, eos}^i$  and the current CP  $r_{ex}(t)$ . Hence reactive gait planning is possible.

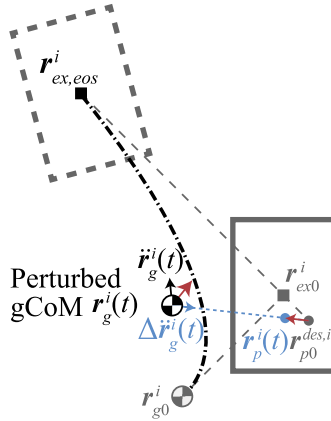


FIGURE 7.6 Concept of CP-based gait generation and ZMP control.

**CP tracking (CPT) controller:** Let  $\Delta t$  be the control period. As illustrated in Fig. 7.5B, the CPT controller controls the current ICP  $r_{ex}^i(t)$  toward the desired ICP at the next sampling period  $r_{ex}^{des,i}(t + \Delta t)$ . Since  $r_{ex}^{des,i}(t + \Delta t)$  is used as the desired ICP, (7.5) is rewritten as

$$\mathbf{r}_p^{ref,i}(t) = \frac{1}{1 - e^{\omega\Delta t}} \mathbf{r}_{ex}^{des,i}(t + \Delta t) - \frac{e^{\omega\Delta t}}{1 - e^{\omega\Delta t}} \mathbf{r}_{ex}^i(t) \quad (0 < t \leq T_{step}). \quad (7.12)$$

In the simulation in [22],  $\Delta t$  was set at 0.05 s, while  $T_{step}$  was set at 0.8 s.

**Modification of the reference CoP:** The reference CoP  $\mathbf{r}_p^{ref,i}(t)$  calculated from (7.11) or (7.12) may not always lie within the BoS. When  $\mathbf{r}_p^{ref,i}(t)$  is outside the BoS, it should be shifted within the BoS (cf. Phase (d) in Section 7.2.2). The desired CoP  $\mathbf{r}_p^{des,i}(t)$  is then set at the modified reference CoP.

#### 7.2.4 CP-Based Gait Generation and ZMP Control

The main disadvantage of the well-known gait generation approach based on preview control [56] is that the preview controller depends on future reference CoPs to generate the motion. Hence, the preview controller can not modify the generated gait to react to an external disturbance. CP-based gait generation overcomes this problem.

Both the CPS and the CPT controller calculate the current ICP  $r_{ex}^i(t)$  at every control cycle. The reference CoP  $\mathbf{r}_p^i(t)$  is given based on the difference between the desired and current ICPs. The CoP is controlled so that the current CP moves toward the desired CP.

In [60], the CP dynamics were used just to generate the reference gCoM trajectory, and a conventional ZMP controller was used for stabilization. The main advantage of this method is that a well-established ZMP controller can be used while reactively generating the gait pattern. The concept of an on-line gait generation and stabilizing control used in [60] is illustrated in Fig. 7.6.

Note that the calculation of the desired CoP in [60] is different from the CPS or CPT controllers. The initial ICP  $\mathbf{r}_{ex0}^i$  and the reference CoP  $\mathbf{r}_{p0}^{ref,i}$  at the  $i$ th step are calculated by (7.8) and (7.9), respectively. The reference CoP is modified so that the CoP lies within BoS, and the desired CoP is determined (if the reference CoP lies within BoS, the desired CoP is set at the reference CoP).

The reference CoP  $\mathbf{r}_p^{ref,i}$  corresponds to  $\bar{\mathbf{u}}$  in Fig. 5.12. As shown in Fig. 5.12, the ZMP manipulator receives the desired CoP  $\mathbf{r}_{p0}^{des,i}$  and produces the desired CoM trajectory  $(\mathbf{r}_g^{des,i}(t), \dot{\mathbf{r}}_g^{des,i}(t))$  (see Fig. 7.4C).

The reference gCoM trajectory is calculated from the explicit solution of the gCoM dynamics (5.11), i.e.

$$\begin{aligned} \begin{bmatrix} \mathbf{r}_g^i(t) \\ \dot{\mathbf{r}}_g^i(t) \end{bmatrix} &= \begin{bmatrix} \cosh(\omega t) & 0 & \frac{1}{\omega} \sinh(\omega t) & 0 \\ 0 & \cosh(\omega t) & 0 & \frac{1}{\omega} \sinh(\omega t) \\ \omega \sinh(\omega t) & 0 & \cosh(\omega t) & 0 \\ 0 & \omega \sinh(\omega t) & 0 & \cosh(\omega t) \end{bmatrix} \begin{bmatrix} \mathbf{r}_{g0}^i \\ \mathbf{v}_{g0}^i \end{bmatrix} \\ &+ \begin{bmatrix} 1 - \cosh(\omega t) & 0 \\ 0 & 1 - \cosh(\omega t) \\ -\omega \sinh(\omega t) & 0 \\ 0 & -\omega \sinh(\omega t) \end{bmatrix} \mathbf{r}_{p0}^{des,i}, \end{aligned} \quad (7.13)$$

where the hyperbolic functions are defined as follows:

$$\cosh(\omega t) = \frac{e^{\omega t} + e^{-\omega t}}{2}, \quad \sinh(\omega t) = \frac{e^{\omega t} - e^{-\omega t}}{2}.$$

The deviation of the gCoM from the desired trajectory can be controlled by any well-established ZMP controller. In [60], the torso position compliance control (TPCC) approach [85] (see also Section 5.4.5) was used in the stabilizing controller.

## 7.3 BIPED WALK ON SAND

### 7.3.1 Landing Position Control for Walking on Sand

The difficulty of walking on loose soil for a humanoid robot is that the soil under the supporting foot easily deforms because of the weight of the robot. Hence, if the CoP goes to the fringe of the BoS, the soil under the CoP will be depressed, and consequently the robot body will tilt. Most of the stabilizing controllers control the net CoP (the ZMP), however the shift of the CoP may cause sinking on loose soil.

In order to compensate the tilt of the robot body caused by sinking and sliding on soil, a landing position control approach was proposed in [60]. According to this approach, when the deviation of the gCoM from the desired position exceeds a previously specified threshold  $\delta r_g^{th}$ , the deviation is compensated by shifting the landing position. The shift of the landing

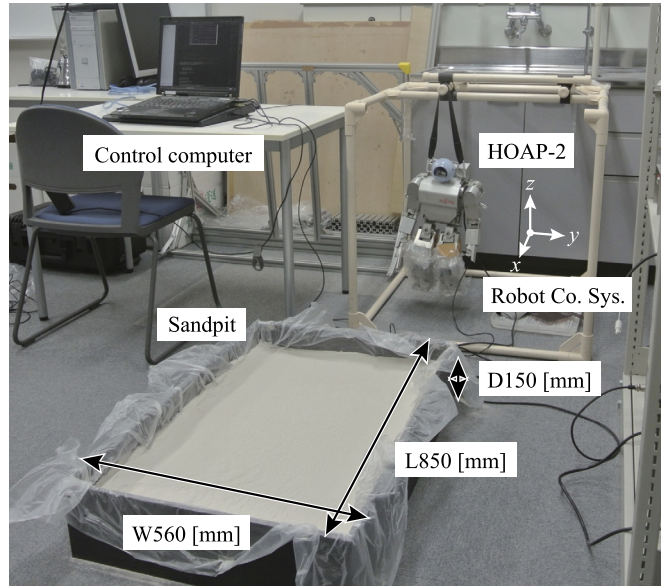


FIGURE 7.7 Experimental setup for biped walking on sand.

position at the next step is calculated by

$$\Delta \mathbf{r}_{k,j+1} = \mathbf{K}_L \max(\delta \mathbf{r}_{g,j}(t)) + \lambda \Delta \mathbf{r}_{k,j} \quad (0 \leq t \leq T_{step}), \quad (7.14)$$

where  $\mathbf{r}_{k,j}$   $k \in \{Fr, Fl\}$  is the 2D position vector of the ground projection of the supporting foot ankle position at the  $j$ th step,  $\max(\delta \mathbf{r}_{g,j})$  is the maximum amount of deviation of the gCoM from the desired position during the  $j$ th step,  $\mathbf{K}_L$  is a diagonal gain matrix, and  $\lambda$  is a diagonal forgetting factor matrix. The first term on the r.h.s. compensates the deviation of the gCoM, while the second term contributes to the reduction of the accumulated deviation.

### 7.3.2 Experiments of Walking on Sand

Fig. 7.7 shows the experimental setup. A small-size humanoid robot HOAP-2 manufactured by Fujitsu Automation Ltd. was used in the experiments. The height of the robot is 500 mm and the weight is 7 kg. The sampling period was set at 1 ms. The legs were covered with plastic sheet for dust proofing. The dimensions of the experimental sand pool were  $850 \times 560 \times 150$  mm (length  $\times$  width  $\times$  depth). Silica sand was used with a particle diameter of about  $0.01 \sim 0.04$  mm.

The foot prints were designed as described in Section 7.2.1, with the parameters  $L_x = 15$  mm,  $L_y = 78$  mm, and  $L_\theta = 0^\circ$  (see Fig. 7.3). The robot walked 28 steps forward and eight steps in place, and then halted. Based on the foot prints, the CPs at the end of each step  $\mathbf{r}_{ex,eos}^i$  were designed. The duration of the step,  $T_{step}$ , was set at 0.4 s. The threshold for the landing position control was set as  $\delta \mathbf{r}_g^{th} = [2.0 \ 6.0]^T$  (mm).

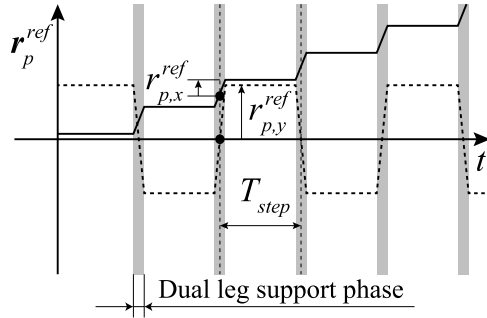


FIGURE 7.8 Design of reference ZMP trajectories.

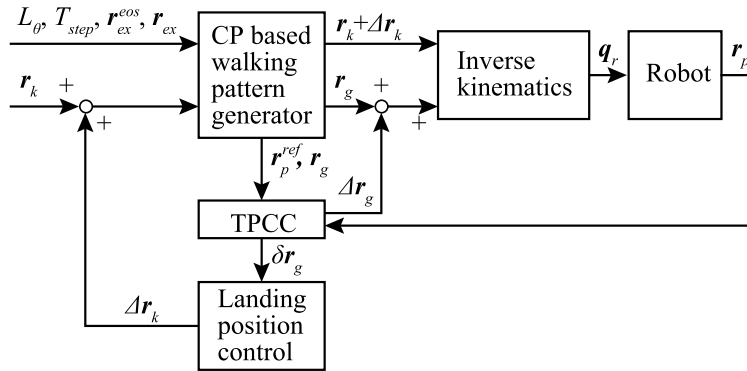
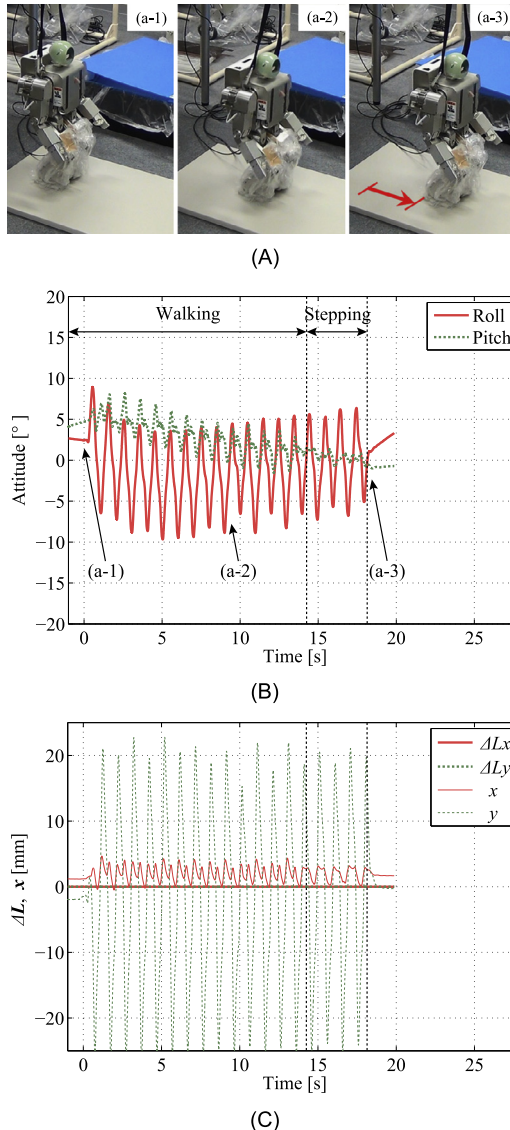


FIGURE 7.9 Block diagram of the control system of biped walking on sand.

The gait was generated on-line in the way described in Section 7.2.2. The designed reference CoP is plotted in Fig. 7.8. The simplified TPCC relations (5.43) and (5.44) were applied to the robot to stabilize its walking. Experiments with and without the landing position control in (7.14) were performed to verify the effectiveness. With landing position control, the forgetting factor  $\lambda$  was set to 0.7 for both the  $x$ - and the  $y$ -direction. The block diagram of the control system is shown in Fig. 7.9.

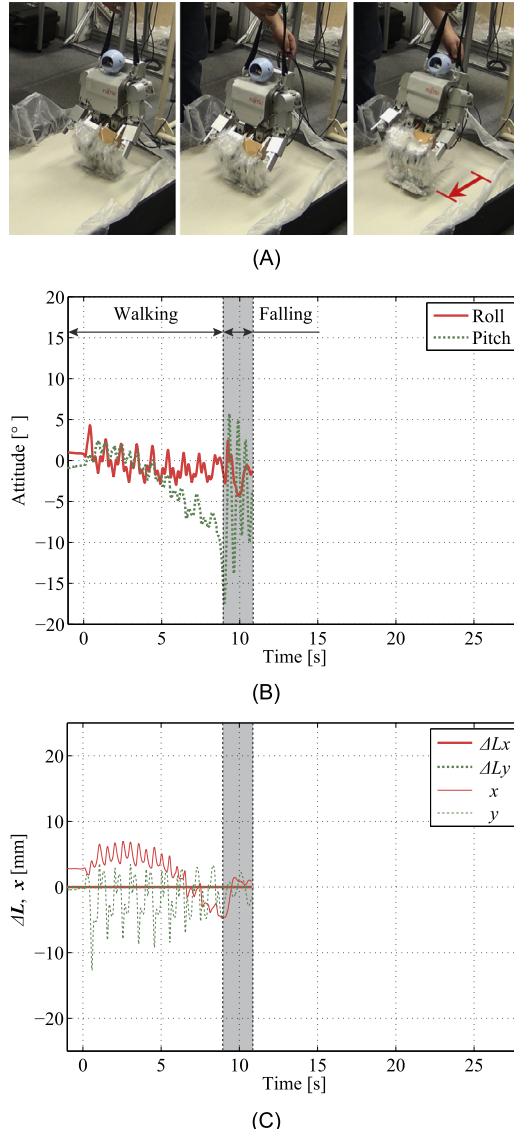
Fig. 7.10 shows the experimental results of walking on a flat floor (on a metal plate) without landing position control ( $\Delta r_k = 0$  in Fig. 7.10C). In biped walking, the humanoid robot laterally sways its body; hence lateral swaying of the CoM is seen in Fig. 7.10C. The lateral and rolling motions were kept in the constant range and the robot could stably walk, step, and stop.

Fig. 7.11 shows the experimental results of walking on sand without landing position control. As seen in Fig. 7.11B, approximately after the 10th step (about 5 s), the pitch angle rapidly increased (the robot tilted backward) and at the 18th step the robot fell down backward, despite the TPCC stabilizing approach. The same experiments were performed several times; however, in all experiments the robot could not stably walk on sand without landing position control.



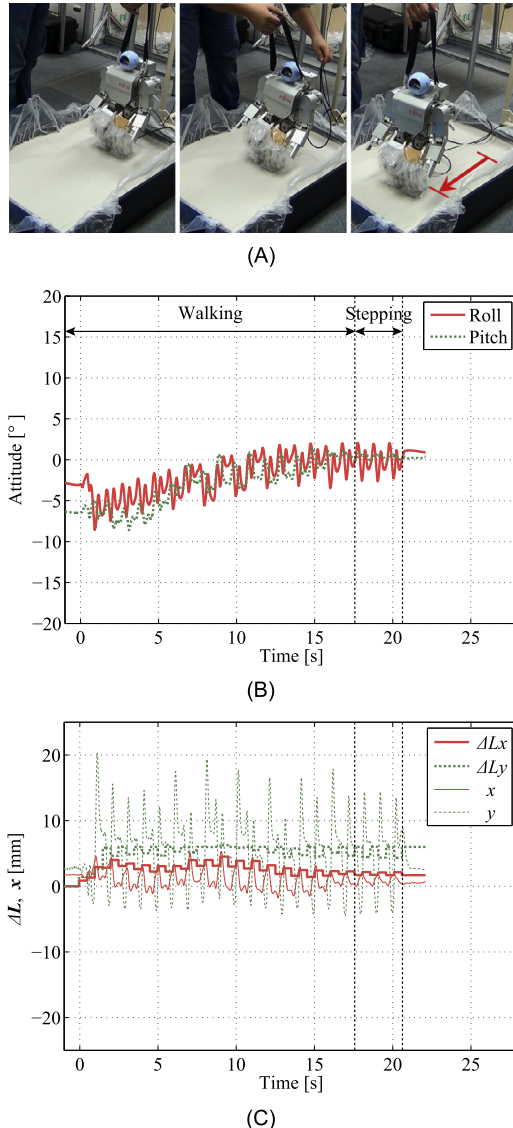
**FIGURE 7.10** Walking on a floor without the landing position control. (A) Snapshots of the experiment. (B) Roll and pitch angles. (C) CoM trajectory and modification of the landing position.

Fig. 7.12 shows the experimental results of walking on sand with landing position control. As seen in Fig. 7.12C, the desired deviation of the landing position  $\Delta r_k$  was calculated and then applied to the robot. As seen in Fig. 7.12B, the landing position control successfully compensated the deviation of the gCoM; consequently the divergence of the roll and pitch angles was well suppressed.



**FIGURE 7.11** Walking on sand without the landing position control. (A) Snapshots of the experiment. (B) Roll and pitch angles. (C) CoM trajectory and modification of the landing position.

In order to verify whether the landing position control is effective even on a flat floor, an experiment of walking on a metal plate with landing position control was performed. Fig. 7.13 shows the results. Compared with the results shown in Fig. 7.10, it seems that the landing position control contributes to suppress the lateral swaying motion. Because of the elasticity of the roll joints at the ankles and hips, the robot tends to tilt inside (toward the



**FIGURE 7.12** Walking on sand with landing position control. (A) Snapshots of the experiment. (B) Roll and pitch angles. (C) CoM trajectory and modification of the landing position.

swing leg). As a result, the swing foot tends to land slightly before the expected landing time, and hence *kicks* the floor. This *kicking* motion enlarges the rolling of the body, as seen in Fig. 7.10B, which ideally should be zero. It is assumed that the orbital energy is decreased by changing the landing position, and hence the *kicking* effect is suppressed.

The experimental results are shown in Video 7.3-1 [62].

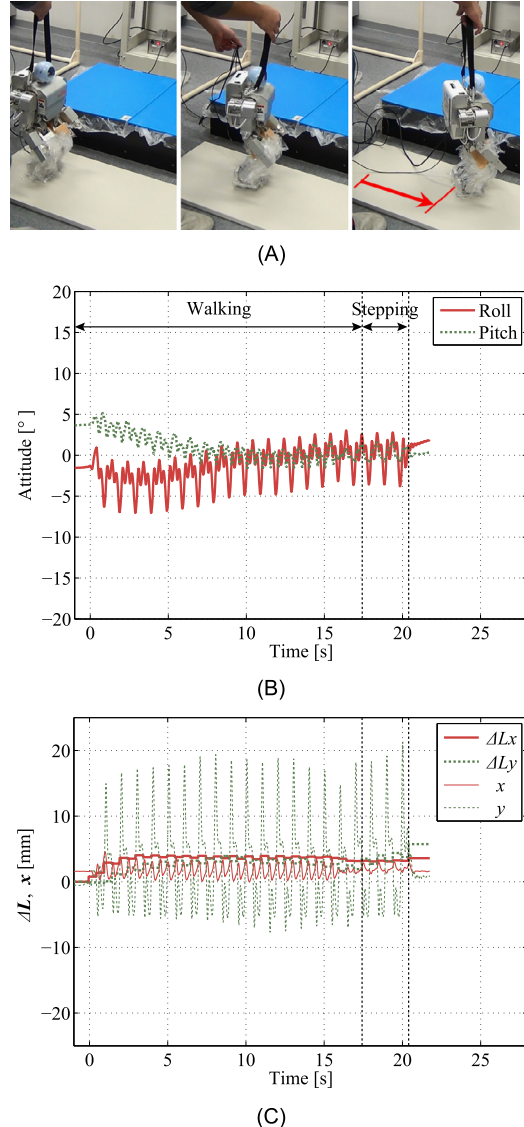
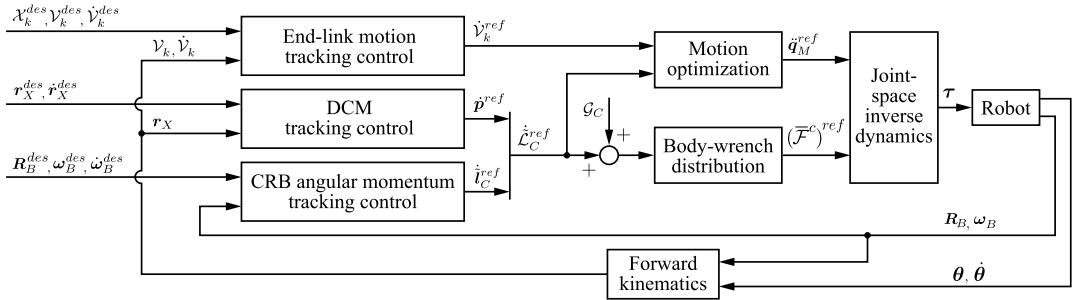


FIGURE 7.13 Walking on a hard floor with landing position control. (A) Snapshots of the experiment. (B) Roll and pitch angles. (C) CoM trajectory and modification of the landing position.

### 7.3.3 Summary and Discussion

This section presented a way to realize biped walking of humanoid robots on loose soil. The CP-based gait generation, TPCC, and landing position control were implemented with the humanoid robot HOAP-2 walking on sand. Those controllers are easy to implement and



**FIGURE 7.14** Block diagram of the VRP/DCM dynamic gait generation and walking controller for irregular terrain based on the VRP-GI body wrench distribution approach. The structure is identical with that of the motion/force controller in Fig. 5.29.

are effective for biped walking on loose soil, such as sand, as experimentally validated in Section 7.3.2.

## 7.4 GAIT GENERATION FOR IRREGULAR TERRAIN AND VRP-GI-BASED WALKING CONTROL

The ICP-based dynamic gait generation and walking control method described in Section 7.2 is limited to flat-ground environments. The method can be adopted to gait generation for irregular terrain in 3D by employing the DCM analysis based on the eCMP and VRP concepts (cf. Section 5.6.2). In this section, an implementation of two gait generation approaches, referred to as the “Continuous Double-Support” (CDS) and “Heel-to-Toe” (HT) gait generation, [20,21] will be described. These approaches ensure continuous GRFs that can be computed in real-time. The HT approach facilitates the so-called toe-off gait, whereby the support foot is allowed to roll around the BoS boundary at the toe. Such a motion is useful to avoid the stretched-knee kinematic singularity that occurs in a gait with a larger step width or while ascending/descending a staircase with a larger step height.

The controller shown in Fig. 7.14 will be used as the walking controller. Note that the controller’s structure is identical with that of the motion/force controller in Fig. 5.29. The VRP generalized inverse (VRP-GI) (cf. Section 5.10.5) will be used to distribute the body wrench during the double-stance (DS) phase and to facilitate smooth transitions between the single-stance (SS) and DS phases. The employment of the VRP-GI is computationally efficient; the wrench distribution problem can be solved much faster [44] than with a “conventional” approach based on iterative optimization (see e.g. [66,116]).

### 7.4.1 Continuous Double-Support (CDS) Gait Generation

Recall that the ICP gait generation method in Section 7.2 was based on control inputs in terms of the desired CoPs  $r_P^{des,i}$  that remain fixed within the foot BoS during the step. The same approach is used in CDS-based gait generation. Instead of desired CoPs, the control

inputs are determined now as desired VRPs, i.e.

$$\mathbf{r}_{vvp}^{des, i} = \mathbf{r}_a^{des, i} + [0 \ 0 \ \bar{z}_{vvp}]^T + \mathbf{R}_a^{des, i} [0 \ \bar{y}_{vvp} \ 0]^T. \quad (7.15)$$

Here  $\mathbf{r}_a^{des, i}$  are the ankle positions at the preplanned footprints. The last term on the r.h.s. is related to the setting of the dynamic stability margin in the envisioned VRP-GI body wrench distribution approach. As explained in Section 5.10.4, to minimize the generated foot moments (which is desirable from the viewpoint of walking control) the dynamic stability margin should be set between the ankle joints. But in this case, a zero weight will be generated by (5.123), which leads to rank deficiency of the VRP-GI. To avoid this, the desired VRP should not pass exactly above the ankles but nearby. To this end, a small offset  $\bar{y}_{vvp} > 0$  is introduced;  $\mathbf{R}_a^{des, i}$  denotes the rotation matrix for the desired foot orientation.

Next, the desired DCM is determined by reverse-order recursion, i.e.

$$\mathbf{r}_X^{des, i} = e^{-\frac{T_{step}}{T_X}} (\mathbf{r}_X^{des, i+1} - \mathbf{r}_{vvp}^{des, i}) + \mathbf{r}_{vvp}^{des, i}, \quad (7.16)$$

where  $T_X = 1/\bar{\omega}_X = \sqrt{\bar{z}_{vvp}/g}$  is the time constant of the DCM dynamics. The reference DCM trajectories can then be obtained as

$$\mathbf{r}_X^{des, i}(t) = e^{\frac{t-T_{step}}{T_X}} (\mathbf{r}_X^{des, i+1} - \mathbf{r}_{vvp}^{des, i}) + \mathbf{r}_{vvp}^{des, i}, \quad (7.17)$$

$$\dot{\mathbf{r}}_X^{des, i}(t) = \frac{1}{T_X} (\mathbf{r}_X^{des, i}(t) - \mathbf{r}_{vvp}^{des, i}), \quad (7.18)$$

for  $0 \leq t \leq T_{step}$ .

Assuming a stationary initial state at Step  $i = 0$ , s.t.  $\mathbf{r}_X^{des, 0} = \mathbf{r}_C(0)$ , the initial desired VRP is calculated from (7.16) as

$$\mathbf{r}_{vvp}^{des, 0} = \frac{1}{1 - e^{-\frac{T_{step}}{T_X}}} \mathbf{r}_C(0) + \frac{1}{1 - e^{\frac{T_{step}}{T_X}}} \mathbf{r}_X^{des, 1}. \quad (7.19)$$

The above relations are valid for a gait whereby the swing and support foot exchange instantaneously. They can be used in gait generation but the resulting trajectories will be discontinuous. To alleviate this problem, a DS phase is introduced. Denote by  $T_{DS}$  the DS time interval. To make use of the above notation,  $T_{DS}$  is divided into subintervals, i.e.  $T_{DS} = T_{DS}^{init} + T_{DS}^{end}$ ;  $T_{DS}^{init} = \alpha_{DS}^{init} T_{DS}$  and  $T_{DS}^{end} = (1 - \alpha_{DS}^{init}) T_{DS}$  stand for the time intervals before and after the (imaginary) instantaneous transition, and  $0 \leq \alpha_{DS}^{init} \leq 1$  is constant. In the following simulations  $\alpha_{DS}^{init} = 0.5$  will be used, as suggested in [20,21]. The desired DCM states at the end and the beginning of the DS phase can then be determined as

$$\mathbf{r}_{X, DS^{end}}^{des, i} = e^{\frac{T_{DS}^{end}}{T_X}} (\mathbf{r}_X^{des, i} - \mathbf{r}_{vvp}^{des, i}) + \mathbf{r}_{vvp}^{des, i}, \quad (7.20)$$

$$\dot{\mathbf{r}}_{X, DS^{end}}^{des, i} = \frac{1}{T_X} (\mathbf{r}_{X, DS^{end}}^{des, i} - \mathbf{r}_{vvp}^{des, i}) \quad (7.21)$$

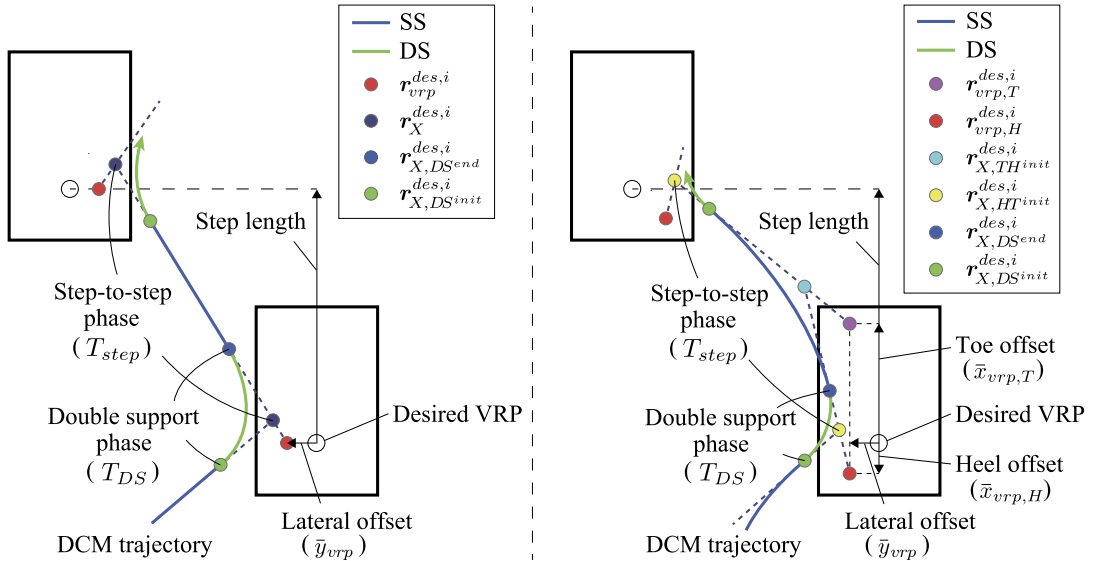


FIGURE 7.15 DCM trajectory generation methods [20]. Left (A): Continuous double-support (CDS). Right (B): Heel-to-toe (HT).

and

$$\mathbf{r}_{X, DS^{init}}^{des,i} = e^{-\frac{T_{DS}^{init}}{T_X}} (\mathbf{r}_X^{des,i} - \mathbf{r}_{vvp}^{des,i-1}) + \mathbf{r}_{vvp}^{des,i-1}, \quad (7.22)$$

$$\dot{\mathbf{r}}_{X, DS^{init}}^{des,i} = \frac{1}{T_X} (\mathbf{r}_{X, DS^{init}}^{des,i} - \mathbf{r}_{vvp}^{des,i-1}), \quad (7.23)$$

respectively. The above two boundary states are connected via a fifth-order spline to generate the desired DCM trajectories during the DS phase. The CDS gait generation procedure is outlined in Fig. 7.15A.

#### 7.4.2 Heel-to-Toe (HT) Gait Generation

To generate a toe-off-type gait, instead of the desired VRP  $\mathbf{r}_{vvp}^{des,i}$  used in the CDS approach, two desired VRPs will be employed:  $\mathbf{r}_{vvp,H}^{des,i}$  and  $\mathbf{r}_{vvp,T}^{des,i}$  for the heel and toe, respectively. They are obtained with the help of offsets  $\bar{x}_{vvp,H}$  and  $\bar{x}_{vvp,T}$ , respectively (cf. Fig. 7.15B), i.e.

$$\mathbf{r}_{vvp,H}^{des,i} = \mathbf{r}_a^{des,i} + [0 \ 0 \ \bar{z}_{vvp}]^T + \mathbf{R}_a^{des,i} [\bar{x}_{vvp,H} \ \bar{y}_{vvp} \ 0]^T, \quad (7.24)$$

$$\mathbf{r}_{vvp,T}^{des,i} = \mathbf{r}_a^{des,i} + [0 \ 0 \ \bar{z}_{vvp}]^T + \mathbf{R}_a^{des,i} [\bar{x}_{vvp,T} \ \bar{y}_{vvp} \ 0]^T. \quad (7.25)$$

The desired DCMs can then be determined by the following reverse-order recursions:

$$\mathbf{r}_{X, TH^{init}}^{des,i} = e^{-\frac{T_{TH}}{T_X}} (\mathbf{r}_{X, HT^{init}}^{des,i+1} - \mathbf{r}_{vvp,T}^{des,i}) + \mathbf{r}_{vvp,T}^{des,i}, \quad (7.26)$$

$$\mathbf{r}_{X,HT^{init}}^{des,i} = e^{-\frac{T_{HT}}{T_X}} (\mathbf{r}_{X,HT^{init}}^{des,i} - \mathbf{r}_{vRP,H}^{des,i}) + \mathbf{r}_{vRP,H}^{des,i}, \quad (7.27)$$

where  $T_{HT} = \alpha_{HT} T_{step}$  and  $T_{TH} = (1 - \alpha_{HT}) T_{step}$ ,  $0 \leq \alpha_{HT} \leq 1$ .

As in the CDS algorithm, assume a stationary initial state at Step  $i = 0$ . The initial desired VRP can then be calculated as

$$\mathbf{r}_{vRP,T}^{des,0} = \frac{1}{1 - e^{-\frac{T_{TH}}{T_X}}} \mathbf{r}_C(0) + \frac{1}{1 - e^{\frac{T_{TH}}{T_X}}} \mathbf{r}_{X,HT^{init}}^{des,1}. \quad (7.28)$$

The desired DCM states at the end and the beginning of the DS phase can then be determined as

$$\mathbf{r}_{X,DS^{end}}^{des,i} = e^{\frac{T_{DS}^{end}}{T_X}} (\mathbf{r}_{X,HT^{init}}^{des,i} - \mathbf{r}_{vRP,H}^{des,i}) + \mathbf{r}_{vRP,H}^{des,i}, \quad (7.29)$$

$$\dot{\mathbf{r}}_{X,DS^{end}}^{des,i} = \frac{1}{T_X} (\mathbf{r}_{X,DS^{end}}^{des,i} - \mathbf{r}_{vRP,H}^{des,i}) \quad (7.30)$$

and

$$\mathbf{r}_{X,DS^{init}}^{des,i} = e^{-\frac{T_{DS}^{init}}{T_X}} (\mathbf{r}_{X,HT^{init}}^{des,i} - \mathbf{r}_{vRP,T}^{des,i-1}) + \mathbf{r}_{vRP,T}^{des,i-1}, \quad (7.31)$$

$$\dot{\mathbf{r}}_{X,DS^{init}}^{des,i} = \frac{1}{T_X} (\mathbf{r}_{X,DS^{init}}^{des,i} - \mathbf{r}_{vRP,T}^{des,i-1}), \quad (7.32)$$

respectively. The above two boundary states are connected via a fifth-order spline to generate the desired DCM trajectories during the DS phase. The HT gait generation procedure is outlined in Fig. 7.15B.

### 7.4.3 Simulation

A small-sized humanoid robot model with parameters similar to those of the HOAP-2 robot [25] was used in the Chorenoid environment [87]. For the numbering of the joints and other relevant data see Section A.1. The results from three simulations with the HT algorithm will be presented. The following parameters were used:  $T_{step} = 0.5$  s,  $T_{DS} = 0.1$  s,  $\bar{y}_{vRP} = 15$  mm,  $\bar{x}_{vRP,T} = 25$  mm,  $\bar{x}_{vRP,H} = -15$  mm,  $\alpha_{DS} = \alpha_{HT} = 0.5$ , and the step length and height were 100 and 20 mm, respectively. The desired rotation of the trunk (the base link) is the initial (zero) one. The feedback gains for the CRB trajectory were  $K_X = 300 = K_{OB}$ ,  $K_{\omega B} = 50$ . The P and D feedback gains for the swing foot trajectory tracking were set at 3000 and 500, respectively. The arm motion was controlled by joint damping only. The damping was set at 100 for each arm joint.

The first simulation demonstrates walking on a flat floor, without toe-off. The results are shown in Video 7.4-1 [81] and Fig. 7.16. Apparently, the generated dynamic gait and the controller ensure a stable performance.

The second simulation demonstrates the ascending/descending of a staircase. The height of the stair steps was 20 mm. The maximum height of the swing foot trajectory was set at 10 mm above the ground. The results are shown in Video 7.4-2 [82] and Fig. 7.17. Although there is a slight difference in the CoP fluctuation while ascending and descending, overall the walking is quite stable.

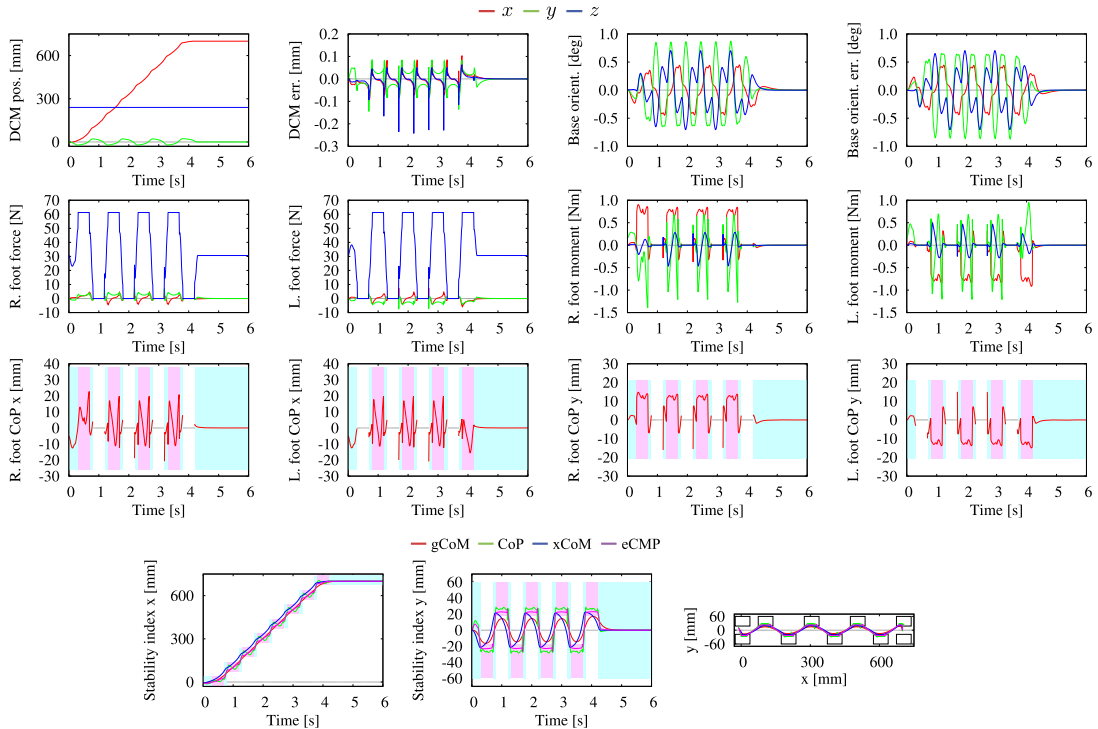
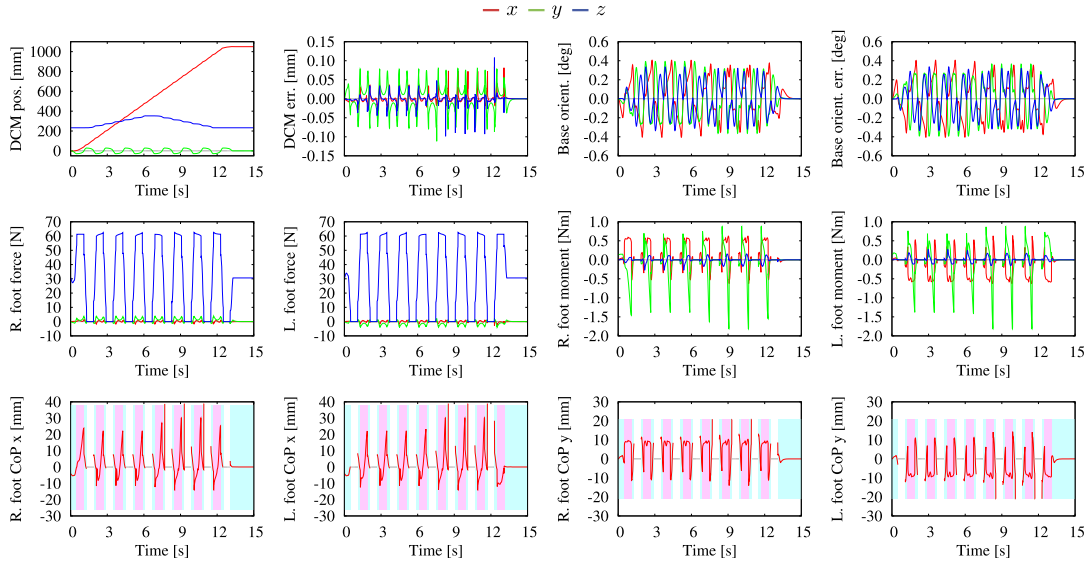


FIGURE 7.16 Dynamic straight walking on a flat floor. The light-blue/pink areas signify the double/single-support phases, respectively.

The third simulation is for walking on a flat floor with toe-off. The result is shown in Video 7.4-3 [83]. This simulation also demonstrates very stable dynamic walking.

## 7.5 SYNERGY-BASED MOTION GENERATION

Research on motor control in the field of neurophysiology has revealed that determining the appropriate muscle activation to achieve a given motion objective is a fairly complex task. The reasons, as pointed out in [19], are the high dimensionality of the search space and the nonlinear and dynamic nature of the transformation between the muscle activity and the movement. It has been hypothesized that this task is solved by the central nervous system (CNS) resorting to *muscle synergies* or muscle activation patterns. A muscle synergy induces a respective *movement synergy* (also called a “kinematic synergy,” a “motion pattern” or a “motion primitive”), i.e. a variation in the posture of a human or an animal whereby the movement in the body segments is coordinated in a specific way [71]. The above hypothesis has been confirmed via experimental results [19]. The results have shown that the motor control in animals and humans alike is organized in a modular way, s.t. various behaviors are determined either by linear combinations of the same synergies, or by specific synergies. In this way, the load on the CNS can be significantly decreased.



**FIGURE 7.17** Ascending/descending a staircase. The light-blue/pink areas signify the double/single-support phases, respectively.

The term “synergy” was introduced in the field of robotics in the pioneering work [74], with regard to motion analysis/generation in the presence of kinematic redundancy. As discussed in Chapter 2, a kinematically redundant manipulator can achieve its end-link motion task with an infinite number of movements. To arrive at the desired unique movement, one or more additional subtasks have to be specified. It is preferable that the subtasks are specified in the lower-dimensional subspace of the redundant DoFs, rather than in the higher-dimensional joint space. Each redundant DoF yields a specific synergy that determines a movement pattern. A desirable complex movement pattern can be obtained by linear combinations of the synergies.

Kinematic synergies are useful not only in redundancy resolution, but also in dealing with kinematically singular manipulator configurations. As revealed by the analysis based on the Singularity-Consistent method [89] (cf. Section 2.5), *instantaneous* motion patterns emerge at such configurations. Furthermore, kinematic synergies have also been shown to be useful in specifying the manipulation tasks [8]. In the field of computer-based animation of articulated figures, the synergetic choreography approach in [120] deserves to be mentioned.

Kinematic synergies have also been employed in balance control of humanoid robots. With the method described in [29], postural variations that resemble the ankle and hip strategies used by humans in response to a perturbation can be generated. A discussion on kinematic synergies in relation to balance control, including the formal definition of a kinematic synergy as a *one-parameter* family of curves in joint space (i.e. a manifold), can be found in [31,32].

In the remaining part of this section, the focus will be on synergy-based motion generation for a humanoid robot. Synergy-based balance control will be discussed in Section 7.6 and Section 7.7.

**TABLE 7.1** Primitive motion synergies generated with a single command

Primitive motion synergy	$\mathcal{V}_M$	$\bar{\mathcal{V}}^m$	$\dot{\theta}_u$
P1 limb self-motion (internal-link motion with stationary CoM/base)	$= \mathbf{0}$	$= \mathbf{0}$	$\neq \mathbf{0}$
P2 end-link motion with stationary CoM/base	$= \mathbf{0}$	$\neq \mathbf{0}$	$= \mathbf{0}$
P3 CoM/base motion (fixed end links, no self-motion)	$\neq \mathbf{0}$	$= \mathbf{0}$	$= \mathbf{0}$

**TABLE 7.2** Combinations of synergies generated with multiple commands

Combinations of synergies	$\mathcal{V}_M$	$\bar{\mathcal{V}}^m$	$\dot{\theta}_u$
C1 whole-body motion with stationary CoM/base	$= \mathbf{0}$	$\neq \mathbf{0}$	$\neq \mathbf{0}$
C2 whole-body self-motion (internal-link and CoM/base motion)	$\neq \mathbf{0}$	$= \mathbf{0}$	$\neq \mathbf{0}$
C3 end-link and CoM/base motion	$\neq \mathbf{0}$	$\neq \mathbf{0}$	$= \mathbf{0}$
C4 whole-body motion	$\neq \mathbf{0}$	$\neq \mathbf{0}$	$\neq \mathbf{0}$

### 7.5.1 Primitive Motion Synergies

The constraint-consistent instantaneous-motion inverse kinematics solutions for a humanoid robot, expressed in terms of the base and the mixed quasivelocity, are given in (2.98) and (2.133), respectively. The latter solution will be implemented below for the synergy-based motion generation. Recall that this solution has an advantage that enables the robot to attain a completely erected posture, as shown with the example in Section 2.11.4.

Each of the three components of solution (2.133) determines a *primitive kinematic synergy*. This is apparent from the fact that the components are parametrized by lower-dimensional inputs. The input in the first component,  $\dot{\theta}^c$ , is the mixed-quasivelocity twist  $\mathcal{V}_M$ . This component determines the CoM/base-link movement synergy. The second component,  $\dot{\theta}^m$ , specifies a synergy for the end-link movements along the unconstrained motion directions via the input  $\bar{\mathcal{V}}^m$ . The third component,  $\dot{\theta}^n$ , determines the self-motion synergy. The three synergies are called primitive since they are generated by a single command input, as shown in Table 7.1.

### 7.5.2 Combinations of Primitive Synergies

As already pointed out, primitive motion synergies can be combined to obtain complex movement patterns. The primitive synergies in Table 7.1 are combined to obtain the four movement patterns shown in Table 7.2. The synergies and their combinations can be related to typical motion tasks. For example, the three stationary-CoM/base motion synergies/patterns (P1, P2, and C1, obtained with  $\mathcal{V}_M = \mathbf{0}$ ) are useful for dual-stance (DS) erected or sitting postures, whereby only the arms move. When the hands are immobilized (e.g. when the hands are placed on a table s.t.  $\bar{\mathcal{V}}_H^m = \mathbf{0}$ ), the limb self-motion synergy P1 can be used to adjust the arm configurations, e.g. to apply optimal contact forces while standing up. A movement pattern for standing up can be realized with the CoM/base-motion synergy P3 or the whole-body self-motion pattern C2.

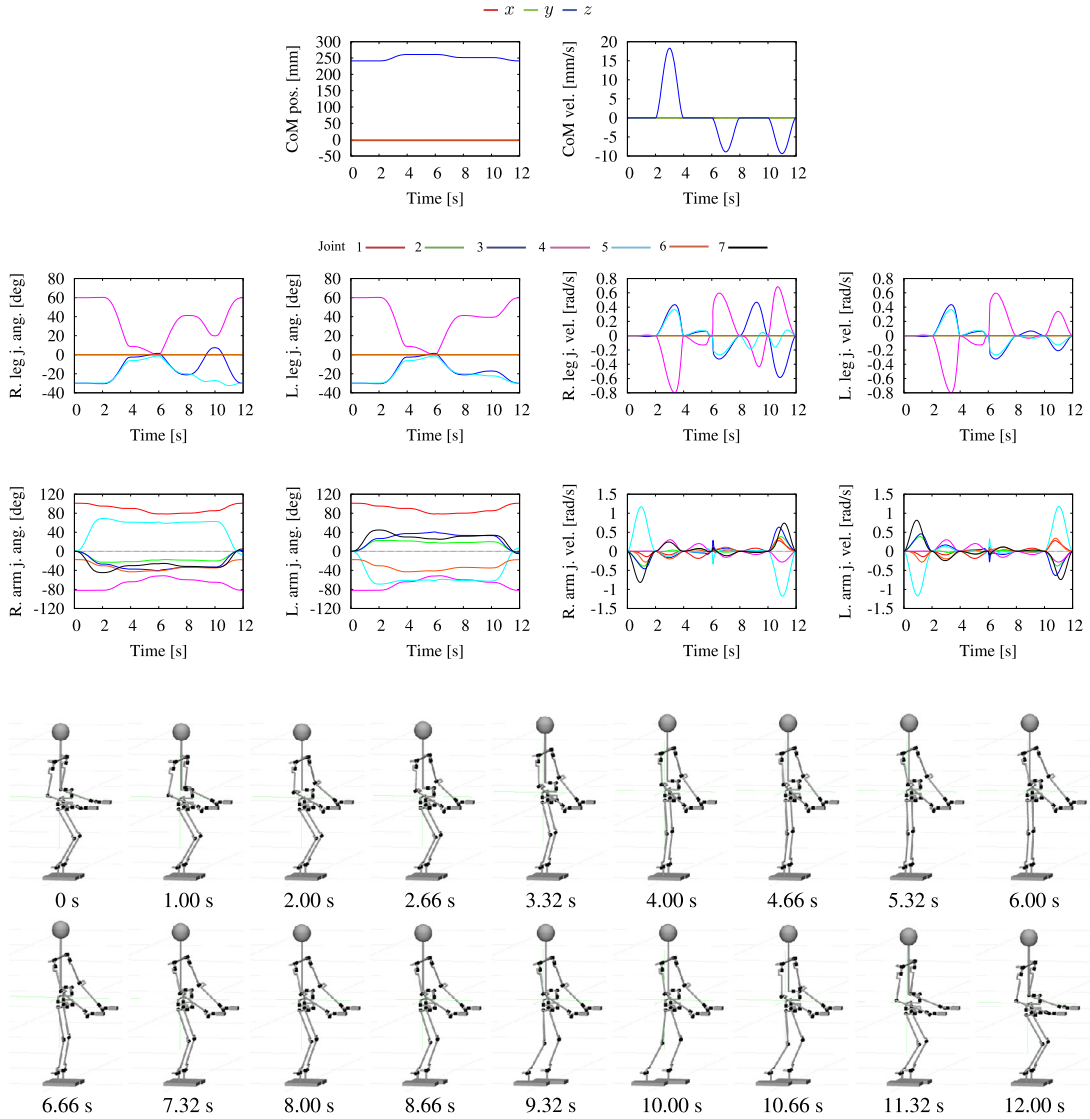


FIGURE 7.18 Synergy-based motion generation. The position and velocity of the CoM are shown in the upper-row graphs. The joint angles and their rates for the legs and arms are shown in the middle and lower rows, respectively. Snapshots from the animated motion are shown at the bottom.

Video 7.5-1 [106] demonstrates the movements of a small-sized humanoid robot<sup>2</sup> generated with primitive motion synergies and their combinations. The CoM position/velocity and the joint angle/angular velocity graphs are shown in Fig. 7.18. Snapshots from the sim-

<sup>2</sup> The parameters of the model were derived from a HOAP-2 robot [25] (see Section A.2).

ulation are shown at the bottom of the same figure. The following synergies/patterns are performed:

1. 0 ~ 2 s arm self-motion (P1);
2. 2 ~ 4 s CoM/base upward motion (P3);
3. 4 ~ 6 s hands sliding along an invisible horizontal surface, with stationary CoM/base (C3);
4. 6 ~ 8 s CoM/base downward motion (P3);
5. 8 ~ 10 s right-leg sliding motion with stationary CoM/base (P2);
6. 10 ~ 12 s whole-body motion for returning to the initial posture (C4).

Note that the contacts at the feet/hands have been set as frictionless to allow the robot to adjust the postures of its limbs by sliding on the closure-link surfaces (i.e. the floor surface for the feet and the invisible table surface for the hands) in the desirable way. Note also that while the hands slide during Phase 3, the posture becomes fully erected. This is also apparent from the knee-joint graphs in Fig. 7.18 (drawn in purple color). No instabilities are observed at this posture because the mixed quasivelocity notation was employed. This would not be the case if the notation in terms of the base quasivelocity were used. The motion in the final, sixth phase is composed of all previous synergies, but executed in the reverse direction. As apparent from the graphs, smooth movements can be generated with this method.

### 7.5.3 Multiple Synergies Generated With a Single Command Input

There are special cases when multiple synergies can be invoked with a single command input. Assume a humanoid robot with redundant arms, the hands being constrained to keep their positions on a table. The initial posture of the robot is with slightly bent knees. The CoM/base upward motion command (P3) first invokes upward CoM/base motion, as expected. When the legs become fully extended, the base cannot move anymore upward. But the CoM can do so, by (automatically) invoking self-motion in the arms. This type of behavior can be seen in Video 7.5-2 [127].

## 7.6 SYNERGY-BASED REACTIVE BALANCE CONTROL WITH PLANAR MODELS

---

In Section 5.13 three balance controllers were introduced capable of accommodating external disturbances via a whole-body compliance. It was noted, though, that such controllers can accommodate relatively weak disturbances only. This limitation stems from the constant PD feedback terms in the CRB spatial dynamics control component; the error bounds cannot be set sufficiently low to allow for larger postural variations. Note that a larger postural variation is needed to accommodate a larger disturbance. The reactive balance controller should ensure sufficiently large postural variations without deteriorating the balance. As will be shown in what follows, motion synergies can be used to generate such postural variations.

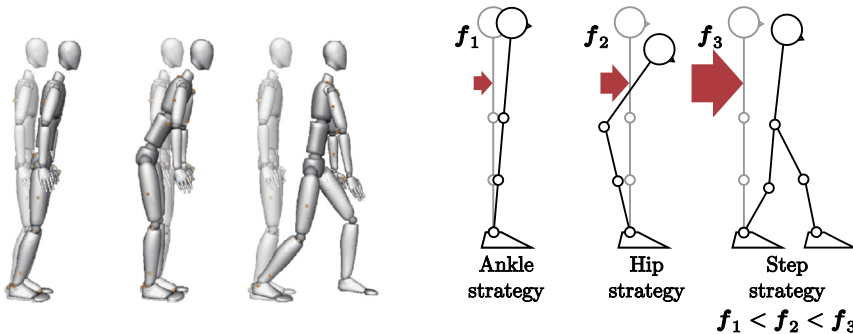


**FIGURE 7.19** Sagittal-plane ankle, hip, and step reactive strategies in response to an external force acting on the back. The ankle strategy is initialized by a weak disturbance that is accommodated by motion in the ankle joints and displacement of the CoM within the BoS. The hip strategy is initialized by a disturbance of a mid-level magnitude; it is realized by bending the upper body with prevailing motion in the hip joints. Sometimes, this strategy is characterized as an antiphase excursion in the ankle and hip joints. The stepping strategy is initialized by a strong disturbance leading to a change in the BoS (reactive stepping).

### 7.6.1 Motion Synergies for Balance Control Used by Humans

Researchers in the fields of biomechanics and physical therapy have paid attention to the balance recovery strategies used by humans to assess balance disorders [102,118,117,42]. For the purpose of analysis, most often simple models on the sagittal and lateral planes (cf. Fig. 2.1) have been adopted. A brief overview of the results will be presented below.

#### **Sagittal Plane**

When a healthy person standing upright is subjected to an external disturbance generated by horizontal perturbations in the support surface, he or she reacts either with the ankle or the hip synergy [102,42]. When the support surface is sufficiently large, postural balance is achieved with the ankle synergy. Thereby, the disturbance accommodation and the equilibrium restoration are done via movements in the ankle joints mainly. The hip synergy, on the other hand, is invoked when the person stands on a support surface shortened in relation to the foot length. This synergy produces a horizontal shear force against the support surface, with little or no motion in the ankles but with a predominant motion in the hips. In addition to the ankle and hip strategies, a third one, the so-called *stepping or stumbling strategy*, was also identified. This strategy is invoked when certain boundary values (in position and/or velocity) during the hip strategy are exceeded. The three reactive strategies are illustrated in Fig. 7.19.

#### **Lateral Plane**

A conceptual model for investigating the role of the CNS in the performance of swaying movements within the lateral plane<sup>3</sup> was proposed in [53]. A four-link model was used to

<sup>3</sup> Also referred to as a frontal or coronal plane.

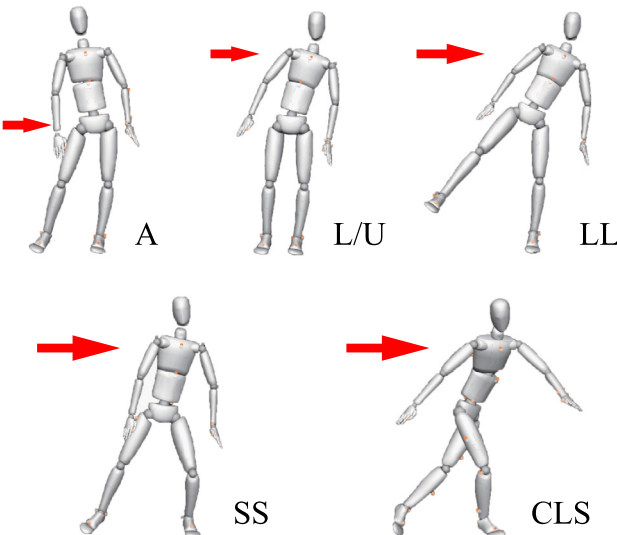


**FIGURE 7.20** Lateral-plane reactive response patterns. *A*, Ankle. *L/U*, Load/Unload. *LL*, Lift-Leg. *SS*, Side-Step. *CLS*, Cross-Leg-Step. Patterns *A*, *L/U*, *SS*, and *CLS* are known from studies in the field of biomechanics [100,79,96]. Pattern *LL* was identified in [126]; it also appears in a humanoid robot study [41].

derive parallel-leg motion patterns with predominant motion in the ankle/hip joints. A more detailed study [100] came to the conclusion that the lateral-plane ankle strategy is used when the disturbance is relatively small (e.g. when applied at the pelvis). With a larger disturbance, acting e.g. at the shoulder, the response is with the so-called *load/unload synergy*. Also, it was mentioned that a step could be invoked to maintain the balance, when the disturbance grows even larger. In [79] and [96], two main protective-step patterns were identified: the loaded side-step and the unloaded crossover-step strategies in response to invariant disturbances. In [126] it was observed that when the disturbance invoking the load/unload synergy grows larger, the contact at the unloaded foot is lost, resulting in the so-called *lift-leg* synergy. This synergy was also obtained with a humanoid robot model [41]. The lateral plane balance strategies confirmed in [126] are shown in Fig. 7.20.

The reaction/recovery motion patterns used by humans have been examined experimentally via simulations. Some of the patterns have been implemented with real robots. Fairly complex full-body models have been introduced at an early stage. Solutions that can accommodate not only weak, but also medium disturbances, were obtained with the linear [29] and quadratic [68] programming approaches. Most studies have been based on simple models, though, mainly in the sagittal plane [103,6,122]. In the remaining part of this section, the focus will be on the implementation of synergies that do *not require a change in the BoS*. Such synergies are used to accommodate a disturbance of medium magnitude. Synergies that are typically used to respond to a larger disturbance require a change in the BoS (e.g. as the sagittal-plane step strategy or the lateral-plane lift-leg strategy). These types of synergies will be discussed in Section 7.7.5.

### 7.6.2 RNS-Based Reactive Synergies

Given a statically stable posture with a sufficiently large stability margin, an infinite set of *large* postural variations for disturbance accommodation can be generated via a spatial momentum conservation approach, e.g. the Reaction Null-Space (RNS) method (cf. Section 4.9). Such variations, henceforth referred to as *RNS synergies*, are reactionless; they can ensure balance stability while conserving the initial (zero) spatial momentum. The conservation implies that a motion will be generated that keeps the CoM and the centroidal-moment point (CMP) fixed throughout the motion synergy. This is a somewhat conservative approach, but the balance controller is simple and yields robust performance, also with a position-controlled robot as will be shown below. In the following discussion, models composed of the legs and the trunk will be employed. Whole-body models that include arm motion will be discussed in Section 7.7. Furthermore, it will be assumed that the direction of the external disturbance does not pass through the CoM. This means that the disturbance can be accommodated mainly via rotations in the trunk/legs, without inducing a large variation in the CoM.

### 7.6.3 Sagittal-Plane Ankle/Hip Synergies

The ankle synergy is used to accommodate a relatively small disturbance. Thus, it can be realized with one of the whole-body compliance control approaches discussed in Chapter 5, e.g. the passivity-based gravity compensation (cf. Section 5.13.1, see also [48]). The ankle synergy can also be invoked in a straightforward manner with a simple linearized IP-on-foot model and an LQR controller [103]. The realization of the hip synergy, on the other hand, is somewhat more challenging. The ultimate goal is to design a balance controller that can invoke any of these two synergies depending on the magnitude of the disturbance. It is also desirable to accommodate possible variations in the disturbance, via smooth transitions between the two synergies.

The simplest model for the hip synergy is the double-IP-on-foot model with foot/leg/torso segments (cf. Fig. 7.21B). With this model, the hip synergy can be generated based on the RNS method, whereby the foot is designated as the root link of the floating-base system [92, 91]. The balance stability can be preserved under a disturbance *force* applied horizontally at the torso, provided the leg/torso force accommodating movements do not impose horizontal force and moment components at the foot. The foot will then remain stationary, s.t.  $v_{Bx} = 0 = \omega_B$ . In this case, the momentum conservation condition assumes the simple form  $\mathbf{J}_{\overline{CB}_x} \dot{\theta} = 0$ , where

$$\mathbf{J}_{\overline{CB}_x} = \begin{bmatrix} z_g & k_m l_g 2 \cos(\theta_1 + \theta_2) \end{bmatrix} \quad (7.33)$$

is the horizontal ( $x$ ) component of the CoM Jacobian,  $k_m = M_2/M$ ,  $M = M_1 + M_2$  denoting the total mass. The joint velocity vector is composed of the two joint rates (ankle and hip). Solving for the joint rates, one obtains the following set of *reactionless joint velocities*:

$$\{\dot{\theta}_{rl}\} = \{bn\}, \quad (7.34)$$

where  $b$  is an arbitrary scalar that parametrizes the hip synergy;  $\mathbf{n} \in \mathfrak{N}^2$  is a vector from the kernel of  $\mathbf{J}_{\overleftarrow{CB_x}}$ , i.e.

$$\mathbf{n} = \begin{bmatrix} n_1 \\ n_2 \end{bmatrix} = \begin{bmatrix} -M_2 l_{g2} \cos(\theta_1 + \theta_2) \\ (M_1 l_{g1} + M_2 l_1) \cos \theta_1 + M_2 l_{g2} \cos(\theta_1 + \theta_2) \end{bmatrix}. \quad (7.35)$$

This relation generates a vector field in the joint space that specifies the synergy.

The following relation for the joint rates in the hip synergy can then be obtained:

$$\dot{\theta}_{1h}^{ref} = \frac{n_1}{n_2} \dot{\theta}_{2h}^{ref}. \quad (7.36)$$

Here  $\dot{\theta}_{ih}^{ref}$ ,  $i = 1, 2$ , are reference joint rates for the hip strategy.

Next, consider the IP-on-foot model for the ankle synergy shown in Fig. 7.21A. The equation of motion is written as

$$Ml_g^2 \ddot{\theta}_1 - Mg x_g = \tau_1 - D_a \dot{\theta}_1 - K_a \theta_1. \quad (7.37)$$

Here  $l_g$  is the distance from the ankle to the CoM,  $x_g = l_g \sin \theta_1$  is the CoM ground projection,  $g$  is the gravity acceleration, and  $D_a$  and  $K_a$  are virtual damper/spring constants. Linearizing around the upright posture, the ankle torque can be replaced as  $\tau_1 \approx -Mg x_p$  (cf. (4.8)). The reference joint acceleration for the ankle can then be obtained as

$$\ddot{\theta}_{1a}^{ref} = \frac{1}{Ml_g^2} (Mg(x_g - x_p) - D_a \dot{\theta}_1 - K_a \theta_1). \quad (7.38)$$

The same relation can be used to obtain the reference joint acceleration for the hip joint in the hip synergy, under the simplified assumption that the torso segment represents a single IP, whereby the leg is instantaneously immobilized. Thus,

$$\ddot{\theta}_{2h}^{ref} = \frac{1}{M_2 l_{g2}^2} (M_2 g(x_g - x_p) - D_h \dot{\theta}_2 - K_h \theta_2). \quad (7.39)$$

Here  $C_h$  and  $K_h$  are virtual damper/spring constants for the torso; the rest of the parameters should be clear from Fig. 7.21. The joint accelerations are integrated to obtain the reference joint angle rates to be used as control inputs in the following equations.

The above ankle and hip synergies can be combined by considering the displacement of the CoM during the two synergies. During the ankle synergy, the gCoM is displaced within the BoS. During the hip strategy, the CoM is displaced only in the vertical direction, whereas its ground projection remains stationary (cf. Fig. 7.21B). The aim of the transition between the ankle (A) and hip (H) synergies is twofold. First, it should be ensured that hip motion is initialized in a timely fashion before  $x_g$  reaches the BoS boundary (A-H transition). Second, the gCoM should move back swiftly to the position of the erected posture, after the disturbance disappears. In order to ensure such movements, make use of

$$\dot{x}_g = \mathbf{J}_{\overleftarrow{CB_x}} \dot{\theta} \quad (7.40)$$

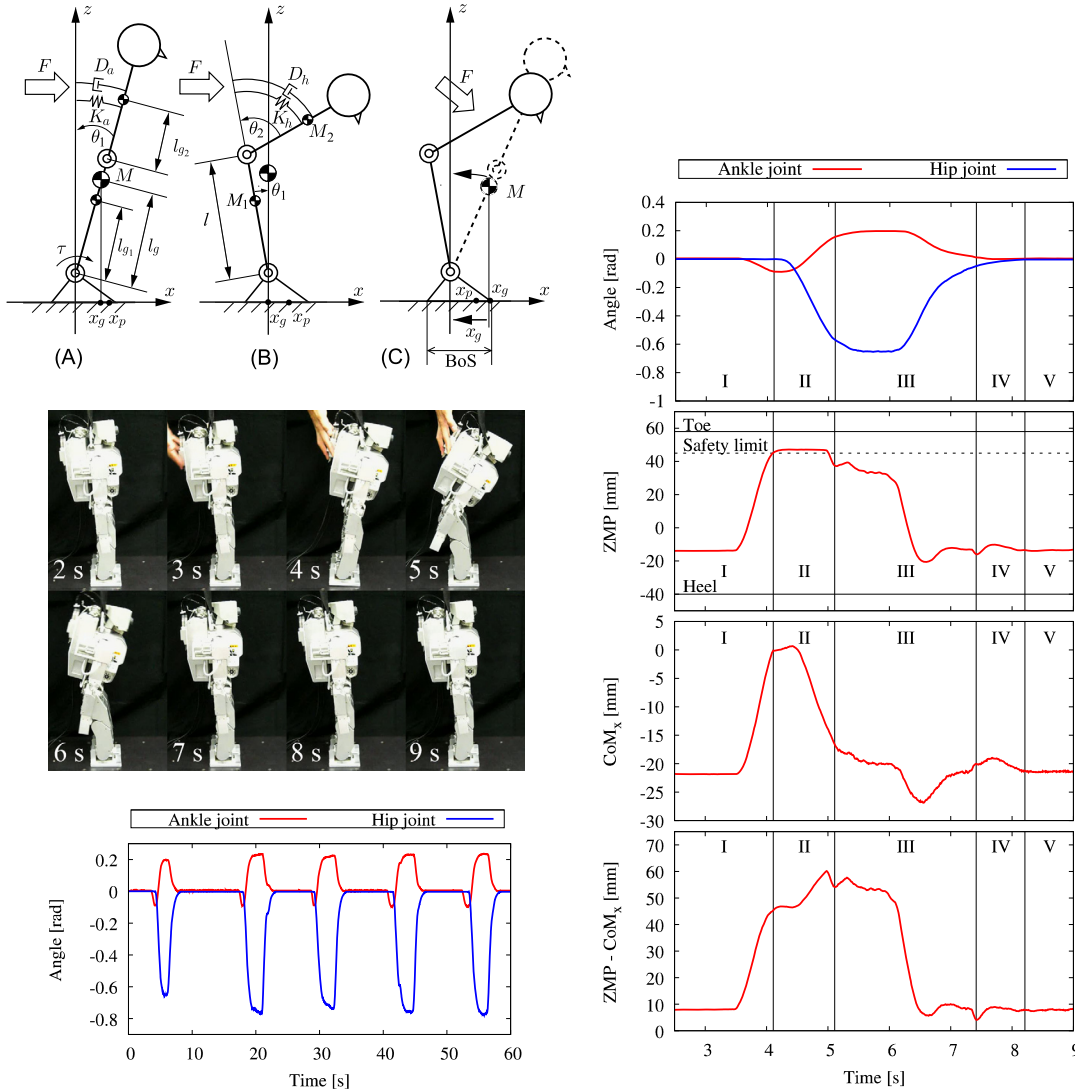


**FIGURE 7.21** Ankle-hip reaction synergies within the sagittal plane [57]. Left-top: models for the ankle (A) and hip (B) synergies and the transition (C). Left-middle: snapshots from the experiment. Left-bottom: joint angle data for five consecutive disturbances; Right: detailed data from the first disturbance cycle. The motion phases are enumerated according to Table 7.3;  $K_{(o)}/D_{(o)}$  are the virtual spring/damper variables.

with solution

$$\dot{\theta} = \mathbf{J}_{\overleftarrow{CB}_x}^+ \dot{x}_g + b\mathbf{n}. \quad (7.41)$$

Consider first the A–H transition phase. With the help of (7.33) and (7.35), (7.41) can be expanded in the following form:

TABLE 7.3 Motion phases and variables

Phase	Synergy	$\theta_1$	$\theta_2$	Variable of transition
I	Ankle (A)	(7.38)	–	–
II	A-H transition	(7.43) (7.44)	(7.39)	$x_p$
		$x_g^{des} : x_g^{lim} \xrightarrow{\text{spline}} x_g^{init}$	$k_w : 0 \xrightarrow{\text{spline}} 1$	
III	Hip (H)	(7.36)	(7.39)	–
IV	H-A transition	(7.38)	(7.45)	$x_p, z_g$
V (I')	Ankle	(7.38)	–	–

$$\begin{bmatrix} \dot{\theta}_1 \\ \dot{\theta}_2 \end{bmatrix} = \frac{\dot{x}_g^{ref}}{z_g^2 + (k_m l_g \cos(\theta_1 + \theta_2))^2} \begin{bmatrix} z_g \\ k_m l_g \cos(\theta_1 + \theta_2) \end{bmatrix} + b\mathbf{n}. \quad (7.42)$$

The reference ankle joint rate can then be derived as

$$\dot{\theta}_1^{ref} = \frac{z_g}{z_g^2 + (k_m l_g \cos(\theta_1 + \theta_2))^2} \dot{x}_g^{ref} + k_w \frac{n_1}{n_2} \dot{\theta}_2^{ref}. \quad (7.43)$$

The first component on the r.h.s. depends on the motion rate of the gCoM as a component of the ankle synergy. The second component, on the other hand, is an RNS hip synergy component (cf. (7.36)). The superposition of the two components is realized via a fifth-order spline, i.e.  $0 \leq k_w(t) \leq 1$ . The reference gCoM rate is calculated from the simple feedback law

$$\dot{x}_g^{ref} = k_{pc} (x_g^{des} - x_g), \quad (7.44)$$

$k_{pc}$  denoting a P feedback gain;  $x_g^{des}$  is also determined as a fifth-order spline, to ensure smooth transition between  $x_g^{lim}$  and  $x_g^{init} (= 0)$ , where  $x_g^{lim}$  is the gCoM at the time instant when  $x_p = x_p^{lim}$ , where  $x_p^{lim}$  is a safety limit, set in the vicinity of the BoS boundary.

The H-A transition is initialized after the disturbance disappears. To this end, the values of the ZMP ( $x_p$ ) and the vertical CoM coordinate ( $z_g$ ) are monitored. Note that the desired posture at the end of the transition equals the initial (erect) one ( $\theta_2 = 0$ ). With proper values, the transition will be initialized when  $\theta_2$  is close to zero. Hence, a regulator-type feedback controller can be employed, i.e.

$$\dot{\theta}_2^{ref} = -k_{p\theta}\theta_2, \quad (7.45)$$

$k_{p\theta}$  denoting a feedback gain. At the end, four distinct phases of motion are obtained, as summarized in Table 7.3.

Experimental data obtained with a miniature humanoid robot HOAP-2 [25] (see Section A.1) are shown in Fig. 7.21. The robot is subjected to unknown (variable) continuous disturbance forces applied five times in the horizontal direction, by pushing its back with a hand during a time interval of 60 s. The time span for the A-H transition was set to 1 s,

within the spline functions for the variables  $k_w$  and  $x_g^{des}$ . The ZMP safety limit was set as  $x_p^{lim} = 45$  mm. The H-A transition was initialized when the following condition was met:  $264.5 < z_g < 266.5$  mm and  $x_p < 0$ . The joint angle time history is shown in the bottom-left of Fig. 7.21. Detailed data graphs from the first push are shown on the right side of the figure. The experimental data demonstrate that the ankle/hip synergies with transitions can be realized in a stable manner with a simple velocity-based balance controller on a position-controlled humanoid robot. The experimental results are shown in Video 7.6-1 [94].

It is desirable to extend the controller capabilities in two ways [6]. First, the foot could be allowed to roll. Second, the system parameters should be determined in a rigorous way by taking into account the system state and the stability analysis methods discussed in the previous sections.

The simple double-IP-on-foot model has also been employed in [103] to design an integral controller that accommodates disturbances via the ankle and hip synergies, achieved with an LQR controller and a gCoM regulator, respectively. This is in contrast to the RNS synergy approach where the hip synergy is generated in a simpler way, using the feedforward control only. Another way of generating the hip synergy is by employing a centroidal moment component, as with the RWP model. Motion control during the reaction (or reflex) phase can then be based on spatial dynamics control of the type (5.136). An implementation of this approach with a four-link model (a foot, a two-segment leg with a knee joint, and a torso) is described in [1]. Since the model is planar, the reference momentum rate can be designed with scalar components  $\dot{p}_x^{ref} = k_p(x_p - x_g)$  and  $\dot{l}^{ref} = -k_{\omega}l$ . The optimal quasivelocity, obtained e.g. via the pseudoinverse, can then be inserted into the joint-space inverse dynamics (JSID) solution to derive the joint torque. During the recovery phase, on the other hand, the movements in the three segments can be generated via a potential energy maximization. This approach yields an erected (stretched-leg) upright posture.

#### 7.6.4 Lateral Plane Ankle, Load/Unload and Lift-Leg Synergies

There are relatively few studies that address the implementation of postural balance synergies within the lateral plane with a humanoid robot. In [16], a two-stage balance control strategy was proposed and implemented with a miniature position-controlled robot. The lateral-plane ankle strategy was realized via the ZMP feedback control during the first stage. During the second stage, a combined ankle-hip strategy was applied to deal with the larger disturbances. However, the proposed models did not refer to an in-depth investigation of the human postural balance strategies. In [41], a control approach based on the ZMP/CoM dynamics and the upper-body angular momentum was adopted, resulting in motions wherein the swing foot was used for balance. No particular reaction patterns were envisioned as control input, though, but the robot behavior was found to resemble that of the human participants.

A more detailed study on the implementation of the lateral-plane ankle and load/unload synergies with follow-up transitions to the lift-leg synergy was presented in [126]. The synergies were realized with the help of the simplified multilink models shown in Fig. 7.22.

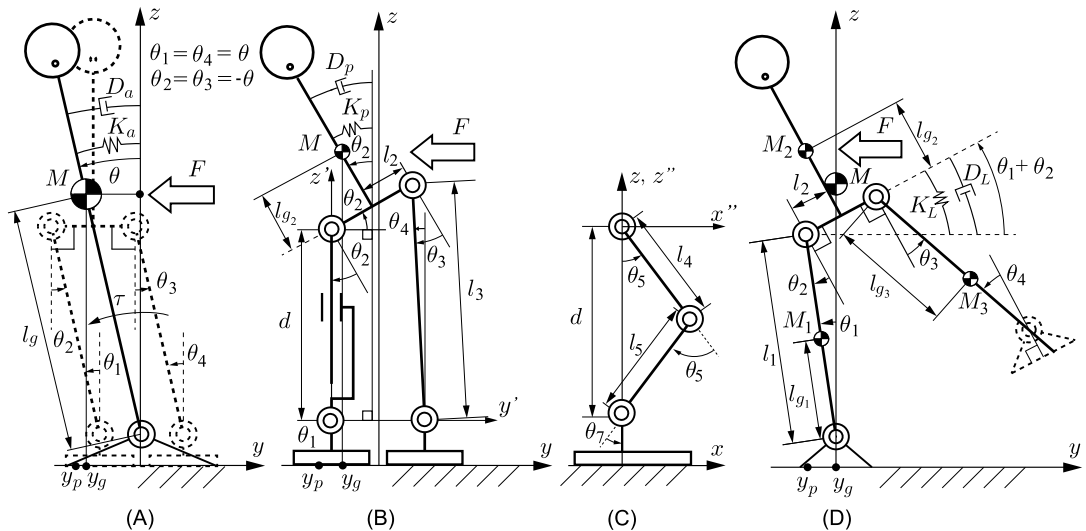


**FIGURE 7.22** Models for the three strategies in the lateral plane. (A) Ankle. (B), (C) Load/unload. (D) Lift-leg. The slider joint in the right leg of (B) is a virtual joint—an equivalent of the real leg subchain involving the three pitch joints: hip ( $\theta_5$ ), knee ( $\theta_6$ ), and ankle ( $\theta_7$ ), as shown in (C).

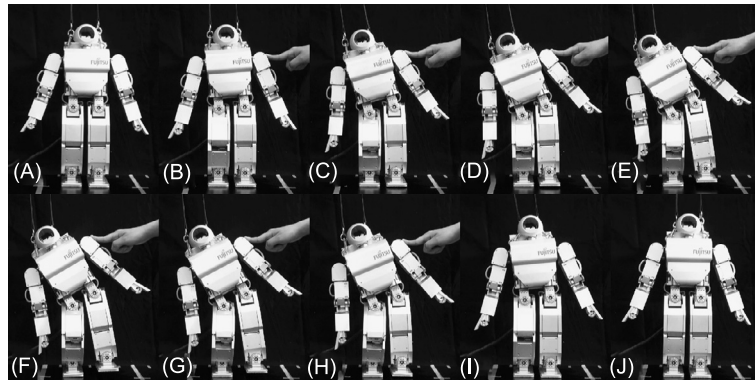


**FIGURE 7.23** Snapshots from Load/Unload and Lift-leg integration, when the disturbance was a continuous force. (A) and (B): Load/Unload strategy. (C)–(H): Lift-leg strategy. (I) and (J): Load/Unload strategy.

Snapshots from the load-unload/lift-leg motion patterns are shown in Fig. 7.23. The ankle/lift-leg synergy motion is shown in Video 7.6-2 [125]. As apparent from the data, the desired motion patterns could be achieved. It should be noted, though, that the implementation was not that straightforward since, first, the models had to be exchanged and, second, the control laws comprised difficult to tune nonlinear spring coefficients and feedback gains. As will be shown in Section 7.7.2, there is an alternative, preferable approach for generating and controlling the lateral-plane reactive synergies with a whole-body model in 3D.

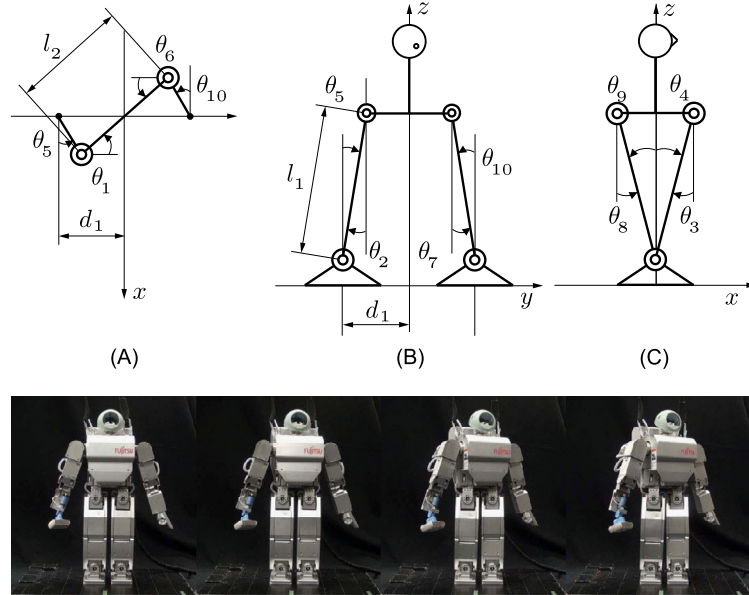


**FIGURE 7.24** Transverse-plane twist strategy. A simple model is used to generate the synergy. (A) Top view. (B) Front view. (C) Side view. The meaning of the joint angles is as follows: hip roll/yaw/pitch:  $\theta_1/\theta_2/\theta_3$  and  $\theta_6/\theta_7/\theta_8$  for right and left, respectively; ankle pitch/yaw:  $\theta_4/\theta_5$  and  $\theta_9/\theta_{10}$  for right and left, respectively.

### 7.6.5 Transverse-Plane Twist Synergy

The transverse-plane twist synergy is used to accommodate a sagittal-plane disturbance force applied from the back (e.g. at the right shoulder), by rotating the upper body around the vertical. Such rotation can be generated via a rolling motion in the pelvis and/or in a special waist-roll joint, if available. The focus here is on the pelvis roll. This synergy can be obtained with the simplified two-leg model shown in Fig. 7.24. The following angular relations can be validated:

$$\begin{aligned}\theta_4 &= \theta_8 = -\theta_9 = -\theta_3, \\ \theta_5 &= \theta_7 = -\theta_{10} = -\theta_2, \\ \theta_6 &= \theta_1.\end{aligned}$$

Here  $\theta_1/\theta_2/\theta_3$  and  $\theta_6/\theta_7/\theta_8$  stand for the roll/yaw/pitch in the right and left hip, respectively;  $\theta_4/\theta_5$  and  $\theta_9/\theta_{10}$  denote the pitch/yaw in the right and left ankle, respectively. Furthermore, from Fig. 7.24B and C one obtains

$$\begin{aligned}l_2 \sin \theta_5 + d_1 \cos \theta_1 &= d_1, \\ l_2 \sin \theta_4 + d_2 \sin \theta_1 &= 0,\end{aligned}$$

respectively. Thus,

$$\theta_2 = \arcsin \left( \frac{d_1 - d_1 \cos \theta_1}{l_1} \right),$$

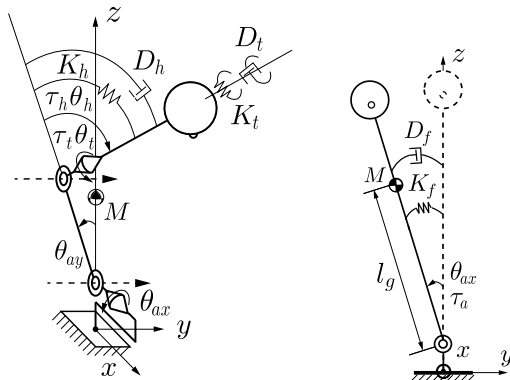


**FIGURE 7.25** Simple models for an ankle-hip-twist strategy superposition. Left (A): four-joint 3D model for the hip-twist and lateral-ankle synergies. Right (B): a single-joint planar model for the lateral-ankle synergy. The virtual spring/damper variables are denoted as  $K_{(o)}/D_{(o)}$ , respectively.

$$\theta_3 = -\arcsin\left(\frac{d_1}{l_1} \sin\theta_1\right).$$

Apparently, all angles can be expressed as functions of  $\theta_1$ . This angle parametrizes the twist synergy. Snapshots from the realization of the twist strategy are shown in the lower part of Fig. 7.24.

### 7.6.6 Complex Reactive Synergies Obtained by Superposition of Simple Ones

The ultimate goal in synergy-based balance control is the design of a controller that can ensure responses to a variety of disturbances applied from different directions. This implies that the appropriate reaction/recovery synergy has to be invoked depending on the magnitude and direction of the disturbance. Two approaches will be introduced below. First, in the remainder of this subsection, the superposition of the simple in-plane synergies discussed so far will be explored. The goal is to obtain a set of out-of-plane synergies that can handle disturbances from various directions. The second approach, to be introduced in Section 7.7, is based on synergy generation with whole-body models.

The sagittal-plane ankle/hip, lateral-plane ankle, and transverse-plane twist synergies can be combined with the help of the simple model shown in Fig. 7.25A. The model comprises two 2-DoF joints: a pitch-yaw ankle joint and a pitch-roll hip joint. A separate model for ankle-yaw is shown in Fig. 7.25B. This model is used in the lateral-plane ankle synergy. Virtual spring/dampers are attached to the joints, with the exception of the ankle-pitch joint. This joint is the dependent joint in the hip synergy. The hip-roll joint is used in the twist synergy that was explained in Section 7.6.5;  $\tau_a$ ,  $\tau_h$ , and  $\tau_t$  are derived from the external disturbances for yaw, pitch, and roll measured by a force/torque sensor embedded into the pelvis of the experimental robot.<sup>4</sup> These inputs are inserted into the forward dynamic relations of the two

<sup>4</sup> A HOAP-2 robot was modified to accommodate the force/torque sensor.

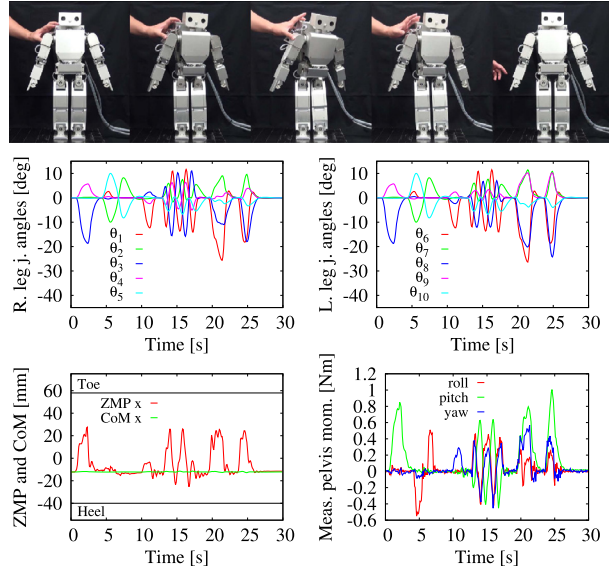


**FIGURE 7.26** Superposition of the ankle-hip-twist synergies. The moment graphs in the bottom-right plot present data obtained from a force/torque sensor embedded into the pelvis of a HOAP-2 robot. The leg joint angles are numbered in increasing order from the hip toward the ankle. The knee joint is not included into the model.

simple models, to obtain the joint accelerations, and the velocities and positions after integration. These are then mapped to the joints of the real robot. As apparent from Video 7.6-3 [93] and the graphs in Fig. 7.26, the robot responds swiftly to perturbations from various directions, resulting in a very compliant behavior. Note that the hip synergy is realized via the RNS approach, as described in Section 7.6.3. In this way, the ZMP excursion within the sagittal plane can be minimized.

The lateral-plane ankle synergy is the only lateral plane synergy realized in this experiment. It could be possible to implement the lateral-plane load/unload and lift-leg synergies, but as already noted, the handling of the transitions between numerous models and the respective synergies is not that straightforward. It would be much more preferable to generate the complex reactive motion patterns with a single whole-body model. Such approach will be introduced in Section 7.7.

### 7.6.7 Summary and Discussion

Simple models can be employed to obtain reactive synergies for accommodating unknown external disturbances of *medium magnitude* that do not require a change in the BoS. The synergies are derived from those used by humans to maintain their balance. It is possible to superimpose the in-plane synergies to obtain fairly complex whole-body motion patterns in response to disturbances acting from various directions. Implementations with a position-controlled humanoid robot have demonstrated satisfactory results, including transitions between the synergies. However, the tuning of the parameters for the transitions is

not straightforward. An alternative and more straightforward approach for generating complex out-of-plane reactive synergies with a single whole-body model will be introduced in Section 7.7.

## 7.7 REACTIVE SYNERGIES OBTAINED WITH A WHOLE-BODY MODEL

---

Reactive synergies that can cope with various types of external disturbances of medium magnitude can be generated with the whole-body models described in this work. To obtain a compliant response during the reflex phase, relatively low feedback gains for the CRB trajectories are used. After the disturbance disappears, the feedback gains are switched to higher values to ensure the swift recovery of the initial posture. This approach is known as *gain scheduling* (see e.g. [73,58]). Alternatively, the initial posture can be recovered with CRB trajectory tracking, as described in Section 5.8.7.

In this section, four balance control approaches will be explored, based on:

- a simple dynamic torque controller;
- a DCM-GI-based wrench distribution implementation for the load/unload and lift-leg strategies;
- a compliant-body response;
- an impact accommodation via angular momentum damping from the RNS (cf. Section 5.11.2);
- a reactive change-of-BoS (reactive stepping).

It is important to distinguish between continuous and impulsive types of disturbances. The discussion in Section 7.6 was based on the former type exclusively. In this section, it will be shown how to implement the balance control methods for both types of disturbances.

All simulations in this section were performed with a small-size humanoid robot model with parameters similar to those of the HOAP-2 robot [25] in the Choroneoid environment [87]. For the numbering of the robot joints and other relevant data, see Section A.1.

### 7.7.1 Reactive Synergies Generated With a Simple Dynamic Torque Controller

A whole-body reactive motion in 3D can be generated and controlled with the simple control law (5.128). Thereby, the linear component of the reference rate of change of the spatial momentum will be obtained from the DCM stabilizer (cf. (5.76)), while the angular one comprises just a damping term. The controller block diagram is the same as that shown in Fig. 5.25. The only difference is the setting of the desired values.

During the reactive (reflex) phase ( $T_0 \leq t < T_{rec}$ ), admittance motion control will be employed. This can be done in a straightforward manner by setting the desired DCM at the current CoM position ( $\dot{\mathbf{r}}_X^{des}(t) = \dot{\mathbf{r}}_C(t)$ ) in the DCM stabilizer. The reference DCM can then be obtained from (5.76) and the definition of the DCM as

$$\dot{\mathbf{r}}_X^{ref}(t) = (1 - T_X k_X) \dot{\mathbf{r}}_C(t), \quad (7.46)$$

where  $T_X = 1/\bar{\omega}_X$  is the time constant of the DCM dynamics.

When the external disturbance disappears (at  $T_{rec}$ ), the recovery phase is initialized. During this phase, the desired DCM trajectory is determined as

$$\mathbf{r}_X^{des}(t) = \mathbf{r}_C(t) + (1 - e^{-\frac{t-T_{rec}}{T_X}})(\mathbf{r}_X^s(t) - \mathbf{r}_C(t)). \quad (7.47)$$

Here  $\mathbf{r}_X^s(t)$ ,  $T_{rec} \leq t \leq T_f$ , is obtained via a fifth-order spline with the nonstationary initial state  $\mathbf{r}_X^s(T_{rec})$  and the stationary final state  $\mathbf{r}_C(T_f) = \mathbf{r}_C^{init}$ ,  $\dot{\mathbf{r}}_C(T_f) = \mathbf{0}$ ,  $\mathbf{r}_C^{init}$  denoting the initial CoM position (before the appearance of the disturbance);  $\mathbf{r}_X^{des}(t)$  and its time derivative are substituted into (5.76) to obtain  $\dot{\mathbf{r}}_X^{ref}$  for the recovery phase. Note that in this way, a smooth transition from the reflex to the recovery phase will also be ensured.

As an example, consider the case when an “unknown” external pushing force is applied on the back of a standing upright humanoid robot horizontally within the sagittal plane. The magnitude of the disturbance is gradually increased from zero to the maximum of 6 Nm via a fifth-order spline, within  $2 \sim 4$  s. The magnitude stays constant within  $4 \sim 12$  s and then decreases gradually within  $12 \sim 14$  s. The application point is at  $(0, -0.050, 0.145)$  m w.r.t. the base coordinate frame, i.e. close to the right shoulder. This implies that the robot has to react with a combination of the hip and twist synergies. There are no particular models for the synergies, though. The reflex movement patterns are obtained by just setting the feedback gains to mimic the virtual spring/dampers. The simulation result is shown in Video 7.7-1 [50]. Apparently, the robot reacts as desired, in a compliant way and without loosing balance. After the disturbance disappears, a swift recovery movement is performed, also in a stable way. The stable performance during the two phases can be confirmed from the graphs in Fig. 7.27.

Furthermore, when the magnitude of the disturbance is set initially at a smaller value, the sagittal-plane ankle synergy will be invoked first. An increase in the magnitude of the disturbance during the ankle strategy yields a smooth transition to the hip-twist synergy. The results from the simulation can be seen in Video 7.7-2 [49].

### 7.7.2 The Load/Unload and Lift-Leg Strategies Revisited

The lateral plane lift-leg synergy described in Section 7.6.4 can be realized with a whole-body dynamic model under the DCM generalized inverse distribution control approach described in Section 5.10.4. The control method is examined via a simulation with the model and controller parameters set as in the examples described in Section 5.10.4. The reactive balance control task demonstrates the performance in the presence of an “unknown” disturbance force impulse, specified by a force vector of  $(0, -20, -20)$  N, applied from between  $3 \sim 5$  s at the left hip of the robot. Accommodation of this disturbance requires a variation in the CoM height. Note that the DCM control approach admits such variations. The  $\bar{z}_{vvp}$  constant in the DCM controller (cf. Section 5.6.2) is set at the initial CoM height (242 mm), which yields  $\bar{\omega}_X = 0.169$ . The force impulse results first in the loading/unloading of the right/left foot, then in lifting the left leg. Thus, this task demonstrates transitions from double to single and back to double stance (DS→SS→DS).

Video 7.7-3 [43] presents the result in animated form; the graphs are displayed in Fig. 7.28. The gray/pink areas in Fig. 7.28 signify the load/unload (DS) and lift-leg (SS) strategy, respectively. The left/right column displays the results from a simulation whereby the dynamic stability area has been set as large/small, respectively. From Fig. 7.28A and B it is seen that

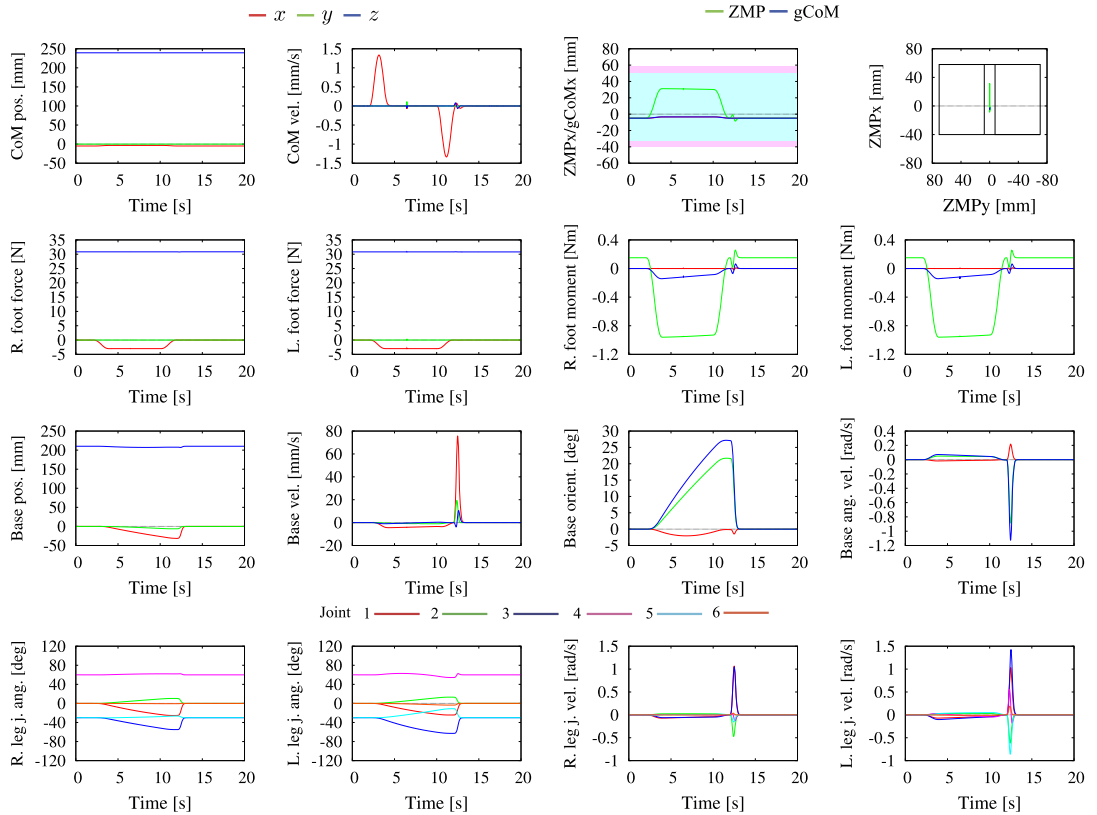


**FIGURE 7.27** Simulation data for the hip-twist reflex synergy followed by a fast recovery motion. The magnitude of the disturbance is gradually increased within  $2 \sim 4$  s, stays constant at 6 Nm within  $4 \sim 12$  s, and then decreases gradually within  $12 \sim 14$  s. The robot recovers thereafter its initial posture, swiftly and in a stable way.

the disturbance component in the  $z$ -direction yields a significant variation in the vertical CoM position. The reaction forces in Fig. 7.28C–F demonstrate the continuous asymmetric force distribution capability of the DCM-GI. The CoP graphs are shown in Fig. 7.28G and H. From the results it is apparent that enlarging the dynamic stability area beyond the ankle-joint positions is possible. However, as seen from Fig. 7.28G, the left foot CoP (green line) almost reaches the limit of the BoS. The foot roll can be avoided, though, since the robot switches from DS to SS in a stable manner. The joint velocity graphs for the four limbs are shown in Fig. 7.28I–L. They demonstrate that the transitions are performed in a continuous way, without excessive accelerations.

### 7.7.3 Compliant-Body Response

A compliant body-type of behavior in response to arbitrary external wrenches was demonstrated in Section 7.6.6. The motion was obtained from the superposition of synergies derived

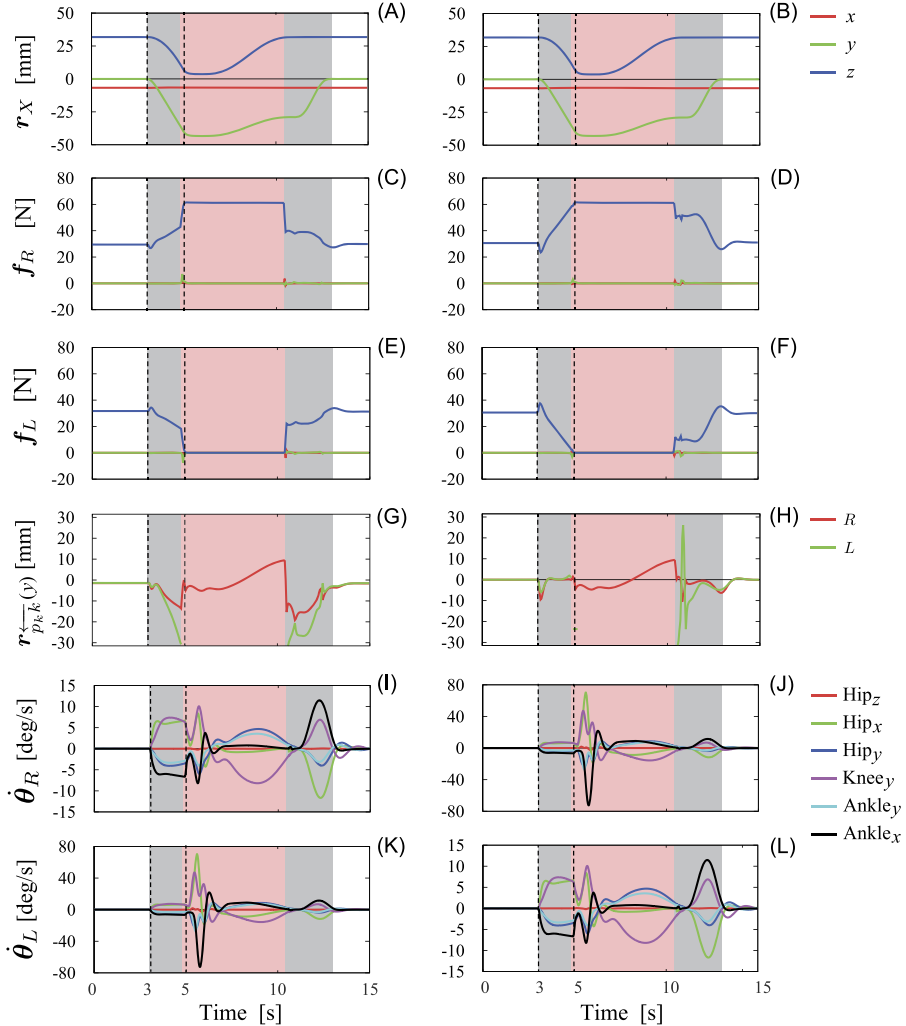


**FIGURE 7.28** Reactive task under an unknown disturbance acting at the base/hip. The graphs on the l.h.s./r.h.s. display the results from a simulation where by the dynamic stability area has been set as large/small, respectively. The gray/pink areas signify the load/unload and the lift-leg strategies, respectively. The time span of the disturbance is signified with dotted vertical lines.

from multiple simple models. In this section, it will be shown that the same type of response can be obtained with a CRB trajectory tracking controller based on the constraint-consistent joint acceleration (5.141), i.e.

$$\ddot{\boldsymbol{\theta}} = \mathcal{J}_{cM}^+ \left( (\dot{\bar{\mathcal{V}}}^c) - \mathbb{C}_{cC}^T \dot{\mathcal{V}}_M^{ref} - \dot{\mathcal{J}}_{cM} \dot{\boldsymbol{\theta}} - \dot{\mathbb{C}}_{cC}^T \mathcal{V}_M \right) + N(\mathcal{J}_{cM}) \ddot{\boldsymbol{\theta}}_u. \quad (7.48)$$

The acceleration in the constrained motion directions,  $\dot{\mathcal{V}}^c$ , is set at zero since the robot stands on firm ground. The control input for the CRB trajectory tracking is defined in accordance with the results in Section 5.8.7 as

$$\dot{\mathcal{V}}_M^{ref} = \mathbb{M}_C^{-1} \mathcal{F}_B^{ext} + \begin{bmatrix} K_{vc} \dot{\mathbf{e}}_{pc} \\ K_{\omega_B} \mathbf{e}_{\omega_B} \\ K_{ob} \mathbf{e}_{ob} \end{bmatrix} + \begin{bmatrix} K_{pc} \mathbf{e}_{pc} \\ K_{ob} \mathbf{e}_{ob} \end{bmatrix}. \quad (7.49)$$

The feedback gains  $K_{(o)}$  and the errors  $\mathbf{e}_{(o)}$  are defined in Section 5.8.7;  $\mathcal{F}_B^{ext}$  is the external wrench measured by the force/torque sensor mounted at the pelvis (cf. Section 7.6.6). This wrench is mapped by the inverse of the CRB (locked) inertia to obtain a feedforward control component in terms of CRB acceleration. The control input  $\ddot{\theta}_u$  determines the motion of the arms. In the following experiment, the arms will be kept motionless.

The experiment was the same as that described in Section 7.6.6: arbitrary wrenches were generated by slightly pushing the upper body in various directions. Since the force/moment measurements were noisy, a threshold of 1 N/Nm was used to filter out the noise. Note that a low-pass filter should be avoided due to the time delay; the robot's response would not be sufficiently compliant. The P and D feedback gains for the CRB trajectory tracking were set at 300 and 100, respectively, for each, position and orientation. The control time interval was 2.5 ms. The result is shown in Video 7.7-4 [51]. The graphs for the measured force/moment, the displacement errors for the CoM and the base rotation, and the joint angles in the legs are displayed in Fig. 7.29.

#### 7.7.4 Impact Accommodation With Angular Momentum Damping From the RNS

In general, an impact can be accommodated either with the linear or the angular component of the spatial momentum, or with both. When the xCoM is located in the vicinity of the BoS boundary, even a weak impact could invoke a critical postural state leading to a foot roll (State D in Fig. 5.3). As clarified in Section 5.3.3, a swift action would then be required to restore the balance. Note that at a critical state, it would be impossible to accommodate the impact via the CoM motion alone; either an angular momentum-based accommodation should be invoked or a reactive step taken. Below, the focus is on the angular momentum-based accommodation with trunk and arm rotations. A reactive step-type response will be discussed in Section 7.7.5.

In Section 5.8.3 it was shown that the *relative angular momentum/velocity* (RAM/V) balance controller can be used to achieve fast proactive torso rotations without deteriorating the balance. The movements of the arms, though not under direct control, have been shown to play an important role. The method can be adopted in a straightforward manner to generate and control a whole-body reflexive motion of a humanoid robot subjected to an impact. To accommodate the impact, angular momentum damping will be injected into the system. This can be done with the *relative angular acceleration* (RAA) controller derived from the second-order formulation of the method (cf. Section 5.11.2).

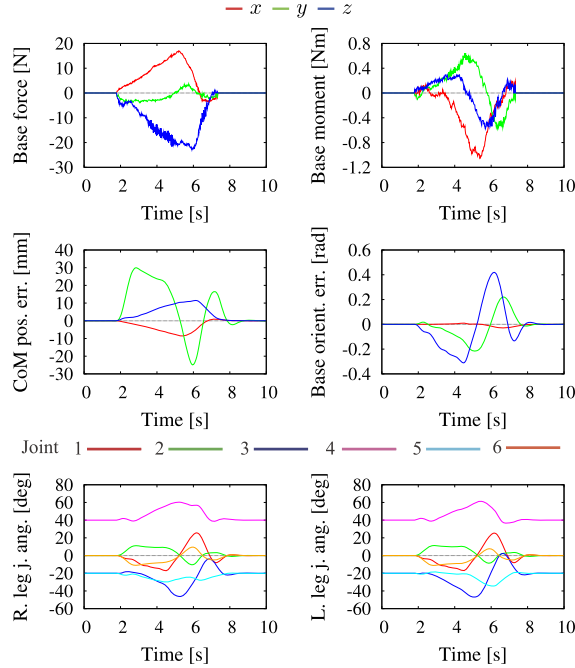


**FIGURE 7.29** Compliant-body response experiment. The measured base force/moment is used as a feedforward control input for the CRB acceleration. The errors denote deviations from the initial configuration.

The constraint-consistent joint acceleration given in (5.142) comprises three *independent* control inputs: the inertia CoM acceleration,  $\dot{\mathbf{v}}_{C_I}^{ref}$ , the system angular acceleration,  $\dot{\boldsymbol{\omega}}_C^{ref}$ , and the angular acceleration of the base link,  $\dot{\boldsymbol{\omega}}_B^{ref}$ . Recall that when the mixed quasivelocity is employed, the CoM acceleration component will be completely decoupled from the angular acceleration one. This implies that  $\dot{\mathbf{v}}_{C_I}^{ref}$  can be designed independently from the two reference angular accelerations.

The conservation of either the system or the coupling angular momentum has been pointed out (in Section 5.11.2) as a possible goal in the design of the angular accelerations. Note, however, that in the case of an impact at a critical state, the system angular momentum conservation would be of no help to reverse the motion in the rolling foot or feet. The only possibility to stabilize the robot at such a state is to *invoke a coupling angular momentum conservation*. This implies an RNS-based design for the angular accelerations, s.t. (cf. Section 5.11.2)

$$\dot{\boldsymbol{\omega}}_C^{ref} = \dot{\boldsymbol{\omega}}_B^{ref} - D_{\boldsymbol{\omega}} \mathbf{J}_{\boldsymbol{\omega}} \dot{\boldsymbol{\theta}}. \quad (7.50)$$

The capability of the RNS-based postural stabilization at a critical state (a foot roll) invoked by an impact will be demonstrated with the following simulation. The humanoid robot is placed on a flat ground in a symmetric posture, the feet being aligned. The robot is leaning forward s.t. the gCoM is in the vicinity of the BoS boundary (the toe area). The initial posture is stabilized with the asymptotic trajectory tracking control approach, using

**TABLE 7.4** Gain scheduling for the base-link rotation PD feedback gains (impact expected)

Phase	Preimpact	Impact	Postimpact I	Postimpact II
Time (s)	0 ~ 0.9	0.9 ~ 1.0	1.0 ~ 1.05	1.05 ~ 1.25
$K_{o_B}$ (P-gain)	300	300 ~ 0.01	0.01	0.01 ~ 30
$K_{\omega_B}$ (D-gain)	50	50 ~ 0.001	0.001	0.001 ~ 5

the RAA controller given in (5.142). The CoM motion is regulated toward the initial position. The respective PD feedback gains are set at relatively high values ( $K_{pC} = 300$ ,  $K_{vC} = 50$ ). The damping gain, used in (7.50) to ensure the RNS-based motion generation, is set at  $D_\omega = 100$ .

The disturbance accommodation during the impact phase and the stabilization of the posture during the postimpact phase are done with a prevailing upper body rotation (in the trunk and the arms), as already explained. The disturbance is applied within the sagittal plane, in the horizontal direction from behind. The application point is around the neck, the exact coordinates (in the base-link frame) are (0, 0, 145) (mm). The impulse of the disturbance is of magnitude 5.5 N, applied for 50 ms. Since the disturbance direction has no lateral component, it can be expected that the impulse will be accommodated with a base-link rotation in the pitch direction mainly. In general,  $\dot{\omega}_B^{ref}$  could be designed as a conventional feedforward plus PD feedback control law. In the special case of a disturbance accommodation task, though, there is no need for a feedforward term. Only PD feedback control can be used to ensure the compliant behavior at impact and the fast recovery after the impact. It will be sufficient to regulate the base-link angular deviation toward the initial posture during all three phases (i.e. preimpact, impact, and postimpact).

### ***Anticipatory-Type Impact Accommodation***

To accommodate the disturbance during the reflex (impact) phase and to stabilize the posture in the postimpact phase, a gain scheduling approach is employed (see e.g. [73,58]). The set of the PD gains for the base rotation is given in Table 7.4. Initially, high gains are used to ensure the desired base orientation (i.e. the initial orientation). Just before the impact, the gains are lowered significantly. After the impact, the gains are switched to higher values to ensure swift recovery. Note that the lowering of the gains *before* the impact corresponds to an *anticipatory* type of behavior.

The results of the simulation are shown in an animated form in Video 7.7-5 [36] and in graphic form in Fig. 7.30. From the graphs it is seen that the impact was successfully accommodated, mainly with a base angular deviation in the pitch direction, as expected. The displacement of the CoM was insignificant. During the accommodation period, the net CoP arrived at the BoS boundary. From the foot angular velocity graphs it is seen that the feet were about to roll. The robot was able to avoid this critical state, however, since the RNS joint acceleration component generated an appropriate swift arm motion. After that, the posture was stabilized to the initial one.

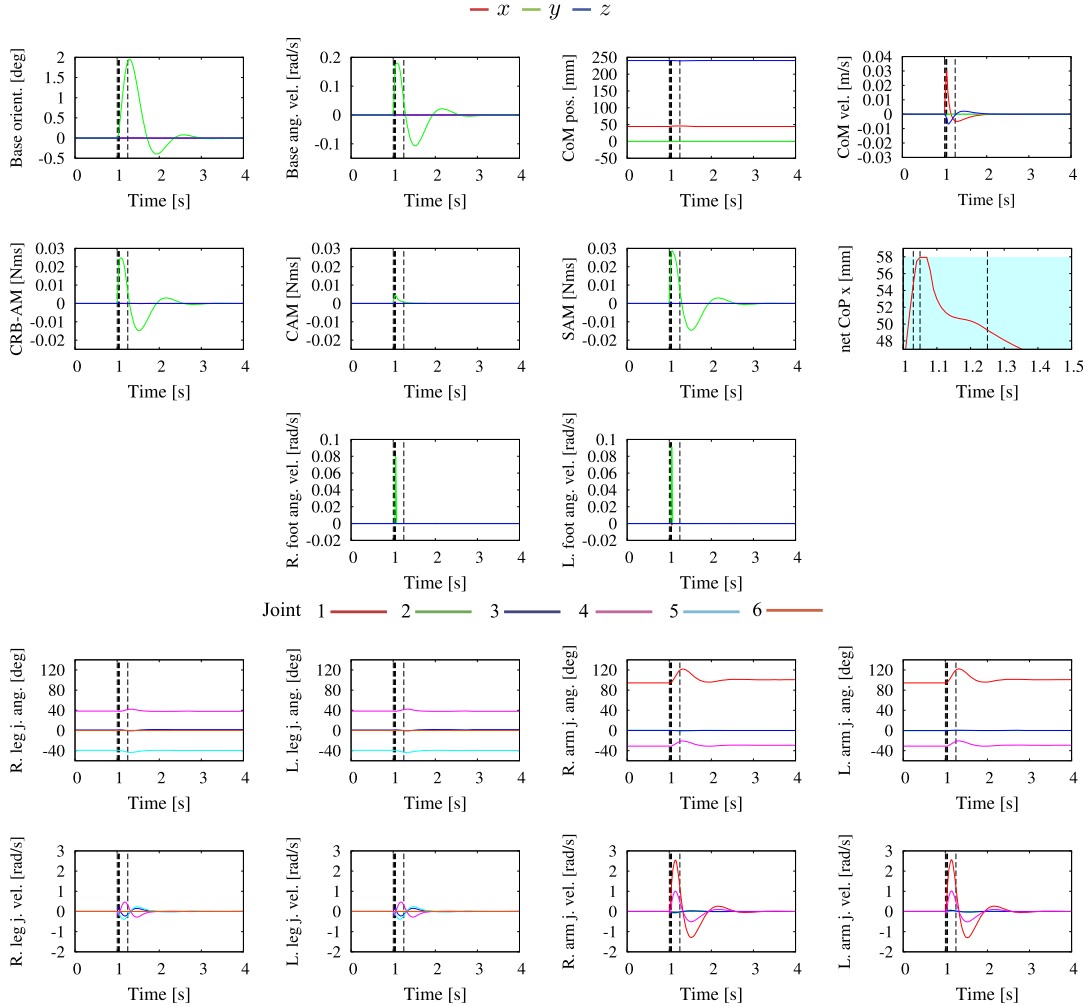


FIGURE 7.30 Simulation result for reflexive impulse accommodation with anticipatory type of behavior (the PD feedback gains for base rotation are lowered *before* the impact). A foot roll is successfully suppressed via the arm motion generated with the RNS approach. The vertical dashed lines signify the time instants in Table 7.4.

### Nonanticipatory-Type Impact Accommodation

The same simulation was repeated with a gain scheduling policy corresponding to a *nonanticipatory* type of behavior. The set of the PD feedback gains for the base rotation is given in Table 7.5. Note that the initial high gains are maintained during the first 20 ms after the impact onset (i.e. Impact I phase). The gains are then lowered to obtain a compliant response during the remaining 30 ms of the impact (i.e. Impact II phase) and the Postimpact I phase. In the final phase, Postimpact II, the gains are switched again to higher values to ensure swift recovery of the initial posture.

TABLE 7.5 Gain scheduling for the base-link rotation PD feedback gains (impact unexpected).

Phase	Preimpact	Impact I	Impact II	Postimpact I	Postimpact II
Time (s)	0 ~ 1.0	1.0 ~ 1.03	1.03 ~ 1.05	1.05 ~ 1.25	1.25 ~
$K_{o_B}$ (P-gain)		300	300 ~ 0.01	0.01 ~ 30	30
$K_{\omega_B}$ (D-gain)		50	50 ~ 0.001	0.001 ~ 5	5

The results of the simulation are shown in animated form in Video 7.7-6 [37] and in graphic form in Fig. 7.31. The main difference with the previous experiment is that a foot roll could not be avoided. Both feet started rolling since the gains were high at impact onset, and the base link could not accommodate the impact with pitch roll as much as in the previous simulation. Nevertheless, the RNS-based generated motion response in the arms was able to ensure the recovery of the plane contacts at the feet and that of the posture stability. Note that no provision was made in the controller for the contact transitions at the feet. This clearly demonstrates the robustness of the controller w.r.t. the model discrepancies.

### 7.7.5 Reactive Stepping

The so-called *change-of-BoS* strategy is used by humans in response to unexpected postural perturbations with a relatively large magnitude. The most prominent example is the reactive stepping (or stumbling) [102,75,76]. Other examples include strategies performed mainly in the lateral plane, known as the “loaded side step” and the “unloaded crossover step” [96], as well as strategies that involve hand support, the so-called “reach-and-grasp” strategies [76]. In this section, the focus will be on the reactive stepping.

From the field of biomechanics it is known that when a relatively large disturbance is applied to the human body, one or more steps may be needed to restore the balance with an upright standing posture [2]. The decision on the number of steps to be taken can be based on the outcome of the so-called “N-step capturability” analysis [67]. The analysis uses the CP theory applied to the 3D LIP, the 3D LIP-on-foot, and the 3D RWP models described in Sections 4.4.2 and 4.4.3. The state at which the balance can eventually be restored after taking one or more steps is referred to as the *captured state*. Being a generalization of the CP approach, the N-step capturability framework is suitable for motion generation and balance control that can endow a humanoid robot with the ability to arrive at a captured state without falling, by taking N or fewer steps [99].

In what follows, an implementation of the N-step capturability framework for balance control during reactive stepping will be described. The following assumptions are made for clarity and simplicity:

- The reactive stepping strategy is implemented on a flat ground.
- The initial state is stationary, the feet being aligned.
- Multiple steps can be taken, each step is completed in time  $T_{step}$ .
- The DCM trajectory is in the horizontal plane (the LIP model applies).
- The swing leg path is a circular arc with maximum height  $l_h$ .

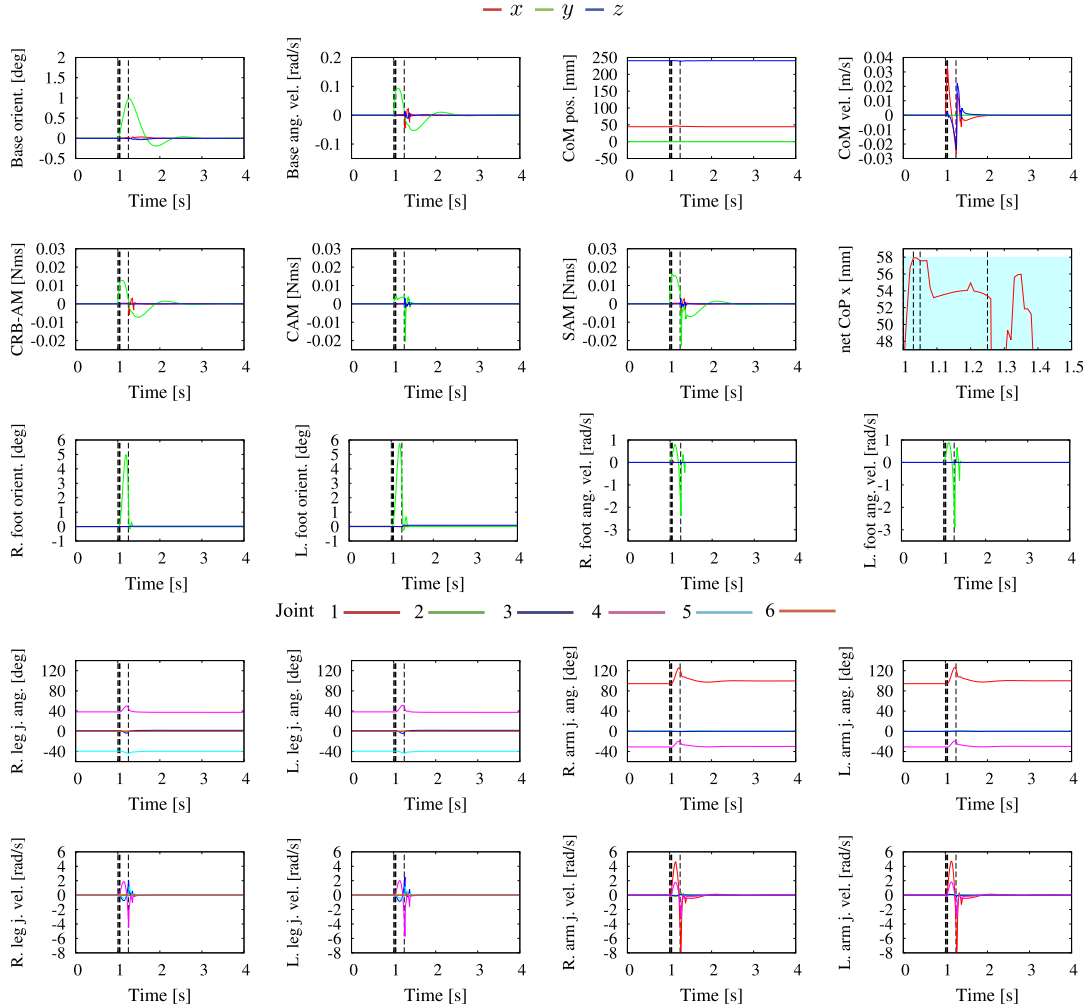


**FIGURE 7.31** Simulation result for reflexive impulse accommodation with nonanticipatory type of behavior with high-gain impact. A foot roll is unavoidable but the plane contacts at the feet and the stability can be recovered via the arm motion generated with the RNS approach. The vertical dashed lines signify the time instants in Table 7.5.

The disturbance is in the form of an impulse expressed as the force/time product  $f_{ext}\Delta t_{imp}$ ,  $\Delta t_{imp}$  denoting the time duration of the impulse. The disturbance induces a change in momentum, i.e.  $M\Delta v_C = f_{ext}\Delta t_{imp}$ . Apparently, the change in the CoM velocity is determined by the direction and magnitude of the applied force. The xCoM/ICP trajectory  $r_{ex}(t)$  may leave the BoS (e.g. as shown with  $r_{ex}(t_{imp}^{end})$  in Fig. 7.32A), resulting in a foot roll and eventually in a fall. One possibility to alleviate this problem is to make use of the centroidal moment, as clarified in Chapter 5. The linear reaction-wheel pendulum model (LRWP) described in Section 5.6.1 can be employed. The 2D version of the xCoM dynamics (5.61) is

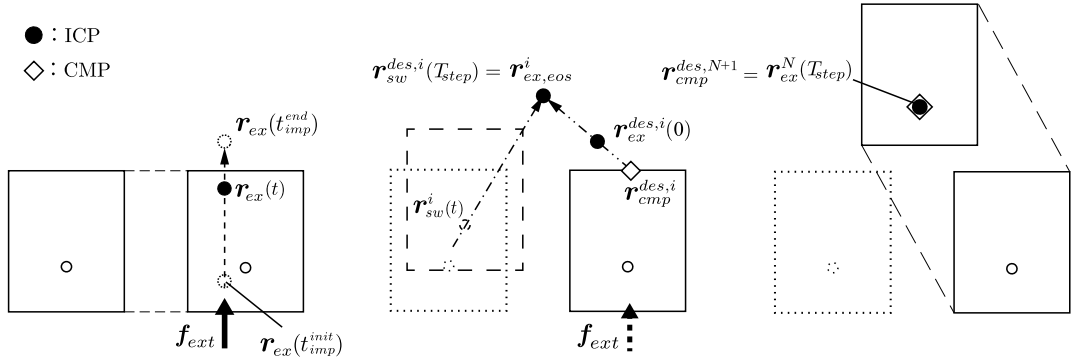


FIGURE 7.32 Reactive stepping. Left (A): Impact phase. Middle (B): Stepping phase. Right (C): Recovery phase.

written as

$$\dot{\mathbf{r}}_{ex}(t) = \omega(\mathbf{r}_{ex}(t) - \mathbf{r}_{cmp}(t)). \quad (7.51)$$

Recall that  $\omega$  is the natural angular frequency of the LIP dynamics. The above equation can also be obtained by projecting the DCM dynamics (5.72) onto the ground surface. The solution is given as

$$\mathbf{r}_{ex}(t) = e^{\omega t} (\mathbf{r}_{ex}(0) - \mathbf{r}_{cmp}(t)) + \mathbf{r}_{cmp}(t). \quad (7.52)$$

As already noted,  $\mathbf{r}_{ex}(t)$  is also referred to as the *instantaneous CP* (ICP) [67].

Another possibility to avoid a foot roll is to initialize reactive stepping. The xCoM location after the impact,  $\mathbf{r}_{ex}(t_{imp}^{end})$ , is used to assess the capturability, i.e. whether zero, one, or more steps will be needed to arrive at a desired captured state  $\mathbf{r}_{ex}^{des}$ . In the case of a nonzero step capturability, as assumed here,  $\mathbf{r}_{ex}^{des,i}(0) = \mathbf{r}_{ex}(t_{imp}^{end})$  is located outside the BoS (cf. Fig. 7.32B).

The reactive stepping algorithm comprises four phases: preimpact, impact, stepping, and recovery. The desired DCM/ICP trajectories are generated with the help of (7.51) and (7.52) as follows.

### Impact Phase

The impact phase duration is  $\Delta t_{imp} = t_{imp}^{end} - t_{imp}^{init}$ . During this time interval, the impact is accommodated with an appropriate CoM translation and a base rotation. The xCoM trajectory is designed to yield an admittance type of behavior, i.e.

$$\dot{\mathbf{r}}_{ex}^{des}(t) = \dot{\mathbf{r}}_g(t), \quad \mathbf{r}_{ex}^{des}(t) = \mathbf{r}_g(t), \quad (7.53)$$

where  $t_{imp}^{init} \leq t \leq t_{imp}^{end}$ . A rotary damper is used for the base-link rotation, the respective PD gains being designed with the help of a gain scheduling approach. The ICP trajectory is depicted in Fig. 7.32A.

### Stepping Phase

In general,  $N$  reactive steps are assumed. The stepping is initialized at the end of the impact,  $t_{imp}^{end}$ . For each step, relative time is used, s.t.  $0 \leq t \leq T_{step}$ . Since the foot roll problem is tackled with reactive stepping, a zero centroidal moment is admissible. In this case, a constant CMP can be employed. The desired ICP trajectory for Step  $i$  is obtained from (7.51) and (7.52) as

$$\mathbf{r}_{ex}^{des, i}(t) = e^{\omega t} \left( \mathbf{r}_{ex}^i(0) - \mathbf{r}_{cmp}^{des, i} \right) + \mathbf{r}_{cmp}^{des, i}, \quad (7.54)$$

$$\dot{\mathbf{r}}_{ex}^{des, i}(t) = \omega \left( \mathbf{r}_{ex}^{des, i}(t) - \mathbf{r}_{cmp}^{des, i} \right), \quad (7.55)$$

respectively. Here CMP  $\mathbf{r}_{cmp}^{des, i}$  denotes the constant desired CMP. Its location is set at the BoS boundary, at the crossing point with the line determined by  $\mathbf{r}_{ex}^{des, i}(0)$  and the desired CP at the end of the step,  $\mathbf{r}_{ex,eos}^i$ . The latter should be set in a way that minimizes the step length. This situation is depicted in Fig. 7.32B;  $\mathbf{r}_{sw}(t)$  is the ground projection of the swing leg path.

### Recovery Phase

After completing the  $N$  steps, at  $t = T_{rec}$  the ICP is within the BoS. The robot state is captured with

$$\mathbf{r}_{ex}(T_{rec}) = \mathbf{r}_{ex}^N(T_{step}) = \mathbf{r}_{cmp}^{des, N+1}. \quad (7.56)$$

This situation is depicted in Fig. 7.32C. Note that motion in the upper body (trunk and arms) is admissible, when generated from within the null space of the xCoM stabilization task.

The walking controller shown in Fig. 7.14 will be used. The reference contact wrenches are determined via the VRP-GI (cf. Section 5.10.5). The linear component of the reference rate of change of the spatial momentum is obtained from the DCM stabilizer (cf. (5.76)). The angular component (i.e. the rotation of the trunk/base link) is specified as a regulator with a damping term (obtained from (5.106) by removing the feedforward term). The motion of the arms is determined by a joint damping.

### Simulation

The results from a simulation of reactive stepping under the above control approach are shown in Video 7.7-7 [52]. The impact force  $\mathbf{f}_{ext} = (30, 0)$  N was applied at  $t_{imp}^{init} = 1.0$  s for  $\Delta t_{imp} = 0.1$  s. This resulted in  $\mathbf{r}_{ex}(0) = (70.8, -25.2)$  mm and  $N = 1$ . The stepping time duration was preset at  $T_{step} = 0.2$  s. The CP was calculated as  $\mathbf{r}_{ex}^{des, N} = \mathbf{r}_{ex}^{des}(T_{rec}) = (124.9, 0.0)$  mm, where  $T_{rec} = t_{imp}^{end} + T_{step} = 1.1 + 0.2 = 1.3$  s. Feedback was used only during the initial (preimpact) and final stabilization. During the impact and the stepping, only feedforward was applied. This implies an anticipatory type of behavior. The joint damping gain for the arm motion was set at  $K_{D_h} = 100$ . The stability margins for the VRP-GI-based wrench distribution at the initial and final DS postures were set to pass under the ankles. The maximum step height was set at 10 mm.

The data graphs for the mixed quasicoordinate and quasivelocity, the states of the end links, the GRFs and GRMs at the feet, the DCM error, the gCoM, the net CoP, and the xCoM are shown in Fig. 7.33. The CoP coordinates are presented in the local frames, the light-blue

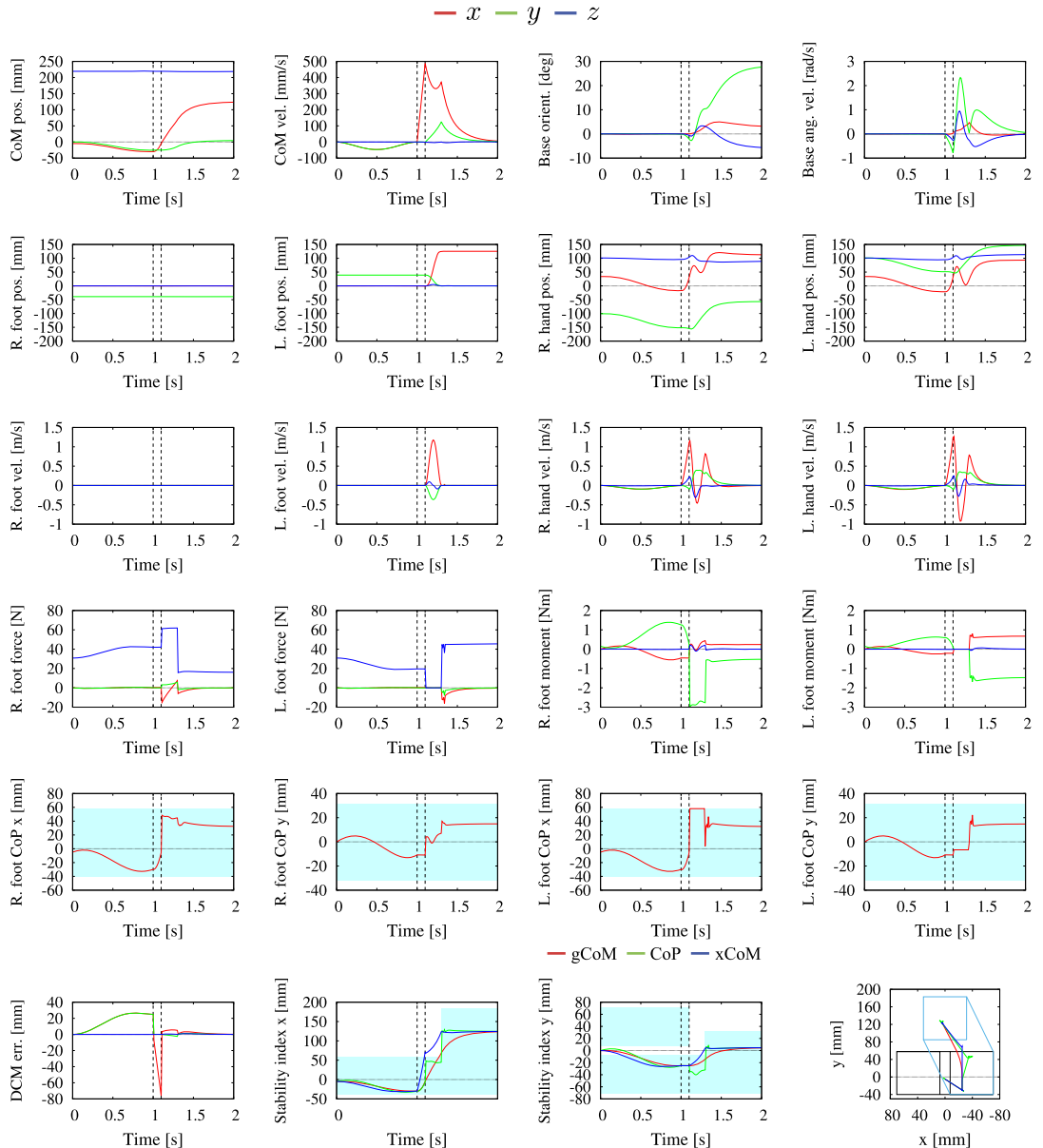


**FIGURE 7.33** Data graphs for a simulation of reactive stepping. Shown are the states of the CoM, the rotation of the base link and the end links, the GRFs and GRMs at the feet, the DCM error, the gCoM, the net CoP and the xCoM. The CoP coordinates are presented in the local frames, the light-blue area denotes the BoS.

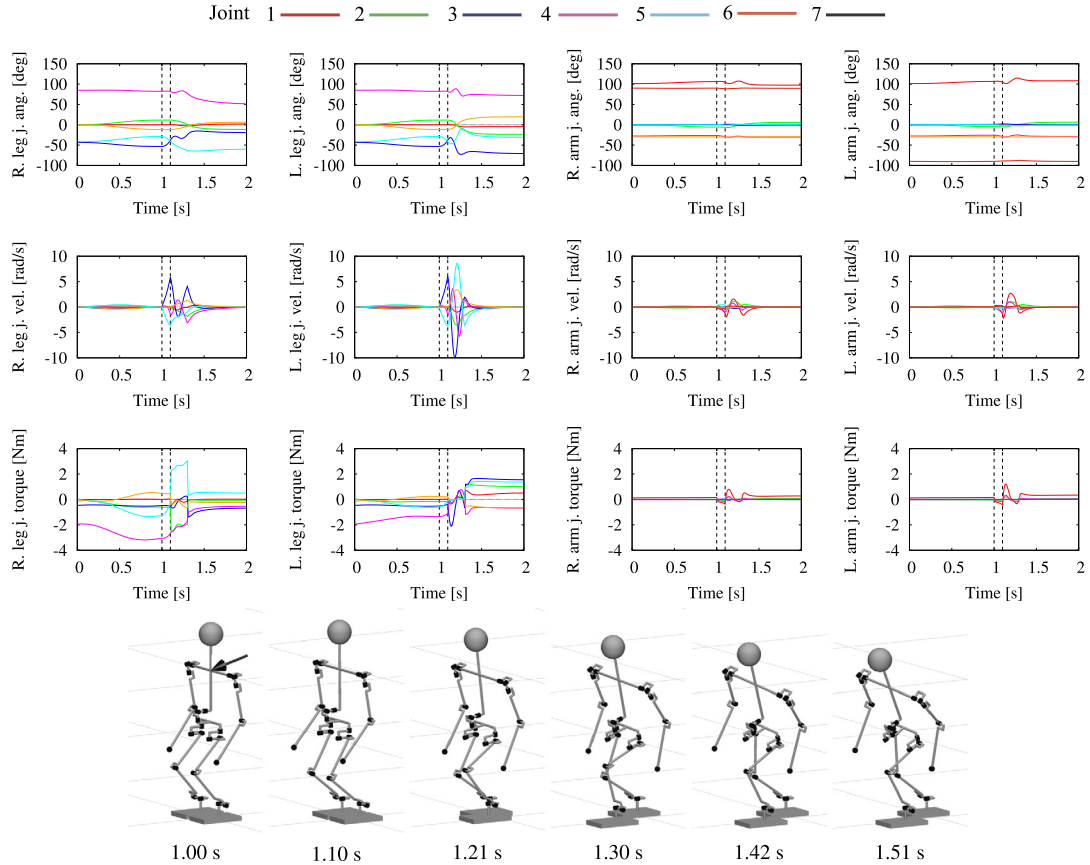


**FIGURE 7.34** Data graphs for a simulation of reactive stepping. Shown are the graphs for the variations in the joint angles, rates, and torques in time. Snapshots from the animated motion as shown at the bottom of the figure.

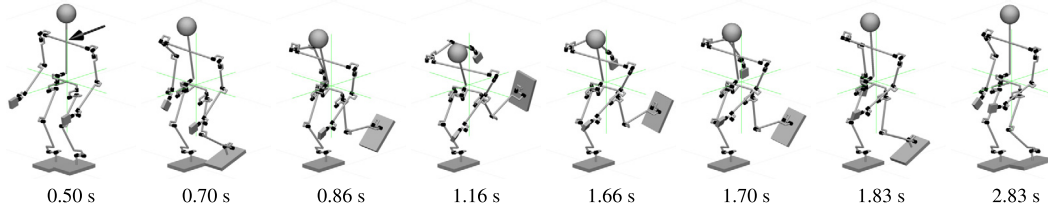
area denotes the BoS. Furthermore, the data graphs for the joint-space quantities (joint angles, rates, and torques) are shown in Fig. 7.34. From the graphs, a stable stepping response can be confirmed.

With the above approach, there is some ambiguity in the parameter setting. The stepping parameters depend on the torque and velocity constraints. In the case of constraint violation, the stepping time could be increased and/or a smaller step could be taken, at the expense of a smaller dynamic stability margin. As an alternative, the motion planning and generation processes can be formulated as a recursive optimization task (a QP task) that includes the above constraints, as suggested in [27].

It should be noted that the impact applied was relatively large; it was impossible to accommodate the impact with a synergetic motion, neither with the ankle nor with the hip/twist synergies or combinations thereof. In Section 7.7.6, an RNS-based accommodation approach will be explored as an alternative.

**TABLE 7.6** Gain scheduling and snapshots for accommodating a large impact without stepping

Phase	Preimpact		Impact	Postimpact I	Postimpact II	
Time [s]	0 ~ 0.4	0.4 ~ 0.5	1.0 ~ 1.1	1.1 ~ 1.6	1.6 ~ 3.0	3.0 ~
$K_{o_B}$ (P-gain)	300	300 ~ 0.01		0.01	0.01 ~ 300	300
$K_{\omega_B}$ (D-gain)	50	50 ~ 0.001	0.001	0.001 ~ 5	5 ~ 50	50



### 7.7.6 Accommodating a Large Impact Without Stepping

The main idea behind accommodating a large impact without stepping is to make use of the whole-body motion generation and control approach with angular momentum damping from the RNS, when the robot is in a single stance. In this way, the motion in the free leg can contribute, together with that in the upper torso and the arm motion, to the dissipation of the energy of the impact. The *relative angular acceleration* control framework from Section 7.7.4 is suitable to implement the RNS balance controller. During the reflex phase, an anticipatory type of behavior is assumed, i.e. the virtual-spring gain for the impact accommodating base rotation is preset at a relatively low value *before* the impact. The gain is also held at that value during the phases Impact and Postimpact I.

The performance of the designed controller is examined with a simulation. The initial xCoM and the impact parameters were set as in the reactive stepping simulation in Section 7.7.5.<sup>5</sup> The initial posture is an SS one, the left foot being lifted off the floor. The timing of the impact and the gain scheduling setting are apparent from Table 7.6. The resulting motion can be seen in Video 7.7-8 [38].

The graphs from the simulation are displayed in Figs. 7.35 and 7.36. The graphs in Fig. 7.35 are for the CoM position and velocity, the base-link orientation and the angular velocity, the end-link positions/orientations and the respective velocities/angular velocities, the CRB, the coupling and the system angular momentum (abbreviated as CRB-AM, CAM, and SAM, respectively), the respective rates of change, and, finally, the CoP graphs. In Fig. 7.36, graphs for the joints-space quantities (joint angles, rates, and torques) are shown. From the snapshots, the video, and the graphs it is apparent that the large impact has been accommodated successfully. The impact induced a rotational disturbance in the support foot, but only instantaneously. The state was recovered swiftly with the relative angular acceleration control law. The energy of the impact was dissipated in the postimpact phases, s.t. the robot came to rest without disturbing the stance foot state significantly.

<sup>5</sup> Recall that the impact was such that it could not be accommodated with any of the known synergies.

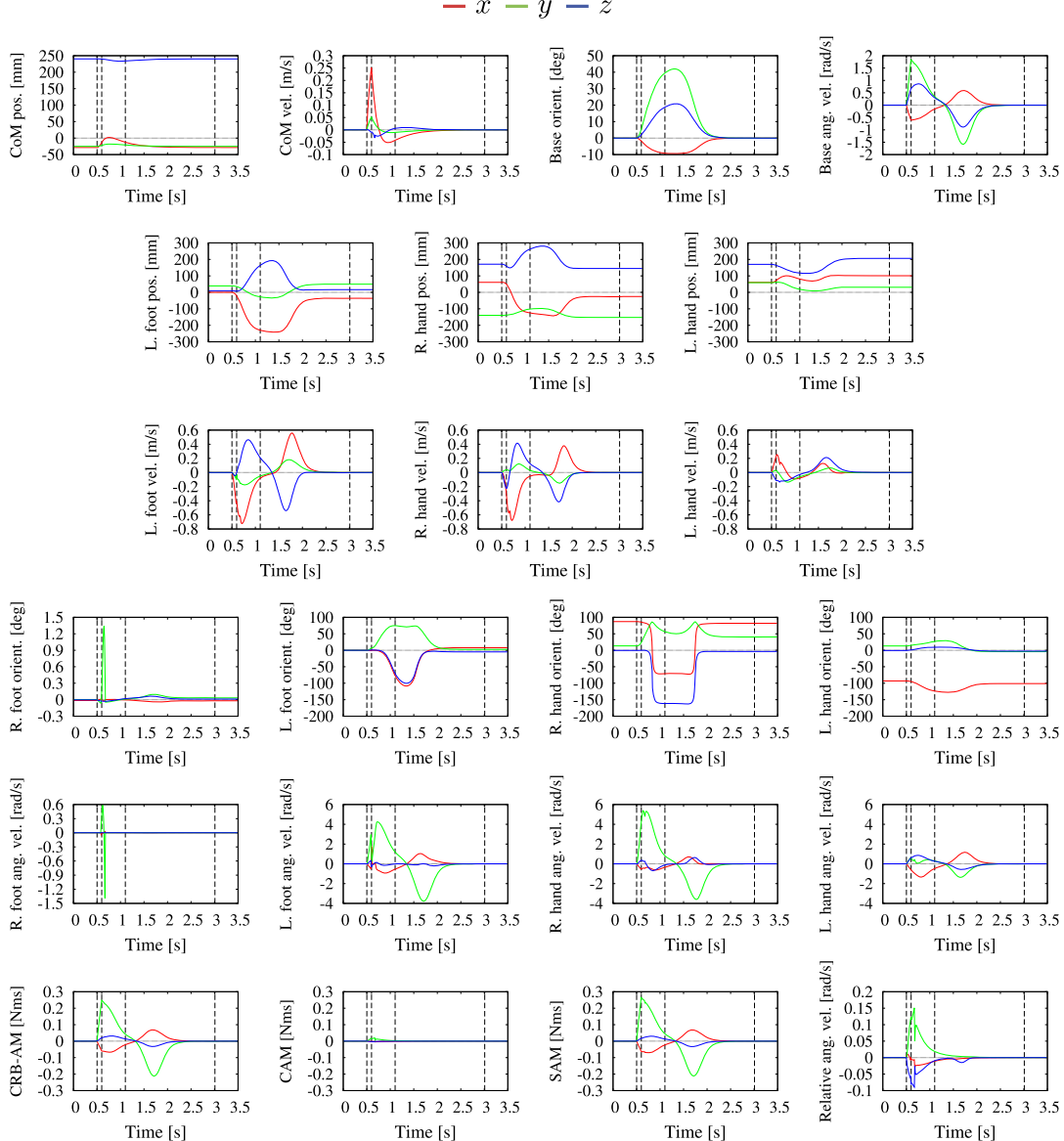


**FIGURE 7.35** Accommodation of a large impact on the back without stepping. The graphs are for the CoM position and velocity, the base-link orientation and angular velocity, the end-link positions/orientations and the respective velocities/angular velocities, the CRB, the coupling and the system angular momentum (abbreviated as CRB-AM, CAM and SAM, respectively), the reference rates of change of the angular momenta, and finally, the CoP. The light-blue areas stand for the BoS.

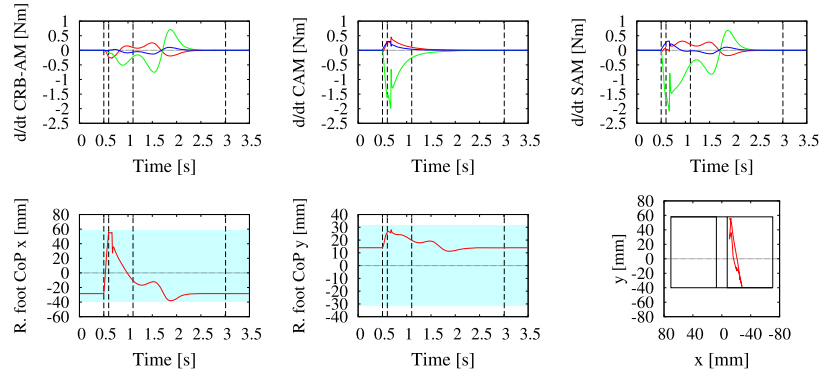


FIGURE 7.35 (Continued.)

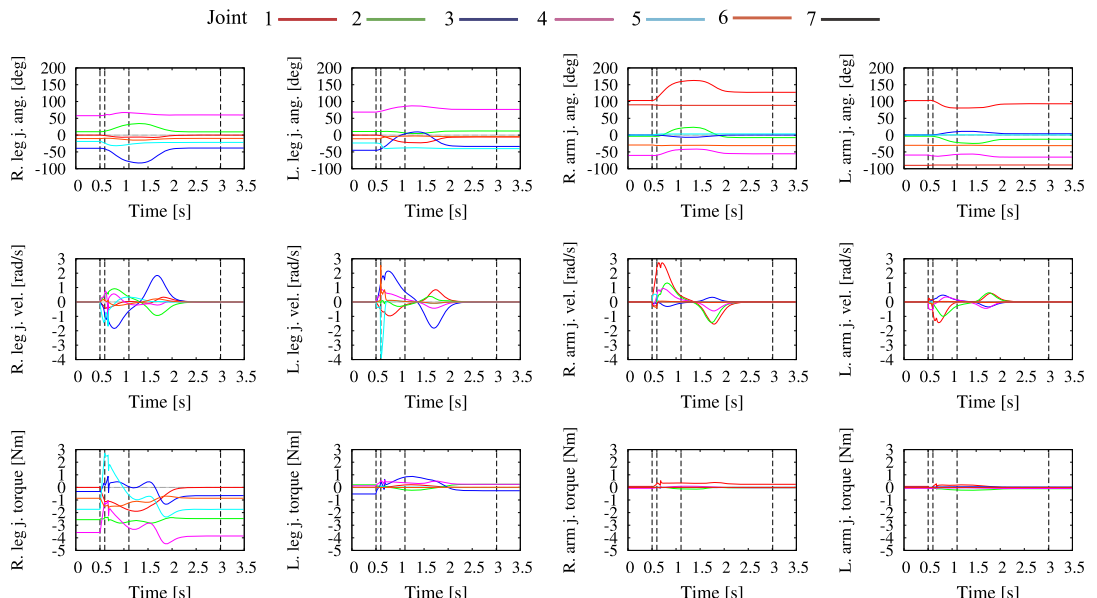


FIGURE 7.36 Accommodation of a large impact on the back without stepping. The graphs are for the joint-space quantities (joint angles, rates and torques).

From the above example it becomes apparent that with the RNS balance control approach it is possible to accommodate relatively large impacts without taking a step. Up to now, such type of impacts would require taking one or more steps, according to the N-step capturability theory [67]. The above result means that the theory can be further developed in the direction of increasing the zero-step capturability region via RNS-based motion generation and control.

## 7.8 IMPACT MOTION GENERATION

An impact motion is defined here as a motion that generates impulsive forces when contacting objects from the environment, whereby the magnitude of the force exerted on the object is not limited by the actuator torque constraints, as is the case for forces generated under static conditions.

### 7.8.1 Historical Background

When a fixed-base robot arm collides with a hard environment, there is a possibility of control destabilization due to a flip-flop-type transition between the free and constrained spaces. A humanoid robot that comprises a floating base may fall down if a large impulsive force is applied to its body. These examples show that the dynamics of impacts play an important role in modeling and control. Indeed, a considerable number of studies have been conducted in this field over the past few decades.

An impact dynamics model suitable for fixed-base robots was discussed in [128]. In order to avoid an excessive impulse force at collision, numerous control approaches have been proposed so far. They include the optimum approach velocity for force-controlled contacts [86, 59], an impact control scheme for stable hard-on-hard contact [110], a discontinuous control approach for transition between a noncontact and contact motion [80], a unified control strategy capable of achieving stable contact within both hard and soft environments [77], and a sensor-referenced control method using positive acceleration feedback and a switching control strategy [107]. In order to analyze and evaluate the effects of impacts on fixed-base robots, some measures have been proposed such as the *virtual mass* [5], the *dynamic impact measure*, and the *generalized impact measure* [115].

In the field of biped locomotion, impacts occur at collisions between the swing leg and the floor at the end of the swing phase. This type of collision is referred to as the *heel strike*. The effect of such impacts on the stability of biped locomotion was discussed in [45,46]. In [28], biped locomotion was modeled as a nonlinear system with impulse effects. The stability of the gait was analyzed in [28,88] using a Poincaré map. The toe-off action at the end of the double support phase was modeled in [17] by an impulsive foot actuator. In [84], the contact phase after the impact was analyzed using a five-link humanoid robot model. Strategies for tripping caused by an unexpected impact at the swing leg were addressed in [95]. Impacts occurring at touchdown after jumping were analyzed in [3]. Stabilization after a hard impact was studied in [121,101].

Free-floating space robots also belong to the class of floating-base robots. In the case of a collision with a free-floating object, the state of the robot may become completely uncontrollable. The *Reaction Null Space*-based control method has been proposed to deal with such situations. This control approach can minimize the impulsive reaction wrench and the disturbance on the floating satellite base [124,90].

Most works have tried to overcome the problems caused by impacts. On the other hand, some trials have been made to harness impacts. Note that, when a robot statically applies a force to the environment, the magnitude of the force is bounded by the maximum torque of the actuators. When the applied force is in the form of an impulse, its magnitude is not

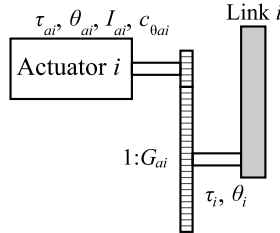


**FIGURE 7.37** The model of a robot joint driven by an actuator with a reduction gear train.

bounded in such a way. Some applications that utilize an impulsive force have been presented so far, such as hammering a nail with a 3-DOF manipulator [108], with a rigid-link manipulator [104], and with a flexible-link manipulator [54], or sawing a wooden plate [104].

If a humanoid robot could do heavy work utilizing impulsive forces as well as a human does, the application field of humanoid robots would be drastically enlarged. Some attempts of using impulsive forces by humanoid robots have been reported so far, e.g. power lifting, diving, and gymnastics [7], pushing a wall and turning a valve [47], drum-beating [63], dynamic lifting [4], breaking woods with karate chop [78,64], and kicking a soccer ball [18].

It is important to note that when a legged robot applies an impulsive force to the environment, maintaining the balance is of utmost importance. A few works have addressed this problem, e.g. the *Adios Zero Moment Point* approach [40] (cf. Section 5.8.5).

### 7.8.2 Considering the Effects of the Reduction Gear Train

Most humanoid robots developed so far are equipped with gear trains with high reduction ratios in the joints. Such gears are generally characterized by a low joint backdrivability stemming from the friction in the gear transmission and the high effective rotor inertia. Recall that the friction and inertia moments at the actuator side are multiplied by the square of the reduction ratio, when seen from the output side. A model of a joint equipped with a high-reduction gear train is illustrated in Fig. 7.37.

Let  $\tau_{ai}$ ,  $\theta_{ai}$ ,  $I_{ai}$ , and  $c_{ai}$  be the torque, rotation angle, rotor inertia, and viscosity coefficient of the  $i$ th actuator and its gear (before reduction), respectively. Furthermore, let  $\tau_i$  and  $\theta_i$  be the torque and the rotation angle of the output side (after reduction). Suppose the reduction ratio is  $1/G_{ai}$ ;  $G_{ai}$  takes a negative value when the output shaft rotates in the direction opposite to that of the motor shaft.

The equation of motion at the actuator side can be written as follows:

$$\boldsymbol{\tau}_a = \mathbf{I}_a \ddot{\boldsymbol{\theta}}_a + \mathbf{c}_a \dot{\boldsymbol{\theta}} + \mathbf{G}_a^{-1} \boldsymbol{\tau}, \quad (7.57)$$

where

$$\boldsymbol{\tau}_a = \begin{bmatrix} \tau_{a1} \\ \vdots \\ \tau_{an} \end{bmatrix}, \quad \boldsymbol{\theta}_a = \begin{bmatrix} \theta_{a1} \\ \vdots \\ \theta_{an} \end{bmatrix}, \quad \mathbf{I}_a = \begin{bmatrix} I_{a1} & & \mathbf{0} \\ & \ddots & \\ \mathbf{0} & & I_{an} \end{bmatrix},$$

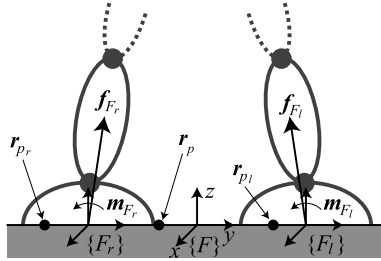


FIGURE 7.38 Reaction force and moment.

$$\mathbf{c}_a = \begin{bmatrix} c_{a1} & & \mathbf{0} \\ & \ddots & \\ \mathbf{0} & & c_{an} \end{bmatrix}, \quad \mathbf{G}_a = \begin{bmatrix} G_{a1} & & \mathbf{0} \\ & \ddots & \\ \mathbf{0} & & G_{an} \end{bmatrix},$$

and  $\tau$  is defined in (3.71). The equation of motion (7.57) can be rewritten as follows:

$$\tau = \mathbf{G}\tau_a - \mathbf{G}_a\mathbf{I}_a\mathbf{G}_a\ddot{\theta} - \mathbf{G}_a\mathbf{c}_a\mathbf{G}_a\dot{\theta} \quad (\because \theta_a = \mathbf{G}_a\theta). \quad (7.58)$$

Substituting (7.58) into (4.155), the equation of motion is rewritten as follows:

$$\begin{bmatrix} \mathbb{M}_B & \mathbf{H}_{BB} \\ \mathbf{H}_{BB}^T & \mathbf{M}_{\theta B_G} \end{bmatrix} \begin{bmatrix} \dot{\mathcal{V}}_B \\ \dot{\theta} \end{bmatrix} + \begin{bmatrix} \mathcal{C}_B \\ \mathbf{c}_{\theta B_G} \end{bmatrix} + \begin{bmatrix} \mathcal{G}_B \\ \mathbf{g}_\theta \end{bmatrix} = \begin{bmatrix} \mathbf{0} \\ \mathbf{G}\tau_a \end{bmatrix} + \begin{bmatrix} \mathbb{C}_{cB} \\ \mathcal{J}_{cB}^T \end{bmatrix} \bar{\mathcal{F}}^c, \quad (7.59)$$

where

$$\mathbf{M}_{\theta B_G} = \mathbf{M}_{\theta B} + \mathbf{G}_a\mathbf{I}_a\mathbf{G}_a, \quad \mathbf{c}_{\theta B_G} = \mathbf{c}_{\theta B} + \mathbf{G}_a\mathbf{c}_a\mathbf{G}_a\dot{\theta}. \quad (7.60)$$

Here  $\bar{\mathcal{F}}^c$  denotes the contact (reaction) forces defined in (3.61). For the definitions of  $\mathbb{C}_c$  and  $\mathcal{J}_{cB}$  refer to (2.74), (2.75), and (2.81).

### 7.8.3 Ground Reaction Force and Moment

Let  $\mathbf{f}_{F_j} \in \mathbb{R}^3$  and  $\mathbf{m}_{F_j} \in \mathbb{R}^3$  be the GRF and GRM measured at the origin of the foot coordinate system  $\{F_j\}$ ,  $j \in \{r, l\}$ , as illustrated in Fig. 7.38. The wrench  $\mathcal{F}_{F_j}$  can be written as (cf. (3.57))

$$\mathcal{F}_{F_j} = \begin{bmatrix} \mathbf{f}_{F_j} \\ \mathbf{m}_{F_j} \end{bmatrix} \triangleq \mathbb{B}_{cF_j} \bar{\mathcal{F}}^c. \quad (7.61)$$

Let  $\mathbf{r}_{F_r}$ ,  $\mathbf{r}_{F_l}$ , and  $\mathbf{r}_F$  denote the origins of coordinate systems  $\{F_r\}$ ,  $\{F_l\}$ , and  $\{F\}$ , respectively. In double-support stance, the net reaction wrench is given as follows (cf. (3.57)):

$$\mathcal{F}_F = \begin{bmatrix} \mathbf{f}_F \\ \mathbf{m}_F \end{bmatrix} = \begin{bmatrix} \mathbf{f}_{F_r} + \mathbf{f}_{F_l} \\ \mathbf{m}_{F_r} - [\mathbf{r}_{F_F}^\times] \mathbf{f}_{F_r} + \mathbf{m}_{F_l} - [\mathbf{r}_{F_F}^\times] \mathbf{f}_{F_l} \end{bmatrix}, \quad (7.62)$$

where  $\mathbf{r}_{\overleftarrow{FF}_j} = \mathbf{r}_F - \mathbf{r}_{F_j}$ . Usually, a humanoid robot is equipped with force/torque sensors mounted at the ankles or pressure sensors embedded into the soles [85,65]. The sensors detect the wrenches  $\mathcal{F}_{FS_j}$  with respect to the sensor coordinate frame  $\{FS_j\}$ . The wrench at  $\mathbf{r}_{F_j}$  is obtained from the sensor readings as follows:

$$\mathcal{F}_{F_j} = {}^W \mathbb{X}_{FS_j \overleftarrow{F_j FS_j}}^T {}^{FS_j} \mathcal{F}_{FS_j}, \quad (7.63)$$

where  ${}^W \mathbb{X}_{FS_j \overleftarrow{F_j FS_j}}^T$  is a wrench coordinate transform matrix from the force sensor coordinate frame  $\{FS_j\}$  to the world coordinate frame  $\{W\}$  (cf. (2.7)).

The net CoP  $\mathbf{r}_p$ , which is equivalent to the ZMP [111,112] on a flat ground, can be detected by the ankle force/torque sensors or the foot sole pressure sensors, in general. The wrench at  $\mathbf{r}_{F_j}$  is expressed as a function of the ZMP as follows:

$$\mathcal{F}_{F_j} = \begin{bmatrix} \mathbf{f}_{F_j} \\ \mathbf{m}_{F_j} \end{bmatrix} = \begin{bmatrix} \mathbf{f}_{p_j} \\ -[\mathbf{r}_{\overleftarrow{F_j p_j}}^\times] \mathbf{f}_{p_j} \end{bmatrix}, \quad (7.64)$$

where  $\mathbf{r}_{\overleftarrow{F_j p_j}} = \mathbf{r}_{F_j} - \mathbf{r}_{p_j}$ , and  $\mathbf{f}_{p_j} \in \mathfrak{N}^3$  is the GRF at the CoP.

Note that the z-components of  $\mathbf{r}_{p_j}$  and  $\mathbf{r}_{F_j}$  are zero because they are on the ground. The relationship between the CoP and  $\mathcal{F}_{F_j}$  is obtained as follows:

$$r_{p_{jx}} = r_{F_{jx}} - \frac{m_{F_{jy}}}{f_{F_{jz}}}, \quad r_{p_{jy}} = r_{F_{jy}} + \frac{m_{F_{jx}}}{f_{F_{jz}}}, \quad (7.65)$$

where the subscripts  $x$  and  $y$  indicate components of the respective vector quantities.

#### 7.8.4 Dynamic Effects Caused by Impacts

Suppose an impulsive force stemming from an impact is applied to a point  $\mathbf{r}_I$  of a humanoid robot at time  $t_0$ , as illustrated in Fig. 7.39. The dynamic equation at the moment of the impact is given as follows:

$$\begin{aligned} & \begin{bmatrix} \mathbb{M}_B & \mathbf{H}_{BB} \\ \mathbf{H}_{BB}^T & \mathbf{M}_{\theta B_G} \end{bmatrix} \begin{bmatrix} \dot{\mathcal{V}}_B \\ \ddot{\boldsymbol{\theta}} \end{bmatrix} + \begin{bmatrix} \mathcal{C}_B \\ \mathbf{c}_{\theta B_G} \end{bmatrix} + \begin{bmatrix} \mathcal{G}_B \\ \mathbf{g}_\theta \end{bmatrix} \\ &= \begin{bmatrix} \mathbf{0} \\ \mathbf{G}\boldsymbol{\tau}_a \end{bmatrix} + \begin{bmatrix} \mathbb{C}_{cB}(\mathbf{q}) \\ \mathcal{J}_{cB}^T(\mathbf{q}) \end{bmatrix} \left( \overline{\mathcal{F}}^c + \overline{\mathcal{I}}^c \delta(t - t_0) \right) + \begin{bmatrix} \mathbb{C}_{cB}(\mathbf{q}_I) \\ \mathcal{J}_{cB}^T(\mathbf{q}_I) \end{bmatrix} \overline{\mathcal{I}} \delta(t - t_0), \end{aligned} \quad (7.66)$$

where  $\delta(t - t_0)$  is the Dirac delta function, and hence  $\overline{\mathcal{I}} \delta(t - t_0)$  represents the impulsive force applied at  $t = t_0$ . Note that  $\overline{\mathcal{I}}$  does not include moment components;  $\overline{\mathcal{I}}^c \delta(t - t_0)$  is the reaction impulse induced by  $\overline{\mathcal{I}} \delta(t - t_0)$  at the constraint points such as feet (see Fig. 7.39) and  $\mathbf{q}_I$  is the generalized coordinate vector with respect to  $\mathbf{r}_I$ .

During the short period from  $t_0 - \Delta t/2$  to  $t_0 + \Delta t/2$ , it is assumed that the inertia matrices are quasiconstant, i.e.  $\mathbb{M}_B = \mathbf{0}$ ,  $\mathbf{H}_{BB} = \mathbf{0}$ , and  $\mathbf{M}_{\theta B_G} = \mathbf{0}$ . Therefore, from the definitions of  $\mathcal{C}_B$  and  $\mathbf{c}_{\theta B}$  given in (4.125) and (4.145), respectively, the velocity-dependent terms are zero, i.e.

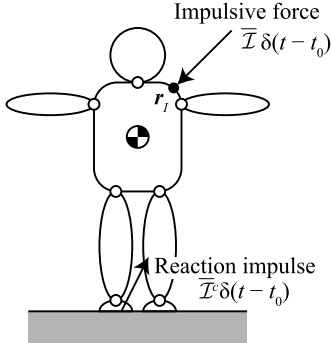


FIGURE 7.39 Impulsive force applied to a humanoid robot.

$\mathcal{C}_B = \mathbf{0}$  and  $c_{\theta B} = \mathbf{0}$ . Furthermore, it can be assumed that the gravitational terms  $\mathcal{G}_B$  and  $\mathbf{g}_\theta$ , the actuator torque  $\tau_a$ , and the constraint wrench  $\bar{\mathcal{F}}^c$  are also quasiconstant during the short period from  $t_0 - \Delta t/2$  to  $t_0 + \Delta t/2$ .

Integrating both sides of (7.66), the following equation is obtained:

$$\begin{aligned}
 \begin{bmatrix} \mathbb{M}_B & \mathbf{H}_{BB} \\ \mathbf{H}_{BB}^T & \mathbf{M}_{\theta B_G} \end{bmatrix} \begin{bmatrix} \Delta \mathcal{V}_B \\ \Delta \dot{\theta} \end{bmatrix} &= \int_{t_0 - \frac{\Delta t}{2}}^{t_0 + \frac{\Delta t}{2}} \left\{ - \begin{bmatrix} \mathbf{0} \\ \mathbf{G}_a \mathbf{c}_a \mathbf{G}_a \dot{\theta} \end{bmatrix} - \begin{bmatrix} \mathcal{G}_B \\ \mathbf{g}_\theta \end{bmatrix} + \begin{bmatrix} \mathbf{0} \\ \mathbf{G} \boldsymbol{\tau}_a \end{bmatrix} + \begin{bmatrix} \mathcal{C}_{cB}(\mathbf{q}) \\ \mathcal{J}_{cB}^T(\mathbf{q}) \end{bmatrix} \bar{\mathcal{F}}^c \right\} dt \\
 &\quad + \int_{t_0 - \frac{\Delta t}{2}}^{t_0 + \frac{\Delta t}{2}} \left\{ \begin{bmatrix} \mathcal{C}_{cB}(\mathbf{q}) \\ \mathcal{J}_{cB}^T(\mathbf{q}) \end{bmatrix} \bar{\mathcal{I}}^c \delta(t - t_0) + \begin{bmatrix} \mathcal{C}_{cB}(\mathbf{q}_I) \\ \mathcal{J}_{cB}^T(\mathbf{q}_I) \end{bmatrix} \bar{\mathcal{I}} \delta(t - t_0) \right\} dt \\
 &= - \begin{bmatrix} \mathbf{0} \\ \mathbf{G}_a \mathbf{c}_a \mathbf{G}_a [\boldsymbol{\theta}(t)]_{t_0 - \frac{\Delta t}{2}}^{t_0 + \frac{\Delta t}{2}} \end{bmatrix} + \left\{ - \begin{bmatrix} \mathcal{G}_B \\ \mathbf{g}_\theta \end{bmatrix} + \begin{bmatrix} \mathbf{0} \\ \mathbf{G} \boldsymbol{\tau}_a \end{bmatrix} + \begin{bmatrix} \mathcal{C}_{cB}(\mathbf{q}) \\ \mathcal{J}_{cB}^T(\mathbf{q}) \end{bmatrix} \bar{\mathcal{F}}^c \right\} \Delta t \\
 &\quad + \left\{ \begin{bmatrix} \mathcal{C}_{cB}(\mathbf{q}) \\ \mathcal{J}_{cB}^T(\mathbf{q}) \end{bmatrix} \bar{\mathcal{I}}^c + \begin{bmatrix} \mathcal{C}_{cB}(\mathbf{q}_I) \\ \mathcal{J}_{cB}^T(\mathbf{q}_I) \end{bmatrix} \bar{\mathcal{I}} \right\} \int_{t_0 - \frac{\Delta t}{2}}^{t_0 + \frac{\Delta t}{2}} \delta(t - t_0) dt \\
 &= \begin{bmatrix} \mathcal{C}_{cB}(\mathbf{q}) \\ \mathcal{J}_{cB}^T(\mathbf{q}) \end{bmatrix} \bar{\mathcal{I}}^c + \begin{bmatrix} \mathcal{C}_{cB}(\mathbf{q}_I) \\ \mathcal{J}_{cB}^T(\mathbf{q}_I) \end{bmatrix} \bar{\mathcal{I}}, \tag{7.67}
 \end{aligned}$$

because

$$\int_{t_0 - \frac{\Delta t}{2}}^{t_0 + \frac{\Delta t}{2}} \delta(t - t_0) dt = 1, \quad \lim_{\Delta t \rightarrow 0} \left[ \boldsymbol{\theta}(t) \right]_{t_0 - \frac{\Delta t}{2}}^{t_0 + \frac{\Delta t}{2}} = \mathbf{0},$$

and, since  $\mathcal{G}_B$ ,  $\mathbf{g}_\theta$ ,  $\boldsymbol{\tau}_a$ , and  $\bar{\mathcal{F}}^c$  are assumed to be quasiconstant during the short period, the terms  $\mathcal{G}_B \Delta t$ ,  $\mathbf{g}_\theta \Delta t$ ,  $\boldsymbol{\tau}_a \Delta t$ , and  $\bar{\mathcal{F}}^c \Delta t$  vanish as  $\Delta t \rightarrow 0$  [128]. The differences  $\Delta \mathcal{V}_B$  and  $\Delta \dot{\theta}$  are defined as follows:

$$\Delta \mathcal{V}_B = \mathcal{V}_B^+ - \mathcal{V}_B^-, \quad \Delta \dot{\theta} = \dot{\theta}^+ - \dot{\theta}^-,$$

where  $\mathcal{V}_B^+$  and  $\dot{\theta}^+$  are the base and the joint velocity after the impact, while  $\mathcal{V}_B^-$  and  $\dot{\theta}^-$  are the velocities before the impact, respectively.

The differences in the velocities are obtained from (7.67) as

$$\begin{bmatrix} \Delta \mathcal{V}_B \\ \Delta \dot{\theta} \end{bmatrix} = \begin{bmatrix} X_{11} & X_{12} \\ X_{21} & X_{22} \end{bmatrix} \left\{ \begin{bmatrix} \mathbb{C}_{cB}(\mathbf{q}) \\ \mathcal{J}_{cB}^T(\mathbf{q}) \end{bmatrix} \bar{\mathcal{I}}^c + \begin{bmatrix} \mathbb{C}_{cB}(\mathbf{q}_I) \\ \mathcal{J}_{cB}^T(\mathbf{q}_I) \end{bmatrix} \bar{\mathcal{I}} \right\}, \quad (7.68)$$

where

$$\begin{aligned} X_{11} &= \left( \mathbb{M}_B - \mathbf{H}_{BB} \mathbf{M}_{\theta B_G}^{-1} \mathbf{H}_{BB}^T \right)^{-1}, \\ X_{12} &= - \left( \mathbb{M}_B - \mathbf{H}_{BB} \mathbf{M}_{\theta B_G}^{-1} \mathbf{H}_{BB}^T \right)^{-1} \mathbf{H}_{BB} \mathbf{M}_{\theta B_G}^{-1}, \\ X_{21} &= - \left( \mathbf{M}_{G\theta_B} - \mathbf{H}_{BB}^T \mathbb{M}_B^{-1} \mathbf{H}_{BB} \right)^{-1} \mathbf{H}_{BB}^T \mathbb{M}_B^{-1}, \\ X_{22} &= \left( \mathbf{M}_{G\theta_B} - \mathbf{H}_{BB}^T \mathbb{M}_B^{-1} \mathbf{H}_{BB} \right)^{-1}. \end{aligned}$$

As discussed in Section 7.8.2, most humanoid robots are equipped with high-reduction gear trains in their joints. When the gear reduction ratios (the diagonal elements of  $\mathbf{G}_a$ ) are large enough, the diagonal elements of  $\mathbf{M}_{G\theta_B}$  become quite large (see (7.60)). The inverse of  $\mathbf{M}_{\theta B_G}$  can then be approximated as  $\mathbf{M}_{\theta B_G}^{-1} \simeq \mathbf{0}_{n \times n}$ . In this case, the submatrices  $X_{11}$ ,  $X_{12}$ ,  $X_{21}$ , and  $X_{22}$  can be approximated as follows:

$$X_{11} \simeq \mathbb{M}_B^{-1}, \quad X_{12} \simeq \mathbf{0}, \quad X_{21} \simeq \mathbf{0}, \quad X_{22} \simeq \mathbf{0}. \quad (7.69)$$

Substituting (7.69) into (7.68), the following equation is obtained:

$$\begin{bmatrix} \Delta \mathcal{V}_B \\ \Delta \dot{\theta} \end{bmatrix} \simeq \begin{bmatrix} \mathbb{M}_B^{-1} \left\{ \mathbb{C}_{cB}(\mathbf{q}) \bar{\mathcal{I}}^c + \mathbb{C}_{cB}(\mathbf{q}_I) \bar{\mathcal{I}} \right\} \\ \mathbf{0} \end{bmatrix}. \quad (7.70)$$

The above equation indicates that a humanoid robot with high reduction ratios in the joints (and hence, low backdrivability) behaves as a CRB during the impulse.

### 7.8.5 Virtual Mass

Fig. 7.40 visualizes the concept of a *virtual mass* [5], also referred to as the *equivalent mass*. The virtual mass is a point mass which is equivalent to the mass of the robot reflected at the contact point. The virtual mass of a fixed-base robot can be determined as the ratio of the impulsive force to the resultant acceleration [5]. It should be noted that the original definition of the virtual mass does not consider the friction in the joints. The virtual mass concept was adopted in free-floating space robots with joint resistance, by introducing the *joint resistance factor* [123].

In this section, the virtual mass concept is discussed considering the effects of the reduction gear train. Unilateral point contacts are assumed at the collision points between the robot and

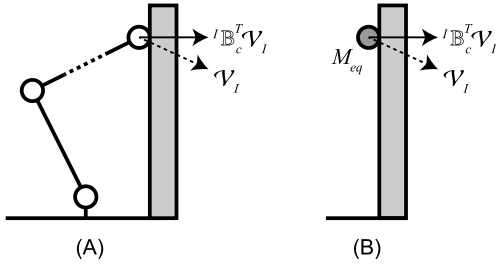


FIGURE 7.40 Equivalent point mass. (A) Robot manipulator. (B) Equivalent point mass.

the environment. Hence, the collision does not produce an impulsive moment. Under this assumption, the constraint basis  $'\mathbb{B}_c$  can be written as

$$'\mathbb{B}_c = \begin{bmatrix} \mathbf{e}_{nI} \\ \mathbf{0}_{3 \times 1} \end{bmatrix} \in \Re^{6 \times 1}, \quad (7.71)$$

where  $\mathbf{e}_{nI} \in \Re^3$  is the unit vector normal to the constraint surface. As illustrated in Fig. 7.40, the component of  $\mathcal{V}_I$  that is normal to the constraint surface is given by  $'\mathbb{B}_c^T \mathcal{V}_I$ .

The difference between the velocity at the impact point before the impact,  $\mathcal{V}_I^-$ , and that after the impact,  $\mathcal{V}_I^+$ , is expressed with respect to the world coordinate system as follows:

$$\Delta \mathcal{V}_I = \mathbb{T}_{BI}^{-1} \Delta \mathcal{V}_B + \mathbf{J}(\boldsymbol{\theta}_I) \Delta \dot{\boldsymbol{\theta}}_I. \quad (7.72)$$

Substituting (7.70) into (7.72),  $\Delta \mathcal{V}_I$  is rewritten as follows:

$$\begin{aligned} \Delta \mathcal{V}_I &= \mathbb{T}_{BI}^{-1} \mathbb{M}_B^{-1} \mathbb{C}_{cB}(\mathbf{q}) \bar{\mathcal{I}}^c + \mathbb{T}_{BI}^{-1} \mathbb{M}_B^{-1} \mathbb{C}_{cB}(\mathbf{q}_I) \bar{\mathcal{I}}^c \\ &= \left\{ \mathbb{T}_{BI}^{-1} \mathbb{M}_B^{-1} \mathbb{C}_{cB}(\mathbf{q}) \frac{\bar{\mathcal{I}}^c}{\bar{\mathcal{I}}} + \mathbb{T}_{BI}^{-1} \mathbb{M}_B^{-1} \mathbb{C}_{cB}(\mathbf{q}_I) \right\} \bar{\mathcal{I}}. \end{aligned} \quad (7.73)$$

If a point mass  $M_{eq}$  collides with an object from the environment, the generated impulse would be

$$M_{eq} ' \mathbb{B}_c^T \Delta \mathcal{V}_I = \bar{\mathcal{I}}. \quad (7.74)$$

Comparing (7.74) with (7.73), the equivalent mass is given as follows:

$$M_{eq} = \frac{1}{' \mathbb{B}_c^T \mathbb{T}_{BI}^{-1} \mathbb{M}_B^{-1} \mathbb{C}_{cB}(\mathbf{q}) \frac{\bar{\mathcal{I}}^c}{\bar{\mathcal{I}}} + ' \mathbb{B}_c^T \mathbb{T}_{BI}^{-1} \mathbb{M}_B^{-1} \mathbb{C}_{cB}(\mathbf{q}_I)}. \quad (7.75)$$

The equivalent mass can be utilized to generate the whole-body motion that maximizes/minimizes the impulsive force. An example of motion generation using the equivalent mass is given in Section 7.8.

### 7.8.6 CoP Displacement Induced by the Impulsive Force

Suppose that only the feet are constrained, with plane contacts on a flat floor (i.e. the hands are completely free). If the humanoid robot can keep the plane contacts after the impact without slipping, the base velocity difference  $\Delta\mathcal{V}_B$  will be zero. The upper part of (7.70) can then be rewritten as

$$\mathbb{C}_{cB}(\mathbf{q}_F)\bar{\mathcal{I}}_F^c + \mathbb{C}_{cB}(\mathbf{q}_I)\bar{\mathcal{I}} = \mathbf{0}. \quad (7.76)$$

The reactive impulse can be calculated from (7.76) and the definition of  $\mathbb{C}_{cB}$  (cf. (2.74)) as

$$\mathcal{I}_F^c = {}^I\mathbb{B}_c(\mathbf{q}_F)\bar{\mathcal{I}}_F^c = -\mathbb{T}_{FB}^T \mathbb{C}_{cB}\bar{\mathcal{I}}. \quad (7.77)$$

The reactive impulse can be expressed as

$$\mathcal{I}_F^c \triangleq \begin{bmatrix} (\mathbf{f}_F^{\mathcal{I}c})^T & (\mathbf{m}_F^{\mathcal{I}c})^T \end{bmatrix} \Delta t = \begin{bmatrix} f_{Fx}^{\mathcal{I}c} & f_{Fy}^{\mathcal{I}c} & f_{Fz}^{\mathcal{I}c} & m_{Fx}^{\mathcal{I}c} & m_{Fy}^{\mathcal{I}c} & m_{Fz}^{\mathcal{I}c} \end{bmatrix}^T \Delta t. \quad (7.78)$$

From the relationship between  $f_F^{\mathcal{I}c}$  and  $\mathbf{m}_F^{\mathcal{I}c}$  given in (7.77), the CoP displacement  $\Delta\mathbf{r}_p$  induced by the impact  $\bar{\mathcal{I}}$  is estimated as

$$\Delta r_{px} = -\frac{m_{Fy}^{\mathcal{I}c}}{f_{Fz}^{\mathcal{I}c}}, \quad \Delta r_{py} = \frac{m_{Fx}^{\mathcal{I}c}}{f_{Fz}^{\mathcal{I}c}}. \quad (7.79)$$

Note that there is no consideration for the dimension of the supporting polygon in the calculation of (7.79), hence the obtained CoP is the *imaginary ZMP* [113] (also known as the *Foot Rotation Indicator* (FRI) [26]).

### 7.8.7 Optimization Problems for Impact Motion Generation

The impact force (the acting force) generated during the impact motion should be as large as possible and should not lead to balance deterioration after the impact. Thus, the objective of the impact motion is to maximize (i) the impact force and (ii) the stability margin in the balance control.

In the impact motion generation approach presented in [64], the initial and final positions were not explicitly specified as boundary conditions. Instead, the position and velocity at the impact were determined by solving an optimization problem. Then, decelerating the motion at impact forwards and backwards in time, the initial and final positions were determined. The concept of this type of motion generation is illustrated in Fig. 7.41. This approach comprises the following five steps:

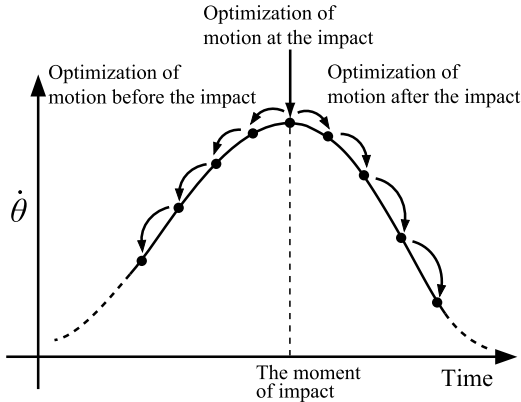


FIGURE 7.41 Conceptual sketch of the impact motion generation approach in [64].

**Step 1:**  $\theta(t)$  and  $\dot{\theta}(t)$  at the moment of impact  $t = t_I$  are determined so that the objective function  $J_I$  is minimized.

**Step 2:**  $\dot{\theta}$  at  $t = t_I - \Delta t$  is determined so that the objective function  $J_{baI}$  is minimized.

**Step 3:** Step 2 is iterated with  $t = t - \Delta t$  until  $\dot{\theta}(t)^T \dot{\theta}(t)$  becomes zero.

**Step 4:**  $\dot{\theta}$  at  $t = t_I + \Delta t$  is determined so that the objective function  $J_{baI}$  (the same function used in Step 2) is minimized.

**Step 5:** Step 4 is iterated with  $t = t + \Delta t$  until  $\dot{\theta}(t)^T \dot{\theta}(t)$  becomes zero.

Here  $\theta(t)$  and  $\dot{\theta}(t)$  denote the joint angle and angular velocity vectors, respectively;  $\Delta t$  stands for the time step.

As a result of the optimization before/after the impact, the joint velocity vector  $\dot{\theta}(t)$  that minimizes the given objective function  $J_{baI}$  will be obtained. The joint angle vector  $\theta(t)$  and the joint acceleration  $\ddot{\theta}(t)$  are calculated as follows:

$$\theta(t) = \begin{cases} \theta(t + \Delta t) - \dot{\theta}(t)\Delta t & \text{(for the motion before the impact)} \\ \theta(t - \Delta t) + \dot{\theta}(t)\Delta t & \text{(for the motion after the impact)} \end{cases} \quad (7.80)$$

$$\ddot{\theta}(t) = \begin{cases} \frac{\dot{\theta}(t + \Delta t) - \dot{\theta}(t)}{\Delta t} & \text{(for the motion before the impact)} \\ \frac{\dot{\theta}(t) - \dot{\theta}(t - \Delta t)}{\Delta t} & \text{(for the motion after the impact).} \end{cases} \quad (7.81)$$

Furthermore, limits on the joint angles and their time derivatives are imposed in the form of the following inequality constraints:

$$\theta_{i,\min} \leq \theta_i(t) \leq \theta_{i,\max}, \quad (7.82)$$

$$-\dot{\theta}_{i,\max} \leq \dot{\theta}_i(t) \leq \dot{\theta}_{i,\max}, \quad (7.83)$$

$$-\ddot{\theta}_{i,\max} \leq \ddot{\theta}_i(t) \leq \ddot{\theta}_{i,\max}. \quad (7.84)$$

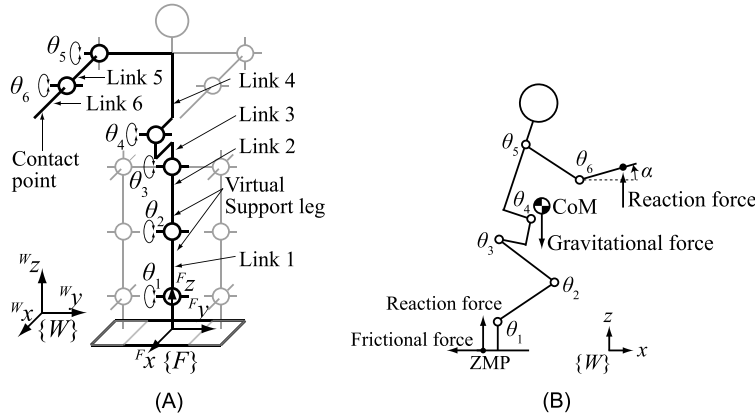


FIGURE 7.42 (A) A simplified model of the humanoid robot HOAP-2. (B) Side view of the model.

Here  $\theta_i(t)$  denotes the angle of the  $i$ th joint at  $t$ ,  $\dot{\theta}_i(t)$  and  $\ddot{\theta}_i(t)$  are the first and second time derivatives. Substituting (7.81) into (7.84), the constraints for the joint rates are obtained as

$$\begin{cases} \dot{\theta}_i(t + \Delta t) - \ddot{\theta}_{i,\max} \Delta t \leq \dot{\theta}_i(t) \leq \dot{\theta}_i(t + \Delta t) + \ddot{\theta}_{i,\max} \Delta t & \text{(for the motion before the impact)} \\ \dot{\theta}_i(t - \Delta t) - \ddot{\theta}_{i,\max} \Delta t \leq \dot{\theta}_i(t) \leq \dot{\theta}_i(t - \Delta t) + \ddot{\theta}_{i,\max} \Delta t & \text{(for the motion after the impact).} \end{cases} \quad (7.85)$$

In the case the joint acceleration given in (7.81) can be ensured during the entire motion, it can be said that the generated motion is continuous. Such a motion can be obtained by constraining the joint velocity as in (7.85). The maximum joint acceleration can be estimated from (7.59) as

$$\ddot{\theta}_{\max} = M_{G\theta}^{-1} (G\tau_{a,\max} - c_{\theta B_G} + g_{\theta}), \quad (7.86)$$

for  $\dot{\theta}_B = 0$  and  $F_{hi} = 0$ . Note that the maximum joint acceleration depends on the arm dynamics. In order to obtain an accurate  $\ddot{\theta}_{\max}(t)$ , these dynamics have to be solved at every iteration during optimization. This approach is not realistic, however, due to the computational cost. This problem can be alleviated in case the minimum value of  $\ddot{\theta}_{\max}(t)$  is estimated in advance.

### 7.8.8 A Case Study: Karate Chop Motion Generation

#### **A Simplified Model of the Humanoid Robot HOAP-2**

The humanoid robot HOAP-2 (Fujitsu Automation) comprising 25 DoFs is chosen as the test platform for the Karate chop experiments. For the impact motion generation task, a simplified, planar 6-DoF model is used, as shown in Fig. 7.42. The simplified model consists of six links and six joints. The left and right legs of the real robot are combined into a virtual support leg in the simplified model, as illustrated in Fig. 7.42A. Therefore, the masses of Links 1 and 2 are the sums of the masses of the corresponding left and right leg links, respectively. The masses of each link of the simplified model are listed in Table 7.7.

**TABLE 7.7** Mass distribution of the HOAP-2 model

	Link 1	Link 2	Link 3	Link 4	Link 5	Link 6
Mass (kg)	0.57	0.88	0.92	2.45	0.62	0.17

**TABLE 7.8** Joint limitations

<i>i</i>	1	2	3	4	5	6
$\theta_{i,\min}$ (°)	-60	-130	-70	0	-90	-115
$\theta_{i,\max}$ (°)	60	0	80	90	90	0

The joint limits of the simplified model are specified in accordance with those of the real robot, as listed in Table 7.8. The maximum joint velocity for each joint is set at  $\pi$  rad/s, which is the actual limit of the actuators used in the real robot.

### Performance Index for Impact Force Evaluation

First, recall that the objective of the impact motion is to maximize the impact force (acting force) and the stability margin (cf. Section 7.8.7). When a link of the robot collides with an object from the environment the generated impulse can be obtained as a difference between the pre- and postimpact momenta. Using the equivalent mass relation (7.74), the preimpact momentum can be expressed as  $M_{eq}{}^I\mathbb{B}_c^T\mathcal{V}_I^+$ , where  ${}^I\mathbb{B}_c$  is the constraint basis at the instantaneous contact joint established at the point of collision (cf. (7.71)). This momentum can be used as a performance index for the impact force minimization goal. Note that  ${}^I\mathbb{B}_c^T\mathcal{V}_I^+$  denotes the component of  $\mathcal{V}_I^+$  along the normal to the contact surfaces at the collision point (see Fig. 7.40B).

### Performance Index for Stability Margin Evaluation

The dynamic equation of a humanoid robot, as given in (4.155) will be employed in the following derivations. Recall that the spatial dynamics relationship (4.130) stems from the upper part of (4.155) and the expression for the *system spatial momentum* (SSM). This relationship can be rewritten with respect to the foot coordinate system  $\{F\}$  as

$$\frac{d}{dt}\mathcal{L}_F + \mathcal{G}_F = \mathcal{F}_F, \quad (7.87)$$

where

$$\frac{d}{dt}\mathcal{L}_F = \frac{d}{dt} \left( {}^F\mathbb{X}_B^T \mathcal{L}_B(\mathbf{q}, \dot{\mathbf{q}}_B) \right) \equiv \begin{bmatrix} \dot{\mathbf{p}} \\ \dot{\mathbf{l}}_F \end{bmatrix}, \quad \mathcal{G}_F = M \begin{bmatrix} -\mathbf{E}_3 \\ [\mathbf{r}_{FC}^\times] \end{bmatrix} \mathbf{a}_g, \quad \mathcal{F}_F = \begin{bmatrix} \mathbf{f}_F \\ \mathbf{m}_F \end{bmatrix},$$

and  $M$  is the total mass of the robot,  $\mathbf{a}_g = [0 \ 0 \ -g]^T$  is the gravitational acceleration vector,  $\mathbf{r}_{FC}^\times$  is the position of the origin of  $\{F\}$  w.r.t. the CoM.  $f_{pz}$  and  $m_{Fy}$  are calculated from (7.87) as

$$f_{Fz} = \dot{p}_z + Mg, \quad m_{Fy} = \dot{l}_{Fy} + (\mathbf{r}_{FC})_x Mg. \quad (7.88)$$

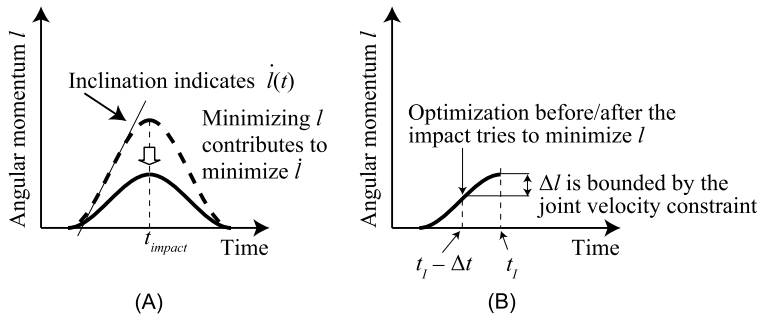


**FIGURE 7.43** Minimizing angular momentum  $l$  in: (A) optimization at the impact and (B) optimization before/after the impact.

Substituting (7.88) into (7.65), the  $x$ -coordinate of the CoP is expressed using the time derivative of SSM as follows:

$$\left( \dot{\mathbf{r}}_{pF} \right)_x = - \frac{i_{Fy} + \left( \dot{\mathbf{r}}_{FC} \right)_x Mg}{Mg + \dot{p}_z}. \quad (7.89)$$

In general, the rate of change of the linear momentum along the  $z$ -axis,  $\dot{p}_z$ , can be assumed much smaller than the gravitational force  $Mg$ . From the above relation it follows then that the rate of change of the angular momentum around the  $y$ -axis,  $i_{Fy}$ , is the crucial parameter that will dominantly affect the  $x$ -coordinate of the CoP.

In the impact motion generation approach discussed here, it is assumed that the robot is stationary at the initial ( $t = 0$ ) and final ( $t = T$ ) postures. Hence,  $\mathbf{p}(0) = \mathbf{p}(T) = \mathbf{0}$  and  $\mathbf{l}_F(0) = \mathbf{l}_F(T) = \mathbf{0}$ . Furthermore, in the optimization process, the angular momentum is constrained to take its maximum value at the impact and to be monotonically reduced before/after the impact, as illustrated in Fig. 7.41. That is why it can be assumed that minimizing  $i_F^2$  will contribute to the minimization of  $i_F$ , as illustrated in Fig. 7.43A. On the contrary, during the optimization before/after the impact, the minimization of  $i_F^2$  at  $t = t_I \pm \Delta t$  yields an increase in  $i_F$  (cf. Fig. 7.43B). Note, however, that  $i$  will be bounded by the joint velocity constraints given in (7.85).

From the reasons described above, it is possible to employ the quantity  $i_{Fy}^2$  as a performance index for the stability margin evaluation goal, instead of the rate of change of the angular momentum,  $i_{Fy}$ .

### **Optimization of the Posture and Velocity at the Impact**

A constrained optimization problem is solved to find the optimal posture and velocity of the robot at an instant when the hand hits the wooden board in the Karate chop experiments. The Sequential Quadratic Programming (SQP) method is used to solve the constrained optimization problem. This method defines the objective function and the constraints as nonlinear

functions of the design parameters. In this work, the `fmincon()` function of the numerical computing language MATLAB (MathWorks Inc.) was used to solve the SQP problem.

The objective function  $J_A$  is defined as follows:

$$J_A = w_A \left( 1 - \frac{M_{eq}^I \mathbb{B}_c^T \mathcal{V}_I^+}{(M_{eq}^I \mathbb{B}_c^T \mathcal{V}_I^+)_\text{max}} \right)^2 + (1 - w_A) \left( \frac{l_{Fy}}{l_{Fy,\text{max}}} \right)^2. \quad (7.90)$$

The first term on the r.h.s. in (7.90) is minimized when  $M_{eq}^I \mathbb{B}_c^T \mathcal{V}_I^+$  is maximized. The second term on the r.h.s., on the other hand, is minimized when  $l_{Fy}$  is minimized;  $w_A$  ( $0 \leq w_A \leq 1$ ) is a weighting factor.

The maximum values  $(M_{eq}^I \mathbb{B}_c^T \mathcal{V}_I^+)_\text{max}$  and  $l_{Fy,\text{max}}$  are estimated in advance by solving the constrained optimization problem with objective functions  $J_{A,MV} = -M_{eq}^I \mathbb{B}_c^T \mathcal{V}_I^+$  and  $J_{A,l_{Fy}} = -l_{Fy}$ , respectively. Minimizing  $-M_{eq}^I \mathbb{B}_c^T \mathcal{V}_I^+$  or  $-l_{Fy}$  yields the maximization of  $M_{eq}^I \mathbb{B}_c^T \mathcal{V}_I^+$  or  $l_{Fy}$ , respectively.

The optimization problem is to find an optimal joint angle  $\boldsymbol{\theta}$  and joint angular velocity  $\dot{\boldsymbol{\theta}}$  at the impact under the following conditions:

$$\begin{aligned} &\text{minimize} \quad J_A(\boldsymbol{\theta}, \dot{\boldsymbol{\theta}}), \\ &\text{subject to} \quad \theta_{i,\text{min}} + \theta_m \leq \theta_i(t) \leq \theta_{i,\text{max}} - \theta_m, \\ &\quad -\dot{\theta}_{i,\text{max}} \leq \dot{\theta}_i(t) \leq \dot{\theta}_{i,\text{max}}, \\ &\quad \alpha_{\text{min}} \leq \alpha(\boldsymbol{\theta}) \leq \alpha_{\text{max}}, \\ &\quad \left( \underline{r}_{pF} \right)_{x,\text{min}} \leq \left( \underline{r}_{pF}(\boldsymbol{\theta}) \right)_x \leq \left( \underline{r}_{pF} \right)_{x,\text{max}}, \end{aligned} \quad (7.91)$$

where  $\alpha$  is the angle between the wooden board and the hand (Link 6) and  $\theta_m$  is the safety margin obtained from the mechanical limits of the joint.

In this case study, the hand position was not included in the constraints in the optimization process. The hand position was calculated from the obtained joint angle  $\boldsymbol{\theta}$ . The wooden board was then placed at the calculated hand position for the experiments. It should not be too difficult, though, to employ an equality constraint for the hand position.

Furthermore, the initial posture was assigned in a heuristic way. In cases when the optimization did not converge, other initial postures were explored, heuristically. The optimization process may also get stuck into a local minimum. Therefore, several initial postures have to be explored to obtain the posture that yields the best  $J_A$  value.

### **Optimization of the Velocity Before/After the Impact**

As illustrated in Fig. 7.41, the robot motion is obtained step by step decelerating the joint velocities from the moment of the impact. Two sets of constrained optimization problems are solved to find the optimal velocities of the robot at  $t - \Delta t$  for the swing before the impact and at  $t + \Delta t$  for the swing after the impact. The optimizations are iteratively invoked to generate the whole swing motion before and after the impact.

The objective function  $J_{BC}$  is defined as follows:

$$J_{BC} = w_{BC} \hat{\boldsymbol{\theta}}^T \hat{\boldsymbol{\theta}} + (1 - w_{BC}) \left( \frac{l_{Fy}}{l_{Fy,\max}} \right)^2, \quad (7.92)$$

where  $w_{BC}$  ( $0 \leq w_{BC} \leq 1$ ) is a weighting factor. The normalized joint velocity  $\hat{\boldsymbol{\theta}}$  is defined as follows:

$$\hat{\boldsymbol{\theta}} = \begin{bmatrix} \hat{\theta}_1 & \hat{\theta}_2 & \dots & \hat{\theta}_n \end{bmatrix}^T, \quad \hat{\theta}_i = \frac{\dot{\theta}_i}{\dot{\theta}_{i,\max}}. \quad (7.93)$$

The optimization problem is to find the optimal joint velocities  $\dot{\boldsymbol{\theta}}$  at  $t - \Delta t$  and at  $t + \Delta t$  under the following conditions:

$$\begin{aligned} \text{minimize} \quad & \begin{cases} J_A(\boldsymbol{\theta}, \dot{\boldsymbol{\theta}}) & (k \leq k') \\ J_{BC}(\dot{\boldsymbol{\theta}}) & (k > k') \end{cases} \\ \text{subject to} \quad & \begin{aligned} \theta_{i,\min} \leq \theta_i(t) \leq \theta_{i,\max}, \\ -\dot{\theta}_{i,\max} \leq \dot{\theta}_i(t) \leq \dot{\theta}_{i,\max}, \\ -\ddot{\theta}_{i,\max} \leq \ddot{\theta}_i(t) \leq \ddot{\theta}_{i,\max}, \\ \dot{l}_{Fy,\min} \leq \dot{l}_{Fy} \leq \dot{l}_{Fy,\max}, \end{aligned} \end{aligned} \quad (7.94)$$

where  $k$  denotes the iteration number and  $k'$  is an arbitrary positive integer. When the humanoid robot follows exactly the generated motion, the hand will hit the wooden board exactly at the expected impact time. However, it is not realistic to expect the humanoid robot to follow the generated motion without any time delay. Therefore, the objective function  $J_A$  is invoked instead of  $J_{BC}$  during a small period around the estimated time of the impact. The period  $\pm k' \Delta t$  corresponds to the time margin for the impact. Since the same objective function  $J_A$  is used for  $k \leq k'$ , the joint velocity is not decelerated during the time interval when  $k \leq k'$ .

The boundary condition for the joint acceleration is replaced by the boundary condition for the joint velocity, as given in (7.85). Therefore, the current joint velocity will be bounded by the joint velocity from the previous step plus/minus  $\dot{\theta}_{i,\max} \Delta t$ . This boundary condition avoids the disparity of  $\dot{\theta}_i$  at the optimization points. Since the joint velocity is minimized as  $J_{BC}$  is minimized, the joint velocity tends to be near the lower bound of (7.85) when  $\dot{\theta}_i$  is positive. Consequently, the joint velocity will be gradually decelerated.

It should be noted, however, that there is no guarantee that  $\dot{\boldsymbol{\theta}}$  will always converge to zero within the joint angle limits. If  $\dot{\boldsymbol{\theta}}$  does not converge,  $\dot{\theta}_{i,\max}$  is slightly increased and the optimization process is restarted.

As a result of the optimization, the joint velocity  $\dot{\boldsymbol{\theta}}$  is obtained. Then, the current joint angle vector  $\boldsymbol{\theta}$  is calculated from  $\dot{\boldsymbol{\theta}}$  and the joint angle vector at the previous step, as given in (7.80). Note that the obtained joint trajectory after the impact (Optimization C) is just a reference trajectory, and hence, it does not guarantee stability after the impact. When the applied momentum  $M_{eq}{}^I \mathbb{B}_c^T V_I^+$  is completely transformed into the form of the applied impact, the impact will be maximized. Using the estimation of the maximum impact force, the net CoP/ZMP displacement can be estimated for the worst case, via (7.79).

**TABLE 7.9** Conditions for the motion optimization

Parameters	Values
$\Delta t$ (ms)	5
$w_A, w_{BC}$	0.03, 0.5
$\theta_m$ (rad)	0.523
$\alpha_{\min}, \alpha_{\max}$ ( $^{\circ}$ )	-5, 5
$(r_{pF})_{x,\min}, (r_{pF})_{x,\max}$ (m)	0.010, 0.030
$i_{Fy,\min}, i_{Fy,\max}$ (Nm)	-0.20, 0.20
$k'$	5

**TABLE 7.10** Success rate of the board breaking motion

Motion	Thickness (mm)	Trial	Success	Failure	Success rate (%)
Hand-made motion	3	10	10	0	100
	5	10	1	9	10
	7	5	0	5	0
Optimized motion	3	3	3	0	100
	5	10	9	1	90
	7	5	0	5	0

### 7.8.9 Experimental Verification of the Generated Impact Motion

Experiments on breaking artificial-wood boards using a hand-made motion and an optimized motion approach will be described in what follows. The parameters used to calculate the optimized motion are listed in Table 7.9. The optimized joint angles are obtained every 5 ms. Since the sampling time in the HOAP-2 humanoid robot controller is 1 ms, it is necessary to interpolate the optimized joint angles before using them as control inputs. In [78], a stabilizing control approach was proposed for the postimpact phase. This approach will not be employed in the experiments, though, since the differences between the hand-made motion and the optimized one will be better exhibited then.

Three artificial-wood boards of various thickness are used in the experiments. The success rates of breaking them are presented in Table 7.10. As apparent from the table, the success rate in the case of the hand-made motion for a board of 5 mm thickness was 10%, while the success rate for the optimized motion for the same board was 90%. Apparently, the success rate was drastically improved by using the proposed method.

The normal component of the velocity of the hand and the angular momentum in the  $y$  (pitch)-direction, calculated from the designed motion, are plotted in Fig. 7.44A and B, respectively (note that these are not experimental results). As shown in Fig. 7.44A, the hand's velocity of the optimized motion reaches a peak at the impact, while in the hand-made motion the hand's velocity reaches a peak before the impact. Furthermore, the angular momentum in the  $y$ -direction is kept at a minimum in the optimized motion. In the hand-made motion, on the other hand, vibration is observed that may cause the humanoid robot to fall.

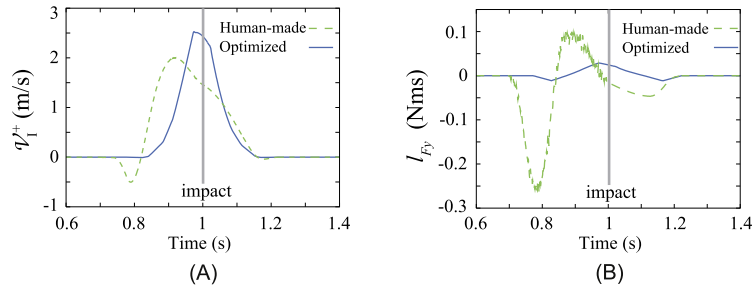


**FIGURE 7.44** Comparison between the hand-made motion and optimized motion in: (A) velocity of the hand  $V_I^+$  and (B) angular momentum  $l_{Fy}$ .

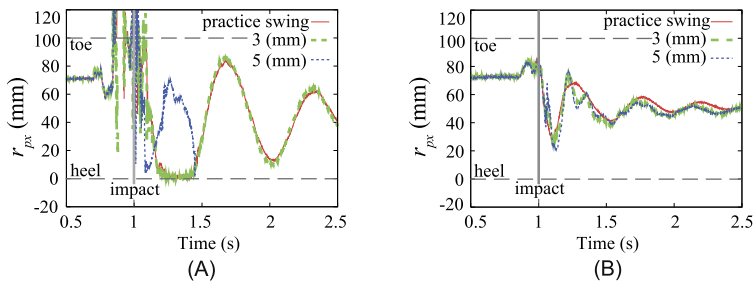


**FIGURE 7.45** CoP along the  $x$ -axis at: (A) hand-made motion and (B) optimized motion.

In the experiments, the humanoid robot HOAP-2 was placed on a force plate manufactured by KISTLER Corp. to measure the net CoP. The CoP trajectories for the hand-made and the optimized motion are plotted in Fig. 7.45A and B, respectively. Since the humanoid robot slightly jumped up during the hand-made motion, the CoP plotted in Fig. 7.45A exceeds the supporting polygon at some points. These points represent unreliable data.

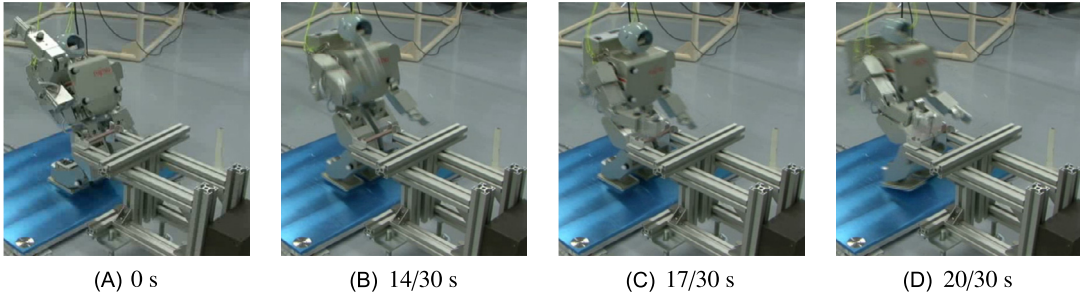
At the moment of the impact, the robot contacts the environment with its hand and feet. Therefore, at the moment of the impact, the CoP is not on the ground but on the supporting polygon formed by the hand and the feet. However, this is an instantaneous phenomenon as the board is immediately broken after the impact. Note that the CoP value plotted in Fig. 7.45A and B is measured with the force plate. Thus, strictly speaking, the CoPs in Fig. 7.45A and B at the moment of impact are incorrect.

In the hand-made motion, the CoP drastically varies after the impact, while in the optimized motion the CoP stays near the center of the support polygon. As mentioned above, the stabilizing control in [78] was not applied in these experiments. Therefore, the differences between the two generation approaches can be clearly seen. The CoP does not drastically vary in the optimized motion, even at the impact. The reason is that the board is successfully broken, and hence, the reaction force is not very large.

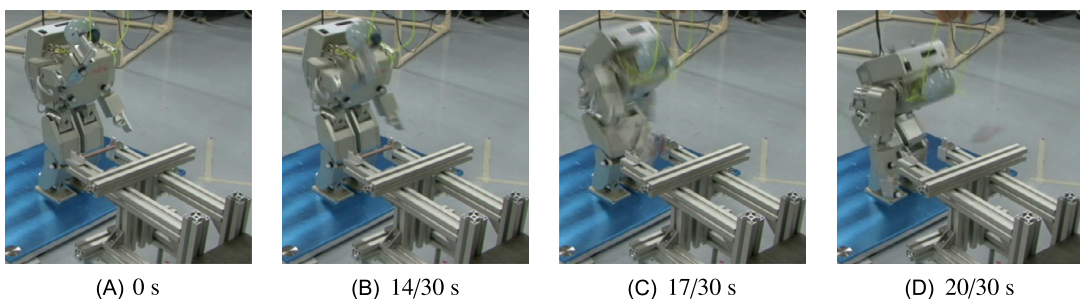
The values of  $M_{eq}^{-1} \mathbb{B}_c^T \mathcal{V}_I^+$  at the impact are presented in Table 7.11 for the cases of the hand-made and optimized motion. The snapshots of the experiments are presented in Figs. 7.46 and 7.47, Video 7.8-1 [61] was taken during the experiments.

TABLE 7.11 Estimated momentum

	$M_{eq}$ (kg)	$\mathcal{V}_L^+$ (m/s)	$M_{eq} I \mathbb{B}_c^T \mathcal{V}_L^+ (\text{Ns})$	$I_{Fy}$ (Nms)
Hand-made motion	0.097	1.46	0.141	-0.0158
Optimized motion	0.102	2.43	0.249	0.0245



**FIGURE 7.46** Snapshots of the hand-made motion. The thickness of the board was 5 mm. Snapshot (D) shows that the robot failed to break the board. The success rate was 10%.



**FIGURE 7.47** Snapshots of the optimized motion. The thickness of the board was 5 mm. Snapshot (D) shows that the robot succeeded to break the board. The success rate was 90 (%).

## References

- [1] M. Abdallah, A. Goswami, A biomechanically motivated two-phase strategy for biped upright balance control, in: IEEE Int. Conf. on Robotics and Automation, Barcelona, Spain, 2005, pp. 1996–2001.
  - [2] Z. Aftab, T. Robert, P.-B. Wieber, Predicting multiple step placements for human balance recovery tasks, Journal of Biomechanics 45 (2012) 2804–2809.
  - [3] Y. Aoustin, A. Formalskii, Upward jump of a biped, International Journal of Humanoid Robotics 10 (2013) 1350032.
  - [4] H. Arisumi, J.-R. Chardonnet, A. Kheddar, K. Yokoi, Dynamic lifting motion of humanoid robots, in: Proceedings of IEEE International Conference on Robotics and Automation, Rome, Italy, 2007, pp. 2661–2667.
  - [5] H. Asada, K. Ogawa, On the dynamic analysis of a manipulator and its end effector interacting with the environment, in: Proceedings of IEEE International Conference on Robotics and Automation, 1987, pp. 751–756.
  - [6] D. Asmar, B. Jalgha, A. Fakih, Humanoid fall avoidance using a mixture of strategies, International Journal of Humanoid Robotics 09 (2012) 1250002.
  - [7] J.E. Bobrow, B. Martin, G. Sohl, E.C. Wang, F.C. Park, J. Kim, Optimal robot motions for physical criteria, Journal of Robotic Systems 18 (2001) 785–795.

- [8] G. Borghesan, E. Aertbelien, J. De Schutter, Constraint- and synergy-based specification of manipulation tasks, in: 2014 IEEE International Conference on Robotics and Automation, ICRA, IEEE, 2014, pp. 397–402.
- [9] K. Bouyarmane, A. Escande, F. Lamiriaux, A. Kheddar, Potential field guide for humanoid multicontacts acyclic motion planning, in: IEEE International Conference on Robotics and Automation, Kobe, Japan, 2009, pp. 1165–1170.
- [10] K. Bouyarmane, A. Kheddar, Static multi-contact inverse problem for multiple humanoid robots and manipulated objects, in: IEEE-RAS International Conference on Humanoid Robots, Nashville, TN, USA, 2010, pp. 8–13.
- [11] K. Bouyarmane, A. Kheddar, Humanoid robot locomotion and manipulation step planning, *Advanced Robotics* 26 (2012) 1099–1126.
- [12] T. Bretl, Motion planning of multi-limbed robots subject to equilibrium constraints: the free-climbing robot problem, *The International Journal of Robotics Research* 25 (2006) 317–342.
- [13] T. Bretl, S. Lall, A fast and adaptive test of static equilibrium for legged robots, in: IEEE International Conference on Robotics and Automation, IEEE, 2006, pp. 1109–1116.
- [14] T. Bretl, S. Lall, Testing static equilibrium for legged robots, *IEEE Transactions on Robotics* 24 (2008) 794–807.
- [15] S. Brossette, A. Escande, G. Duchemin, B. Chrétien, A. Kheddar, Humanoid posture generation on non-Euclidean manifolds, in: IEEE-RAS International Conference on Humanoid Robots, 2015, pp. 352–358.
- [16] A. Carmona, L. Molina-Tanco, M. Azuaga, J.a. Rodriguez, F. Sandoval, Online absorption of mediolateral balance disturbances for a small humanoid robot using accelerometer and force-sensor feedback, in: 2007 IEEE/ASME International Conference on Advanced Intelligent Mechatronics, IEEE, Tenerife, Spain, 2007, pp. 1–6.
- [17] J.H. Choi, J. Grizzle, Planar bipedal robot with impulsive foot action, in: IEEE Conf. on Decision and Control, Atlantis, Paradise Island, Bahamas, 2004, pp. 296–302.
- [18] R. Cisneros, K. Yokoi, E. Yoshida, Impulsive pedipulation of a spherical object for reaching a 3D goal position, in: IEEE-RAS International Conference on Humanoid Robots, Atlanta, GA, USA, 2013, pp. 154–160.
- [19] A. D'Avella, E. Bizzi, Shared and specific muscle synergies in natural motor behaviors, *Proceedings of the National Academy of Sciences* 102 (2005) 3076–3081.
- [20] J. Englsberger, T. Koolen, S. Bertrand, J. Pratt, C. Ott, A. Albu-Schaffer, Trajectory generation for continuous leg forces during double support and heel-to-toe shift based on divergent component of motion, in: IEEE/RSJ International Conference on Intelligent Robots and Systems, 2014, pp. 4022–4029.
- [21] J. Englsberger, C. Ott, A. Albu-Schaffer, Three-dimensional bipedal walking control based on divergent component of motion, *IEEE Transactions on Robotics* 31 (2015) 355–368.
- [22] J. Englsberger, C. Ott, M.A. Roa, A. Albu-Schaffer, G. Hirzinger, Bipedal walking control based on capture point dynamics, in: IEEE International Conference on Intelligent Robots and Systems, IEEE, 2011, pp. 4420–4427.
- [23] A. Escande, A. Kheddar, S. Miossec, Planning support contact-points for humanoid robots and experiments on HRP-2, in: IEEE International Conference on Intelligent Robots and Systems, 2006, pp. 2974–2979.
- [24] A. Escande, A. Kheddar, S. Miossec, Planning contact points for humanoid robots, *Robotics and Autonomous Systems* 61 (2013) 428–442.
- [25] Fujitsu, Miniature Humanoid Robot HOAP-2 Manual, 1st edition, Fujitsu Automation Co., Ltd, 2004 (in Japanese).
- [26] A. Goswami, Postural stability of biped robots and the foot-rotation indicator (fri) point, *The International Journal of Robotics Research* 18 (1999) 523–533.
- [27] R.J. Griffin, A. Leonessa, A. Asbeck, Disturbance compensation and step optimization for push recovery, in: IEEE/RSJ International Conference on Intelligent Robots and Systems, IROS, IEEE, 2016, pp. 5385–5390.
- [28] J. Grizzle, G. Abba, F. Plestan, Asymptotically stable walking for biped robots: analysis via systems with impulse effects, *IEEE Transactions on Automatic Control* 46 (2001) 51–64.
- [29] M. Guihard, P. Gorce, Dynamic control of bipeds using ankle and hip strategies, in: IEEE/RSJ Int. Conf. on Intelligent Robots and Systems, Lausanne, Switzerland, 2002, pp. 2587–2592.
- [30] K. Harada, K. Hauser, T. Bretl, J.-C. Latombe, Natural motion generation for humanoid robots, in: IEEE/RSJ International Conference on Intelligent Robots and Systems, 2006, pp. 833–839.
- [31] H. Hauser, G. Neumann, A.J. Ijspeert, W. Maass, Biologically inspired kinematic synergies provide a new paradigm for balance control of humanoid robots, in: IEEE-RAS International Conference on Humanoid Robots, Pittsburgh, PA, 2007, pp. 73–80.
- [32] H. Hauser, G. Neumann, A.J. Ijspeert, W. Maass, Biologically inspired kinematic synergies enable linear balance control of a humanoid robot, *Biological Cybernetics* 104 (2011) 235–249.

- [33] K. Hauser, Fast interpolation and time-optimization with contact, *The International Journal of Robotics Research* 33 (2014) 1231–1250.
- [34] K. Hauser, T. Bretl, K. Harada, J.-C. Latombe, Using motion primitives in probabilistic sample-based planning for humanoid robots, in: S. Akella, N.M. Amato, W.H. Huan, B. Mishra (Eds.), *Algorithmic Foundation of Robotics VII*, in: Springer Tracts in Advanced Robotics, vol. 47, Springer Berlin Heidelberg, Berlin, Heidelberg, 2008, pp. 507–522.
- [35] K. Hauser, T. Bretl, J.C. Latombe, Non-gaited humanoid locomotion planning, in: IEEE-RAS International Conference on Humanoid Robots, 2005, pp. 7–12.
- [36] R. Hinata, D. Nenchev, Anticipatory reflexive behavior in response to an impulsive force applied while leaning forward, Robotic Life Support Laboratory, Tokyo City University, 2018 (Video clip), <https://doi.org/10.1016/B978-0-12-804560-2.00014-6>.
- [37] R. Hinata, D. Nenchev, Nonanticipatory reflexive behavior in response to an impulsive force applied while leaning forward, Robotic Life Support Laboratory, Tokyo City University, 2018 (Video clip), <https://doi.org/10.1016/B978-0-12-804560-2.00014-6>.
- [38] R. Hinata, D.N. Nenchev, Accommodating a large impulsive force without stepping, Robotic Life Support Laboratory, Tokyo City University, 2018 (Video clip), <https://doi.org/10.1016/B978-0-12-804560-2.00014-6>.
- [39] K. Hirai, M. Hirose, Y. Haikawa, T. Takenaka, The development of Honda humanoid robot, in: IEEE Int. Conf. on Robotics and Automation, Leuven, Belgium, 1998, pp. 1321–1326.
- [40] H. Hirukawa, S. Hattori, K. Harada, S. Kajita, K. Kaneko, F. Kanehiro, K. Fujiwara, M. Morisawa, A universal stability criterion of the foot contact of legged robots – adios ZMP, in: IEEE International Conference on Robotics and Automation, 2006, pp. 1976–1983.
- [41] A. Hofmann, M. Popovic, H. Herr, Exploiting angular momentum to enhance bipedal center-of-mass control, in: IEEE Int. Conf. on Robotics and Automation, Kobe, Japan, 2009, pp. 4423–4429.
- [42] F.B. Horak, S.M. Henry, A. Shumway-Cook, Postural perturbations: new insights for treatment of balance disorders, *Physical Therapy* 77 (1997) 517–533.
- [43] M. Hosokawa, T. Hamano, D. Nenchev, Lift-leg reactive synergy with DCM-GI based control, Robotic Life Support Laboratory, Tokyo City University, 2018 (Video clip), <https://doi.org/10.1016/B978-0-12-804560-2.00014-6>.
- [44] M. Hosokawa, D.N. Nenchev, T. Hamano, The DCM generalized inverse: efficient body-wrench distribution in multi-contact balance control, *Advanced Robotics* 32 (2018) 778–792.
- [45] Y. Hürmüzlü, G.D. Moskowitz, Bipedal locomotion stabilized by impact and switching: I. Two- and three-dimensional, three-element models, *Dynamics and Stability of Systems* 2 (1987) 73–96.
- [46] Y. Hürmüzlü, G.D. Moskowitz, Bipedal locomotion stabilized by impact and switching: II. Structural stability analysis of a four-element bipedal locomotion model, *Dynamics and Stability of Systems* 2 (1987) 97–112.
- [47] Y. Hwang, A. Konno, M. Uchiyama, Whole body cooperative tasks and static stability evaluations for a humanoid robot, in: Proceedings of IEEE/RSJ International Conference on Intelligent Robots and Systems, 2003, pp. 1901–1906.
- [48] S.-H. Hyon, R. Osu, Y. Otaka, Integration of multi-level postural balancing on humanoid robots, in: IEEE International Conference on Robotics and Automation, Kobe, Japan, 2009, pp. 1549–1556.
- [49] R. Iizuka, D.N. Nenchev, Reflex/recovery motion with ankle/hip/twist synergies, Robotic Life Support Laboratory, Tokyo City University, 2018 (Video clip), <https://doi.org/10.1016/B978-0-12-804560-2.00014-6>.
- [50] R. Iizuka, D.N. Nenchev, Reflex/recovery motion with hip/twist synergies, Robotic Life Support Laboratory, Tokyo City University, 2018 (Video clip), <https://doi.org/10.1016/B978-0-12-804560-2.00014-6>.
- [51] C. Inamura, T. Nakamura, D.N. Nenchev, Compliant whole-body balance control, Robotic Life Support Laboratory, Tokyo City University, 2018 (Video clip), <https://doi.org/10.1016/B978-0-12-804560-2.00014-6>
- [52] R. Iizuka, D.N. Nenchev, Reactive stepping, Robotic Life Support Laboratory, Tokyo City University, 2018 (Video clip), <https://doi.org/10.1016/B978-0-12-804560-2.00014-6>.
- [53] K. Iqbal, H. Hemami, S. Simon, Stability and control of a frontal four-link biped system, *IEEE Transactions on Biomedical Engineering* 40 (1993) 1007–1018.
- [54] T. Izumi, Y. Kitaka, Control of a hitting velocity and direction for a hammering robot using a flexible link, *Journal of the Robotics Society of Japan* 11 (1993) 436–443 (in Japanese).
- [55] S. Kagami, F. Kanehiro, Y. Tamiya, M. Inaba, H. Inoue, AutoBalancer: an online dynamic balance compensation scheme for humanoid robots, in: Int. Workshop Alg. Found. Robot, WAFR, 2000, pp. 329–339.

- [56] S. Kajita, F. Kanehiro, K. Kaneko, K. Fujiwara, K. Harada, K. Yokoi, H. Hirukawa, Biped walking pattern generation by using preview control of zero-moment point, in: IEEE International Conference on Robotics and Automation, 2003, pp. 1620–1626.
- [57] Y. Kanamiya, S. Ota, D. Sato, Ankle and hip balance control strategies with transitions, in: IEEE International Conference on Robotics and Automation, Anchorage, AK, USA, 2010, pp. 3446–3451.
- [58] H. Khalil, Nonlinear Systems, 3rd edition, Prentice Hall, Upper Saddle River, New Jersey, USA, 2002.
- [59] K. Kitagaki, M. Uchiyama, Optimal approach velocity of end-effector to the environment, in: Proceedings of IEEE International Conference on Robotics and Automation, 1992, pp. 1928–1934.
- [60] S. Komizunai, Y. Onuki, M.H. Wu, T. Tsujita, A. Konno, A walking stabilization control for biped robots on loose soil, Journal of the Robotics Society of Japan 35 (2017) 548–556.
- [61] A. Konno, Karate chop experiments with the HOAP-2 robot, 2015 (Video clip), <https://doi.org/10.1016/B978-0-12-804560-2.00014-6>.
- [62] A. Konno, HOAP-2 walking on sand, 2016 (Video clip), <https://doi.org/10.1016/B978-0-12-804560-2.00014-6>.
- [63] A. Konno, T. Matsumoto, Y. Ishida, D. Sato, M. Uchiyama, Drum beating a martial art Bojutsu performed by a humanoid robot, in: A.C. de Pina Filho (Ed.), Humanoid Robots: New Developments, Advanced Robotic Systems International and I-Tech Education and Publishing, ISBN 978-3-902613-00-4, 2007, pp. 521–530, Chapter 29.
- [64] A. Konno, T. Myojin, T. Matsumoto, T. Tsujita, M. Uchiyama, An impact dynamics model and sequential optimization to generate impact motions for a humanoid robot, The International Journal of Robotics Research 30 (2011) 1596–1608.
- [65] A. Konno, Y. Tanida, K. Abe, M. Uchiyama, A plantar h-slit force sensor for humanoid robots to detect the reaction forces, in: Proceedings of IEEE/RSJ International Conference on Intelligent Robots and Systems, 2005, pp. 1470–1475.
- [66] T. Koolen, S. Bertrand, G. Thomas, T. de Boer, T. Wu, J. Smith, J. Englsberger, J. Pratt, Design of a momentum-based control framework and application to the humanoid robot Atlas, International Journal of Humanoid Robotics 13 (2016) 1650007.
- [67] T. Koolen, T. de Boer, J. Rebula, A. Goswami, J. Pratt, Capturability-based analysis and control of legged locomotion, Part 1: theory and application to three simple gait models, The International Journal of Robotics Research 31 (2012) 1094–1113.
- [68] S. Kudoh, T. Komura, K. Ikeuchi, The dynamic postural adjustment with the quadratic programming method, in: IEEE/RSJ International Conference on Intelligent Robots and System, 2002, pp. 2563–2568.
- [69] M. Kudruss, M. Naveau, O. Stasse, N. Mansard, C. Kirches, P. Soueres, K. Mombaur, Optimal control for whole-body motion generation using center-of-mass dynamics for predefined multi-contact configurations, in: IEEE-RAS 15th International Conference on Humanoid Robots (Humanoids), 2015, pp. 684–689.
- [70] J.J. Kuffner, S. Kagami, K. Nishiwaki, M. Inaba, H. Inoue, Dynamically-stable motion planning for humanoid robots, Autonomous Robots 12 (2002) 105–118.
- [71] M.L. Latash, Synergy, Oxford University Press, 2008.
- [72] S.M. LaValle, J.J. Kuffner Jr., Rapidly-exploring random trees: progress and prospects, in: Workshop on the Algorithmic Foundations of Robotics, Hanover, New Hampshire, 2000, pp. 293–308.
- [73] D.J. Leith, W.E. Leithead, Survey of gain-scheduling analysis and design, International Journal of Control 73 (2000) 1001–1025.
- [74] A. Liegeois, Automatic supervisory control of the configuration and behavior of multibody mechanisms, IEEE Transactions on Systems, Man and Cybernetics 7 (1977) 868–871.
- [75] C.W. Luchies, N.B. Alexander, A.B. Schultz, J. Ashton-Miller, Stepping responses of young and old adults to postural disturbances: kinematics, Journal of the American Geriatrics Society 42 (1994) 506–512.
- [76] B. Maki, W. McIlroy, G. Fernie, Change-in-support reactions for balance recovery, IEEE Engineering in Medicine and Biology Magazine 22 (2003) 20–26.
- [77] N. Mandal, S. Payandeh, Control strategies for robotic contact tasks: an experimental study, The International Journal of Robotics Research 12 (1995) 67–92.
- [78] T. Matsumoto, A. Konno, L. Gou, M. Uchiyama, A humanoid robot that breaks wooden boards applying impulsive force, in: Proceedings of IEEE/RSJ International Conference on Intelligent Robots and Systems, 2006, pp. 5919–5924.
- [79] M.-L. Mille, M.E. Johnson, K.M. Martinez, M.W. Rogers, Age dependent differences in lateral balance recovery through protective stepping, Clinical Biomechanics 20 (2005) 607–616.

- [80] J.K. Mills, D.M. Lokhorst, Control of robotic manipulators during general task execution: a discontinuous control approach, *The International Journal of Robotics Research* 12 (1993) 146–163.
- [81] S. Miyahara, D.N. Nenchev, VRP-GI based dynamic walk on a flat ground, Robotic Life Support Laboratory, Tokyo City University, 2018 (Video clip), <https://doi.org/10.1016/B978-0-12-804560-2.00014-6>.
- [82] S. Miyahara, D.N. Nenchev, VRP-GI based dynamic walk on a staircase, Robotic Life Support Laboratory, Tokyo City University, 2018 (Video clip), <https://doi.org/10.1016/B978-0-12-804560-2.00014-6>.
- [83] S. Miyahara, D.N. Nenchev, VRP-GI based dynamic walk with toe-off, Robotic Life Support Laboratory, Tokyo City University, 2018 (Video clip), <https://doi.org/10.1016/B978-0-12-804560-2.00014-6>.
- [84] X. Mu, Q. Wu, On impact dynamics and contact events for biped robots via impact effects, *IEEE Transactions on Systems, Man and Cybernetics. Part B. Cybernetics* 36 (2006) 1364–1372.
- [85] K. Nagasaka, M. Inaba, H. Inoue, Stabilization of dynamic walk on a humanoid using torso position compliance control, in: Proceedings of Annual Conference of Robotics Society of Japan, 1999, pp. 1193–1194 (in Japanese).
- [86] K. Nagata, T. Ogasawara, T. Omata, Optimum velocity vector of articulated robot for soft bumping, *Journal of the SICE* 26 (1990) 435–442 (in Japanese).
- [87] S. Nakaoka, Chorenoid: extensible virtual robot environment built on an integrated GUI framework, in: IEEE/SICE International Symposium on System Integration, SII, 2012, pp. 79–85.
- [88] T. Narukawa, M. Takahashi, K. Yoshida, Stability analysis of a simple active biped robot with a torso on level ground based on passive walking mechanisms, in: M. Hackel (Ed.), *Humanoid Robots, Human-Like Machines*, I-Tech Education and Publishing, 2007, pp. 163–174.
- [89] D. Nenchev, Y. Tsumaki, M. Uchiyama, Singularity-consistent parameterization of robot motion and control, *The International Journal of Robotics Research* 19 (2000) 159–182.
- [90] D. Nenchev, K. Yoshida, Impact analysis and post-impact motion control issues of a free-floating space robot subject to a force impulse, *IEEE Transactions on Robotics and Automation* 15 (1999) 548–557.
- [91] D.N. Nenchev, A. Nishio, Ankle and hip strategies for balance recovery of a biped subjected to an impact, *Robotica* 26 (2008) 643–653.
- [92] A. Nishio, K. Takahashi, D. Nenchev, Balance control of a humanoid robot based on the reaction null-space method, in: IEEE/RSJ Int. Conf. on Intelligent Robots and Systems, Beijing, China, 2006, pp. 1996–2001.
- [93] S. Onuma, D. Nenchev, Reactive motion in 3D obtained by super-positioning of simple synergies, Robotic Life Support Laboratory, Tokyo City University, 2015 (Video clip), <https://doi.org/10.1016/B978-0-12-804560-2.00014-6>.
- [94] S. Ota, S. Onuma, D. Nenchev, Ankle-hip reactive synergies with transitions, Robotic Life Support Laboratory, Tokyo City University, 2011 (Video clip), <https://doi.org/10.1016/B978-0-12-804560-2.00014-6>.
- [95] H.W. Park, A. Ramezani, J.W. Grizzle, A finite-state machine for accommodating unexpected large ground-height variations in bipedal robot walking, *IEEE Transactions on Robotics* 29 (2013) 331–345.
- [96] J.L. Patton, M.J. Hilliard, K. Martinez, M.-L. Mille, M.W. Rogers, A simple model of stability limits applied to sidestepping in young, elderly and elderly fallers, in: IEEE EMBS Annual International Conference, New York City, NY, 2006, pp. 3305–3308.
- [97] Q.-C. Pham, Y. Nakamura, Time-optimal path parameterization for critically dynamic motions of humanoid robots, in: 2012 12th IEEE-RAS International Conference on Humanoid Robots, IEEE, Osaka, Japan, 2012, pp. 165–170.
- [98] Q.-C. Pham, O. Stasse, Time-optimal path parameterization for redundantly actuated robots: a numerical integration approach, *IEEE/ASME Transactions on Mechatronics* 20 (2015) 3257–3263.
- [99] J. Pratt, T. Koolen, T. de Boer, J. Rebula, S. Cotton, J. Carff, M. Johnson, P. Neuhaus, Capturability-based analysis and control of legged locomotion, Part 2: application to M2V2, a lower-body humanoid, *The International Journal of Robotics Research* 31 (2012) 1117–1133.
- [100] S. Rietdyk, A. Patla, D. Winter, M. Ishac, C. Little, Balance recovery from medio-lateral perturbations of the upper body during standing, *Journal of Biomechanics* 32 (1999) 1149–1158.
- [101] M. Rijnen, E. de Mooij, S. Traversaro, F. Nori, N. van de Wouw, A. Saccon, H. Nijmeijer, Control of humanoid robot motions with impacts: numerical experiments with reference spreading control, in: IEEE International Conference on Robotics and Automation, ICRA, 2017, pp. 4102–4107.
- [102] A. Shumway-Cook, F.B. Horak, Vestibular rehabilitation: an exercise approach to managing symptoms of vestibular dysfunction, *Seminars in Hearing* 10 (1989) 196–209.

- [103] B.J. Stephens, Integral control of humanoid balance, in: IEEE/RSJ International Conference on Intelligent Robots and Systems, San Diego, CA, USA, 2007, pp. 4020–4027.
- [104] K. Takase, Task execution by robot hand, *Journal of the SICE* 29 (1990) 213–219 (in Japanese).
- [105] T. Takenaka, T. Matsumoto, T. Yoshiike, Real time motion generation and control for biped robot – 1st report: walking gait pattern generation, in: IEEE/RSJ International Conference on Intelligent Robots and Systems, 2009, pp. 1084–1091.
- [106] K. Tamoto, R. Yui, R. Hinata, D.N. Nenchev, Motion synergy generation with multiple commands, Robotic Life Support Laboratory, Tokyo City University, 2017 (Video clip), <https://doi.org/10.1016/B978-0-12-804560-2.00014-6>.
- [107] T.-J. Tarn, Y. Wu, N. Xi, A. Isidori, Force regulation and contact transition control, *IEEE Control Systems* 16 (1996) 32–40.
- [108] M. Uchiyama, *A Control Algorithm Constitution Method for Artificial Arm and Dynamic Control Modes*, University of Tokyo Press, 1975 (in Japanese).
- [109] J. Vaillant, A. Kheddar, H. Audren, F. Keith, S. Brossette, A. Escande, K. Bouyarmane, K. Kaneko, M. Morisawa, P. Gergondet, E. Yoshida, S. Kajita, F. Kanehiro, Multi-contact vertical ladder climbing with an HRP-2 humanoid, *Autonomous Robots* 40 (2016) 561–580.
- [110] R. Volpe, P. Khosla, A theoretical and experimental investigation of impact control for manipulators, *The International Journal of Robotics Research* 12 (1993) 351–365.
- [111] M. Vukobratović, Contribution to the study of anthropomorphic systems, *Kybernetika* 8 (1972) 404–418.
- [112] M. Vukobratović, *Legged Locomotion Robots and Anthropomorphic Mechanisms*, Mihailo Pupin Institute, Belgrade, 1975.
- [113] M. Vukobratović, B. Borovac, D. Šurdilović, Zero-moment point – proper interpretation and new applications, in: Proceedings of the IEEE/RAS International Conference on Humanoid Robots, 2001, pp. 237–244.
- [114] M. Vukobratovic, D. Juricic, Contribution to the synthesis of biped gait, *IEEE Transactions on Biomedical Engineering* BME-16 (1969) 1–6.
- [115] I.D. Walker, Impact configurations and measures for kinematically redundant and multiple armed robot system, *IEEE Transactions on Robotics and Automation* 10 (1994) 670–683.
- [116] G. Wiedebach, S. Bertrand, T. Wu, L. Fiorio, S. McCrary, R. Griffin, F. Nori, J. Pratt, Walking on partial footholds including line contacts with the humanoid robot Atlas, in: IEEE-RAS International Conference on Humanoid Robots, 2016, pp. 1312–1319.
- [117] D. Winter, Human balance and posture control during standing and walking, *Gait & Posture* 3 (1995) 193–214.
- [118] D. Winter, A.E. Patla, J.S. Frank, Assessment of balance control in humans, *Medical Progress Through Technology* 16 (1990) 31–51.
- [119] A. Witkin, M. Kass, Spacetime constraints, *ACM SIGGRAPH Computer Graphics* 22 (1988) 159–168.
- [120] K. Yamane, Y. Nakamura, Synergetic CG choreography through constraining and deconstraining at will, in: IEEE International Conference on Robotics and Automation, Washington, DC, 2002, pp. 855–862.
- [121] S.-J. Yi, B.-t. Zhang, D. Hong, D.D. Lee, Active stabilization of a humanoid robot for impact motions with unknown reaction forces, in: IEEE/RSJ International Conference on Intelligent Robots and Systems, IEEE, Vilamoura, Algarve, Portugal, 2012, pp. 4034–4039.
- [122] S.-J. Yi, B.-T. Zhang, D. Hong, D.D. Lee, Whole-body balancing walk controller for position controlled humanoid robots, *International Journal of Humanoid Robotics* 13 (2016) 1650011.
- [123] K. Yoshida, R. Kurazume, N. Sashida, Y. Umetani, Modeling of collision dynamics for space free-floating links with extended generalized inertia tensor, in: Proceedings of IEEE International Conference on Robotics and Automation, 1992, pp. 899–904.
- [124] K. Yoshida, D.N. Nenchev, Space robot impact analysis and satellite-base impulse minimization using reaction null-space, in: Proceedings of IEEE International Conference on Robotics and Automation, 1995, pp. 1271–1277.
- [125] Y. Yoshida, D.N. Nenchev, Ankle/Lift-leg lateral-plane reactive synergy from simple model, Robotic Life Support Laboratory, Tokyo City University, 2014 (Video clip), <https://doi.org/10.1016/B978-0-12-804560-2.00014-6>.
- [126] Y. Yoshida, K. Takeuchi, Y. Miyamoto, D. Sato, D.N. Nenchev, Postural balance strategies in response to disturbances in the frontal plane and their implementation with a humanoid robot, *IEEE Transactions on Systems, Man, and Cybernetics: Systems* 44 (2014) 692–704.
- [127] R. Yui, R. Hinata, D.N. Nenchev, Motion synergy generation with single command, Robotic Life Support Laboratory, Tokyo City University, 2018 (Video clip), <https://doi.org/10.1016/B978-0-12-804560-2.00014-6>.
- [128] Y.-F. Zheng, H. Hemami, Mathematical modeling of a robot collision with its environment, *Journal of Robotic Systems* 2 (1985) 289–307.